國 立 交 通 大 學

機械工程學系

碩士論文

# 並聯矩陣沙伯紐式風車效率改善數值研究

# CFD Analysis for the Improvement on Power Efficiency of Savonius Wind Rotors in Parallel Matrix System

研究生： 蘇子博

指導教授： 陳俊勳 教授

中 華 民 國 一 〇 二 年 十 月

# 並聯矩陣沙伯紐式風車效率改善數值研究

CFD Analysis for the Improvement on Power Efficiency of Savonius Wind Rotors in Parallel Matrix System

研究生：蘇子博　　Student：Tzu-Po Su

指導教授：陳俊勳　　Advisor：Chiun-Hsun Chen

國立交通大學

機械工程學系

碩士論文

A Thesis

Submitted to Department of Mechanical Engineering

College of Engineering

National Chiao Tung University

In Partial Fulfillment of the Requirements

For the Degree of

Master of Science

In Mechanical Engineering

October 2013

Hsinchu, Taiwan, Republic of China

中華民國一〇二年十月

CFD Analysis for the Improvement on Power Efficiency of Savonius Wind Rotors in Parallel Matrix System

並聯矩陣沙伯紐式風車效率改善數值研究

學 生：蘇 子 博　　指 導 教 授:陳 俊 勳

國立交通大學機械工程學系

# 摘要

本研究使用流體力學套裝軟體 Fluent 分析二葉式沙伯紐式風車周圍的流場與其對應的效能。效能的衡量標準為功率係數 $C_p$(power coefficient)。本研究內容可分為三部分：其一為對單一風車的研究，其二為四風車並聯矩陣系統的研究，其三為十風車並聯矩陣系統的研究。三個系統將會與其分別對應的參數進行研究。在參數分析中，改變參數為風速與周速比，在此之後會探討風向對並聯矩陣系統的影響。最後，本研究將討論三種系統的差異比較。

由數值模擬結果顯示，單一風車之最大 $C_p$ 值為 0.191，發生在周速比 0.8 的情況下；四風車並聯矩陣系統之最大 $C_p$ 值為 0.402，發生在周速比 0.9 的情況下;而十風車並聯矩陣系統之最大 $C_p$ 值為 0.438，發生在周速比 0.7 的情況下。十風車並聯矩陣系統的平均 $C_p$ 值是單一風車的 2.25 倍，四風車並聯矩陣系統的平均 $C_p$ 值是單一風車的 2.07 倍,而十風車並聯矩陣系統的平均 $C_p$ 值是四風車並聯矩陣系統的 1.08 倍。

三個系統的功率係數（$C_p$）分別在同一周速比的情況下，會隨風速提升而略微提高。並聯矩陣系統的效能提升主要歸因於風車間的正向干擾情形，而流場的波動現象在此效應中扮演主要角色，但此種正

向干擾效應受風向改變的影響極大。當風向改變為 0°時，其效能幾乎不會改變，甚至低於單一風車情況下的效能。

關鍵字：沙伯紐式風車、並聯矩陣系統、功率係數

CFD Analysis for the Improvement on Power Efficiency of Savonius Wind Rotors in Parallel Matrix System

Student: Tzu-Po Su Advisor: Prof. Chiun-Hsun Chen

Department of Mechanical Engineering

National Chiao Tung University

# ABSTRACT

This study employs a computational fluid dynamics (CFD) software, Fluent, to analyze the flow fields around two-bladed Savonius wind rotors and their corresponding performances. This research includes three cases: the first one is a study of a single Savonius wind rotor, the second is the parallel matrix system, consisting of four two-bladed Savonius wind rotors, and the last one is the parallel matrix system of ten two-bladed Savonius wind rotors. All of the cases are carried out by the corresponding parametric studies, whose parameters include the wind velocity and tip speed ratio. After that, the influence of wind direction change on the parallel system is also studied. Then, comparisons between the systems mentioned above are discussed.

The simulation results show that the maximum $C_p$ value of one single Savonius wind rotor is 0.191 at tip-speed ratio 0.8; the parallel matrix system with four Savonius wind rotors is 0.402 at tip-speed ratio 0.9; the parallel matrix system with ten Savonius wind rotors is 0.438 at tip-speed ratio 0.7. The average $C_p$ of the parallel matrix system with ten Savonius wind rotors is 2.25 times higher than that in one single Savonius wind rotor and the average $C_p$ of the parallel matrix system with four

Savonius wind rotors is 2.07 times higher than that in one single Savonius wind rotor. However, the average $C_p$ of the parallel matrix system with ten Savonius wind rotors is 1.08 times higher than that in the parallel matrix system with four Savonius wind rotors.

The $C_p$ of these three cases slightly increase with wind speeds at the same tip speed ratio. The higher performance of parallel matrix system is resulted from the positive interaction between these Savonius wind rotors, and the flow fluctuation plays the major role in contributing to this effect, but this effect is strongly influenced by the change of wind direction. When wind direction is 0°, the $C_p$ of the parallel matrix system becomes almost the same or even lower than that of a single one.

Keywords: Savonius wind rotor; parallel matrix system; $C_p$ (power coefficient)

# ACKNOWLEDGEMENTS

首先必須感謝我的指導教授　陳俊勳教授，總是耐心地糾正我的錯誤並給予指導，在老師用心的教誨下，使我在這兩年內學習到許多處理事情與解決問題的能力。感謝曾錦鍊學長給了我這個題目並也給予許多指導。

再來是感謝這兩年陪我一起度過的諸位同學們，不論是一同修課或是一同吃飯，不管在瑣事還是正事上都給我許多幫助。這兩年我們一同走過的經歷，這些都歷歷在目。還有實驗室的諸位學長們，在研究中所遇到的問題你們總是不吝指教，也不會在我們面前擺出學長的架子，讓人覺得十分親近。另外也感謝學長馮嘉軒、黃天洋教導我許多風車模擬以及論文寫作的技巧。

感謝所有曾經給過我鼓勵的朋友們，雖然可能一時無法把名字都一一點出來，但你們曾經給予過我的，我都不會忘記。最後，鄭重地感謝我的家人，雖然不常在家，但你們總是最默默支持我的一群，這才是我在遇到挫折時還能繼續前進的最大動力。未來還有許多的路要走，大學一路上來，並在研究所這兩年的經歷與學習，實在立定了我人生未來道路的基礎。

# CONTENTS

# LIST OF TABLE

# LIST OF FIGURES

# CHAPTER 1

# INTRODUCTION

## 1.1 Motivation

The fossil fuel resources on earth are limited, and the global demands for gas, oil and coal exceed the supplies. As a consequence, they are more and more expensive. Therefore, the heavily dependence on fossil fuels could cause serious problems, including energy shortage and carbon dioxide emissions due to burning of fossil fuels.

As shown in **Fig. 1.1**, Carbon dioxide emissions are increasing year by year that cause global warming. Hence, researches of renewable energy are extremely important. Many countries are committed to develop the renewable energies, such as wind energy, solar energy, geothermal energy, ocean energy, hydropower and bioenergy. The carbon dioxide emissions are very low during the production processes of these renewable energy sources, as illustrated in **Fig. 1.2**. Although nuclear power does not emit any carbon dioxide during power generation, but there are strong oppositions against strengthening nuclear power in many countries of the world due to its safety and waste-handling problems. As mentioned previously, wind energy is one of the important renewable energies, which has a much lower carbon dioxide emission compared with the fossil fuel resources. In other words, its pollution to the environment is very low.

Wind power is the conversion of the wind momentum energy into a useful form of energy. There are two kinds of principal wind turbine designs. They are horizontal-axis wind turbines (HAWTs), whose rotation axis is parallel to the

horizon, and vertical-axis wind turbines (VATWs), whose axis is perpendicular to the horizon. Their structures are demonstrated in **Fig. 1.3**. It is commonly known that the power coefficient ($C_p$) of HAWTs, ranged from about 0.30 to 0.45, is higher than that of VAWTs, whose range is from 0.15 to 0.30. However, there are a few problems in HAWTs. First, HAWTs spinning with high tip speed ratio always cause the low-frequency sound to make noise pollution. Second, it is necessary to need a sufficient distance between the wind rotors in order to avoid wake effect (see **Fig. 1.4**), resulting in a lower energy conversion. Third, the fan should be aligned with the wind direction in order to obtain a better efficiency, but it always takes a long time to adjust. Last but not the least, the costs of land preparations, installation, maintenance and repair of HAWTs are considerable. On the other hand, VAWTs, with the low-cost capital and simple structure, can be more efficiently installed in the low wind area. It can be divided into two categories based on their blade designs: Darrieus wind turbine is lift-type, whereas Savonius wind turbine is drag-type. Relative to the drag-type wind turbines, the lift-type wind turbine has a better value of $C_p$, but the starting torque is low. Besides, Savonius wind turbine is noiseless and it is able to bear the wind with fluctuation. However, the power efficiency needs to be improved.

Even though the $C_p$ of HAWTs is higher than the one of VAWTs, there are a lot of methods to improve the latter one's performance. In order to achieve this purpose, for instance, it can put a series of VAWTs connecting in parallel with a fixed distance between them, and they rotate with a specific phase angle difference. In Feng's preliminary study [1], the simulation of parallel matrix system consisted of three two-bladed Savonius wind rotors, as shown in **Fig. 1.5**, to rotate with 90 degree phase angle deference. Its $C_p$ is about 1.45 times that of

one single Savonius wind rotor in 3-D simulation. Following by Huang's study [2], the simulation of parallel matrix system adopted four two-bladed Savonius wind rotors to rotate with 90 degree phase angle deference (see **Fig. 1.6**). Its average $C_p$ is about 1.46. To further enhance the efficiency of two-bladed Savonius wind rotor parallel matrix system, the present work intends to establish three groups of four two-bladed Savonius wind rotors parallel matrix systems and investigating their respective performance by using computational fluid dynamics (CFD) technique. And then find the optimum $C_p$ value. In this way, the best performance can be expected to find by fully utilizing wind fields in effect.

## 1.2 Literature Review

The Savonius wind rotor is a drag-typed vertical-axis wind rotor, developed by S. J. Savonius [3]. Its shape is similar to the character "S", therefore, it is also called S-rotor. This kind of rotor is spinned by drag force. The drag force difference between concave and convex surfaces drives the rotor, leading to a large starting torque with a relatively low rotational speed. Many improving researches are bringing up after the Savonius' development.

Blackwell et al. [4] investigated the performances of fifteen configurations of Savonius wind rotors by testing in a low speed wind tunnel. What they investigated included parameters, such as number of blades, wind velocity, wind rotor height, and blade overlap ratio. The results showed that the two-bladed configurations have better performance than the three-bladed ones, except the starting torque. Besides, the performance increases with aspect ratio slightly, and the optimum overlap ratio is between 0.1 and 0.15.

Fujisawa [5] studied the performances of two-bladed Savonius wind rotors with different overlap ratios ranged from 0 to 0.5 by experimental investigations. The results reveal that the performance of Savonius wind rotor reaches a maximum value at an overlap ratio of 0.15. It is due to the fact that the flow through the overlap strengthens the forward movement. However, when the overlap ratio becomes larger, the recirculation zone grows accordingly, causing the performance deterioration.

Gupta et al. [6] studied the performances of a Savonius wind rotor and a Savonius-Darrieus machine with overlap variation by experimental investigations. For the Savonius-Darrieus machine, there was a two-bladed Savonius wind rotor in the upper part and a Darrieus machine in the lower side. The result showed that $C_p$ with 20% overlap is higher than 16.2% without overlap. They also concluded that the improvement of $C_p$ can be achieved for the Savonius-Darrieus wind machine compared with the general Savonius rotor.

Irabu and Roy [7] introduced a guide-box tunnel to improve the $C_p$ of Savonius wind rotors and prevent the damage by strong wind disaster. The guide-box tunnel was like a rectangular box as wind passage and the test wind rotor was included. It was able to adjust the inlet mass flow rate by its variable area ratio between the inlet and outlet. The experimental results showed that the maximum $C_p$ of the two-bladed wind rotor using the guide-box tunnel is about 1.23 times of that the wind rotor without the guide-box tunnel and 1.5 times of that using a three-bladed wind rotor. Apparently, it verified that the two-bladed wind rotor is better than the three-bladed one for converting wind power.

Saha et al. [8] used a wind tunnel to test and investigate the performances by different number of blades and stages, different geometries of blade and inserting valves on the concave side of blade or not. The results were as follows.

First, with an increases of the number of blades, the performance of wind rotor decreases. Second, twisted geometry blade profile has a better performance than the semicircular blade geometry. Third, the $C_p$ of a two-stage Savonius wind rotor is higher than those of single-stage and three-stage wind rotors. Last, the valve-aided Savonius wind rotor with three blades shows a better performance than the conventional wind rotor.

Altan et al. [9] introduced a curtaining arrangement to improve the performance and increase the efficiency of a two-bladed Savonius wind rotor without changing its basic structure. They placed two wind-deflecting plates in front of the wind rotor to prevent the negative torque opposite the wind rotor rotation. The experimental results showed that $C_p$ increase about 38% with an optimum curtain arrangement and it is 16% much higher than that without curtaining.

Antheaume et al. [10] applied the CFD software, Fluent, to investigate the performance of vertical axis Darrieus wind rotor in different working fluids by using $k$-$\varepsilon$ turbulent model under steady-state conditions. They also discussed the average efficiency of several wind rotors connected in parallel pattern. The results showed that increasing the number of wind rotors or decreasing the distance between wind rotors can make the efficiency higher due to the velocity streamlines straightening effect by the configuration. In addition, the performances working in water are much higher than those in air.

Zhao et al. [11] applied the computational fluid dynamics (CFD) software to investigate the performance of new helical Savonius wind rotors. They analyzed the behaviors of the wind rotors with different aspects ratio, number of blades, overlap distance and helical angle. The results showed that three-blade helical wind rotor has lower $C_p$ compared with two-bladed helical wind rotor.

And the best overlap ratio, aspect ratio, and helical angle are 0.3, 6.0 and 180°, respectively.

Howell et al. [12] applied Fluent to investigate the performances of one VAWT in 2-D and 3-D simulations and compared the predictions with experimental data. The turbulence model used was RNG k-ε model, by which the applicability in flow fields involves large flow separations. The error bars on experimental data were fixed at ±20% of measured values. The results showed that the performances predicted by 2-D simulations are apparently higher than those by 3-D simulations and experimental measurements due to the effect of the generation of over tip vortices.

Pope et al. [13] applied Fluent to investigate the performances of zephyr VAWT and compared the predictions with experimental data. By the reason that a free spinning turbine cannot be fully simulated, they used constant rotational speeds of the VAWT in simulations and changed the specification of parameters to reveal freely moving turbine blades in experiments. They indicated that determining the performance at constant rotational speed is valuable since any power generation connected to the electricity grid needs to operate at constant speed.

Shigetomi et al. [14] studied the interactive flow field around two Savonius wind rotors by experimental investigation using particle image velocimetry. They found that there exist power-improvement interactions between two rotating Savonius rotors in appropriate arrangements. The interactions are caused by the Magnus effect to provide the additional rotation of the downstream rotor and the periodic coupling of local flow between two wind rotors. However, they are quite sensitive between two wind rotors to the wind direction so that wind rotors arranged together will lose one of the VAWTs inherent advantages, such as

no influence of wind direction.

Akwa et al. [15] investigated the influence of the buckets overlap ratio of a Savonius wind rotor on the averaged moment and power coefficients in the complete cycles of operation by the commercial software, Star-CCMþ. Numerical simulations of the air flow on the rotor in 40 different situations were carried out. The results showed that the best performance occurs at bucket overlap ratios with values close to 0.15, giving an averaged power coefficient of 0.3161 under the tip speed ratio 1.25. However, in the range of high bucket overlap, the moment and performance of the rotor fall dramatically due to the reduced incidence of air on the concave side of the rotor bucket.

McTavish et al. [16] studied a performance assessment of a novel vertical axis wind turbine by using CFD software, CFdesign 2010. A validation study consisting of steady and rotating simulations was conducted using a Savonius rotor. Fair agreement was obtained by comparing with experimental data. Steady two-dimensional CFD simulations had demonstrated that the new VAWT has the similar average static torque characteristics to existing Savonius rotors. Three-dimensional simulations were conducted at several tip speed ratios with a free stream speed of 6 m/s. The predicted dynamic torque generated by the rotor decays more rapidly with increasing tip speed ratio than the torque output of Savonius rotors due to its asymmetric design and the curvature of the outer rotor wall.

Akwa et al. [17] presented a review on the performance of Savonius wind turbines. Simple construction, high start up and full operation moment, wind acceptance from any direction, low noise and angular velocity in operation, reducing wear on moving parts, are some advantages of using this type of machine. Savonius rotor performance is affected by operational conditions,

geometric and air flow parameters. Each different arrangement of Savonius rotor affects its performance. The range of reported values for maximum averaged power coefficient includes values around 0.05–0.30 for most settings. Performance gains of up to 50% for tip speed ratio of maximum averaged power coefficient are also reported with the use of stators.

Zhou et al. [18] explored the non-linear two-dimensional unsteady flow over a conventional Savonius-type rotor and a Bach-type rotor, and developed a simulation method for predicting their aerodynamic performance. The simulations were performed using Star-CCMþ. A comparative study of the two types of rotors was carried out, and numerical simulation results were compared with experimental data. The results showed that the Bach-type rotor is demonstrated to have better performance for torque and power coefficient than the conventional Savonius-type rotor. A discussion of the causes of these differences was presented that is based on a detailed study of the respective flow field characteristics, including the behavior of moment coefficients, velocity vectors and pressure distribution. A simulation method for further study of new blades shapes was suggested.

Feng [1] applied the computational fluid dynamics (CFD) software, Star-CD, to investigate the flow field around two-bladed Savonius wind rotors and their corresponding performances. The study mentioned that using the parallel matrix arrangement of Savonius wind rotors can get higher power efficiency. It indicated that the parallel matrix system has an optimum $C_p$, which is about 1.45 times of $C_p$ of one single Savonius wind rotor in 3-D simulation.

Huang [2] applied the CFD software, Fluent, to investigate a four two-bladed Savonius wind rotors in parallel matrix system and compared the predicted results with experimental data. For the simulation results, the $C_p$ of

parallel matrix system with curtain is about 1.03 times of that of the system without curtain. Both of those are occurred at TSR 0.8. Besides, The $C_p$ of parallel matrix system with curtain at TSR 0.6 is about 1.16 times of that of the system without curtain. However, the predicted results are higher than the experiment measurements because the resultant $C_p$s in experiments by the generated power, which needs to consider energy transform loss.

## 1.3 Scope of Present Study

This study employs a computational fluid dynamics (CFD) software, Fluent, to analyze the flow fields around two-bladed Savonius wind rotors and their corresponding performances. This research includes three cases: the first one is a study of a single Savonius wind rotor, the second is the parallel matrix system, consisting of four two-bladed Savonius wind rotors, and the last one is the parallel matrix system of ten two-bladed Savonius wind rotors. All of the cases are carried out by the corresponding parametric studies, whose parameters include the wind velocity and tip speed ratio. After that, the influence of wind direction change on the parallel system is also studied. Then, comparisons between the systems mentioned above are discussed.

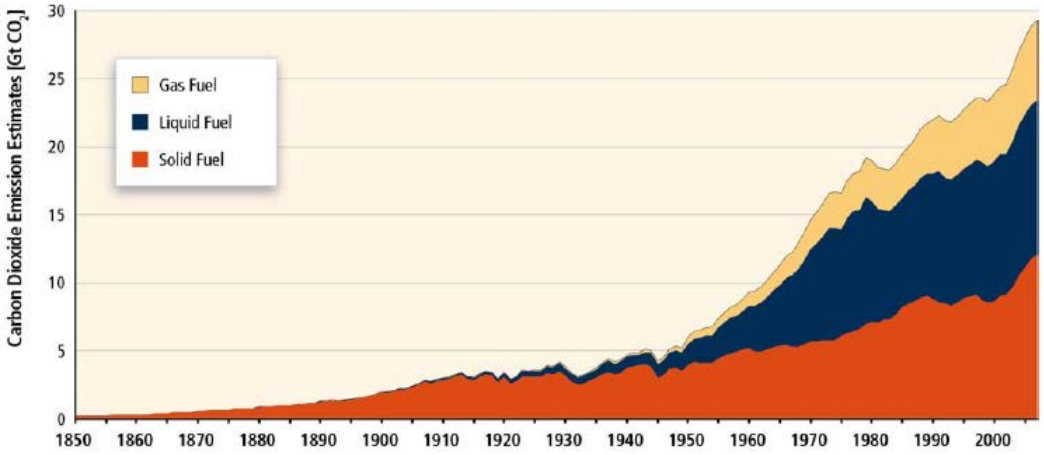


**Fig. 1.1 Global $CO_2$ emissions from fossil fuel burning, 1850 to 2007. Gas fuel includes flaring of natural gas. All emission estimates are expressed in Gt $CO_2$ (Boden and Marland, 2010) [19]**

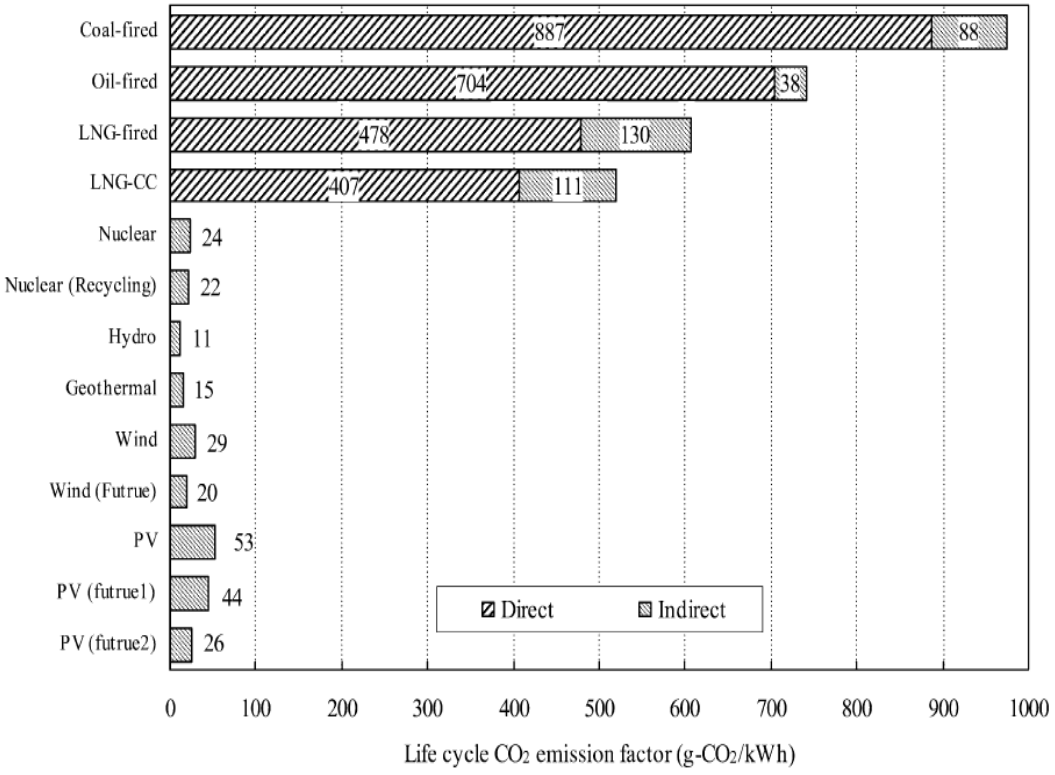


**Fig. 1.2 Life cycle $CO_2$ emission factors for different types of power generation systems [20]**

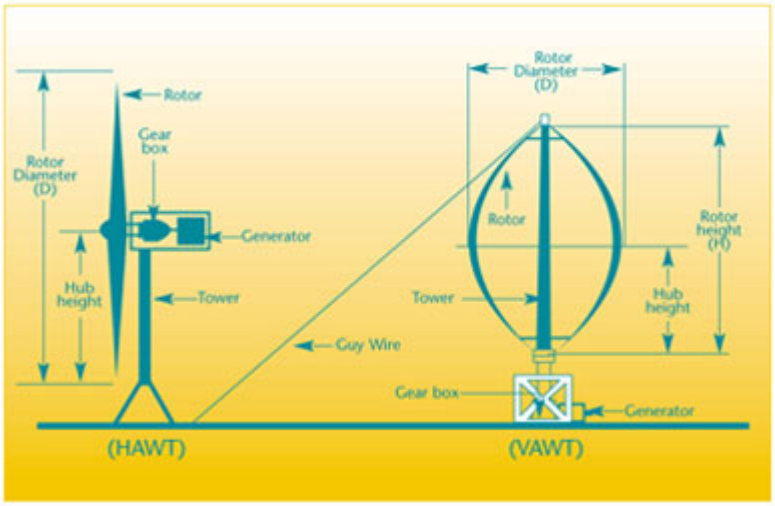


**Fig. 1.3 Structures of wind turbine [21]**

**Fig. 1.4 Wake effect from wind turbine picture (Riso National Laboratory, Denmark) [22]**

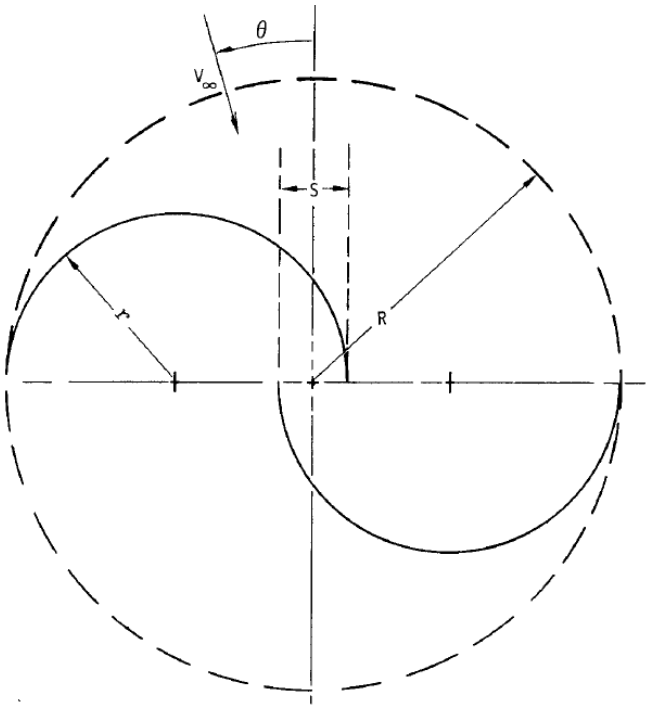


**Fig. 1.5 Schematic of a two-bladed Savonius wind rotor [4]**

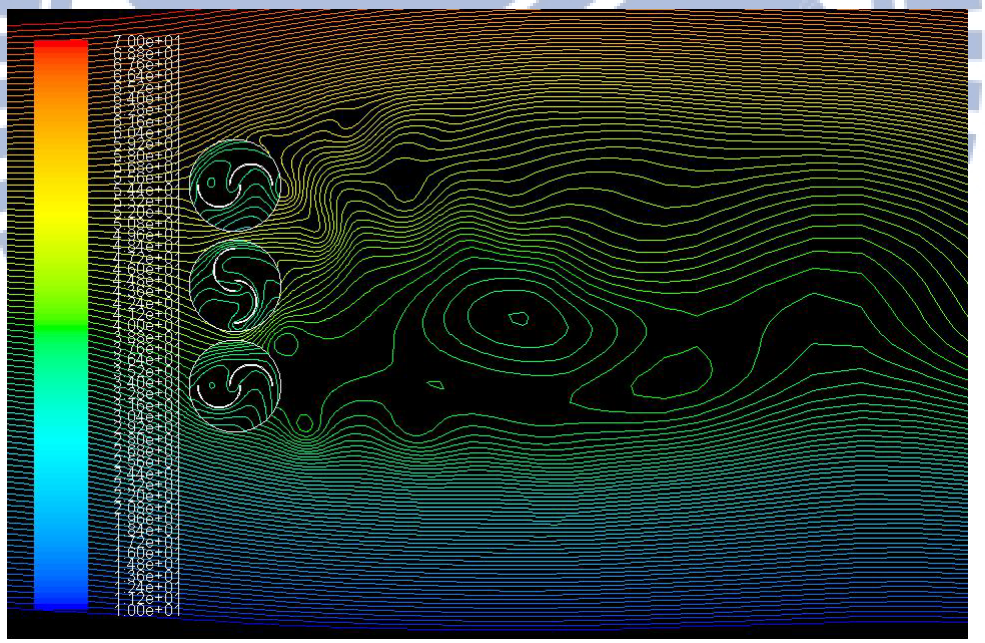

**Fig. 1.6 Streamlines around three Savonius wind rotors with phase angle 90° difference. [1]**

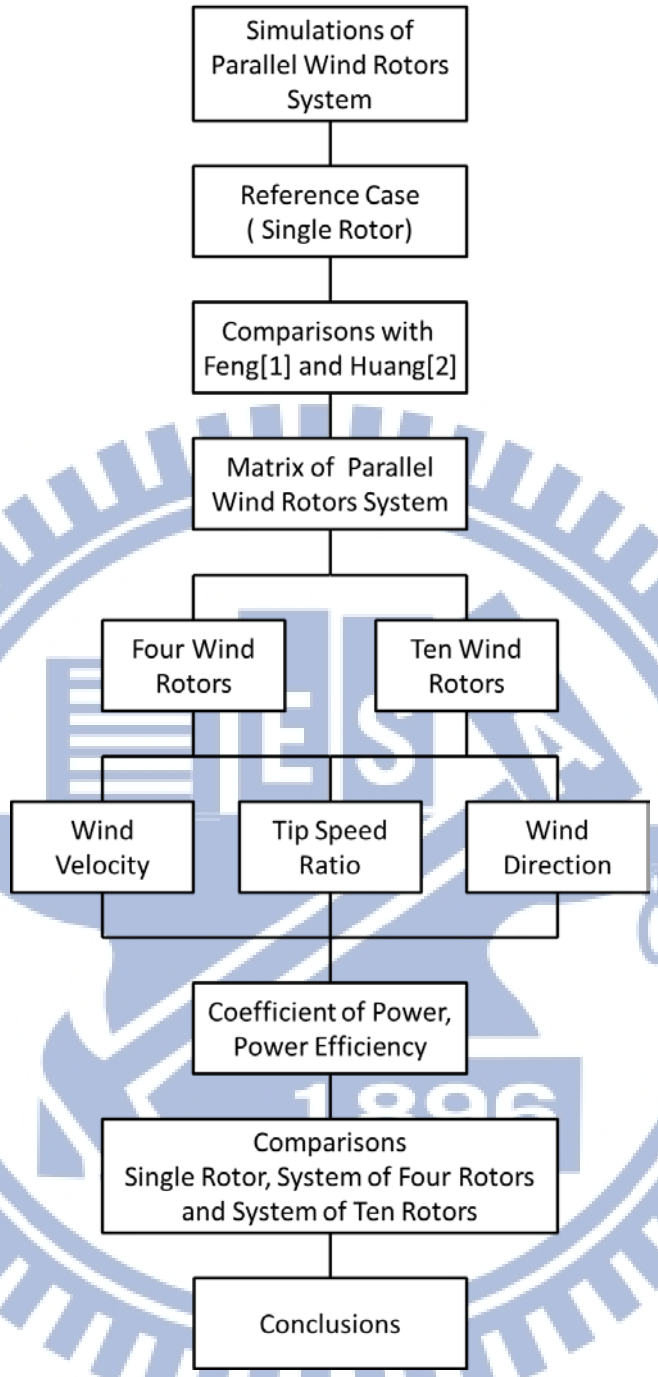


**Fig. 1.7 The scope of this study**

# CHAPTER 2

# FUNDAMENTALS OF WIND ENERGY

## 2.1 Brief History of Wind Energy

The wind energy has been used for thousands of years such as sailing, grinding grains, irrigation and drawing water. The first windmill appeared in Europe can be traced back to the twelfth century. The first wind machine was known as appearing about 2200 years ago in Persia for grinding grains. Then the Romans used the same way for the same purpose around 250 A.D. By the fourteenth century, the Dutch employed windmills to drain water in the low-lying areas of the Rhine River delta. After many years developing, the Netherlands used windmill to drain wetlands from the fourteenth century onwards and become an economy developed country gradually. Professor James Blyth built an experiment of windmill to produce electricity in Scotland in July 1887. The first use of windmill for producing electricity was in 1888. And the first such windmill was built and used by Charles Brush in Ohio, U.S.A. Ten years later, about 72 wind turbines were being used to produce electricity in the range of about 5 to 25kW.

In the twentieth century, wind turbines were used around the world. Because the first wind power station was established in Denmark in 1891, wind power became an important part of a decentralized electrification in the first quarter of the twentieth century. There existed many small electricity generating sites in Denmark, and wind power was a large part of them. In Australia, small wind generators were used to provide power at isolated post offices and farms. In

America, rural farms had used wind power originally. Eventually, this generated electricity was connected to grid later. By 1930, windmill had been widely manufactured and used to generate electricity for the distribution system having not yet been installed in America. More than six million wind turbines had been manufactured in American and it was the first time that the utilization of wind energy was based on an industrially mass-produced. Following these experience, American manufacturers started build and sell small wind turbines not only for battery-charging but also for interconnection to electricity networks. The first megawatt wind turbine was built in USA in 1941. In the 1970s and 1980s, the U.S. government promoted the technologies for the large-scale commercial wind turbines. NASA researched many of the turbine designs under this project that still is used today.

In the end of 2002, there was roughly 32 GW of power supplied from wind energy in the world. Europe has been the leader in wind power utilization, contributing 76% of the total. In 2006, roughly 65GW of rated power were installed in wind farms worldwide, of which more than 47GW located in Europe, and more than 11GW in the United States.

## 2.2 Basic of Wind Energy Conversion

### 2.2.1 Power Conversion and Power Coefficient

From the expression for kinetic energy in flowing air, the power contained in the wind passing an area A with the wind velocity $v_1$ is:

$$P_W = \frac{\rho}{2} A v_1^3 \tag{2-1}$$

where $\rho$ is air density, depending on air pressure and moisture. For practical calculations it may be assumed $\rho \approx 1.225 kg/m^3$. The air streams in axial

direction through the wind turbine, of which *A* is the swept area. The useful mechanical power obtainment is expressed by means of the power coefficient *Cp*:

$$P = C_p \frac{\rho}{2} A v_1^3 \tag{2-2}$$

Supposing the wind velocity of airflow is homogeneous, the value ahead of the turbine plane is $v_1$. After passing through the retardation of wind turbine, suffers retardation due to the power conversion to a speed $v_3$ far behind the wind turbine. Due to the power conversion, wind velocity $v_1$ reduce to a velocity $v_3$, as shown in **Fig. 2.1**, a simplified theory could be claimed that the velocity can be represented in an average value $v_2$, where $v_2 = (v_1+v_3)/2$, in the retardation where the moving blades located. On this basis, Betz has shown by a simple calculation that the maximum useful power can be obtained for $v_3/v_1 = 1/3$ in 1920; where the power coefficient $C_p = 16/27 \approx 0.593$. In reality, wind turbine displays the maximum values $C_p$, max = 0.4 ~ 0.5 due to losses, such as profile loss, tip loss and loss due to wake rotation. In order to determine the mechanical power available for the load machine, such as electrical generator or pump, Eq. (2-2) has to be multiplied with an efficiency of the drive train, taking losses in bearings, couplings and gear boxes into account.

An important parameter of wind rotor is the tip-speed ratio (TSR), $\lambda$. It is defined as a ratio of the circumferential velocity of blade tips to the wind speed:

$$\lambda = {}^{u}/_{v_1} = \frac{D}{2} \cdot \frac{\omega}{v_1} \tag{2-3}$$

where *D* is the outer turbine diameter and $\omega$ the angular wind rotor speed. Considering that in the rotating mechanical system, the power is the product of torque *T* and angular speed $\omega$ $(P = T \bullet \omega)$, then $C_p$ becomes

$$C_p = \frac{P}{P_W} = \frac{T \cdot \omega}{\frac{1}{2}\rho A v_1^3} \tag{2-4}$$

**Fig. 2.2** shows typical characteristics $C_p$ $(\lambda)$ for different types of wind rotors. Besides the constant maximum value according to Betz, as well as the figure indicates a revised curve $C_p$ by Schmitz, who takes the downstream deviation from axial air flow direction into account. The difference is notable in the region of lower tip speed ratios.

### 2.2.2 Wind Rotor Blades Using Aerodynamic Drag or Lift

Extract the airflow power to mechanical power without considering design of wind rotor blades. The momentum theory by Betz indicates the physically based, ideal limit value for the extraction of mechanical power from free-stream airflow without considering the design of the energy converter. However, the power which can be achieved under real conditions cannot be independent of the characteristics of the energy converter. The fundamental difference for various rotor blade designs depends on what kind aerodynamic force is utilized to produce the mechanical power. The first fundamental difference which considerably influences the actual power depends on which aerodynamic forces are utilized for producing mechanical power. As the wind rotor blades are subjected to airflow, the generated aerodynamic drag is parallel to the flow direction, whereas the lift is perpendicular to flow direction. The real power coefficients obtained are greatly dependent on whether aerodynamic drag or aerodynamic lift is used.

#### 2.2.2.1 Drag Devices

The simplest type of wind energy conversion can be achieved by means of pure drag surfaces as shown in **Fig. 2.3**. The air impinges on the surface $A$ with wind velocity $v$, and then the drag $D$ can be calculated from the air density $\rho$, the

surface area $A$, the wind velocity $u$ and the aerodynamic drag coefficient $C_D$ as

$$D = C_D \frac{1}{2} \rho A v_r^2 = C_D \frac{1}{2} \rho A (v - u)^2 \quad (2\text{-}5)$$

The relative velocity, $v_r = v - u$, which effectively impinges on the drag area, is determined by wind velocity $v$ and blade rotating speed $u = \omega RM$, in which $RM$ is the mean radius. Then the resultant power is

$$P = D \cdot u = \frac{1}{2} \rho A v^3 \left[ C_D \left(1 - \frac{u}{v}\right)^2 \frac{u}{v} \right] = \frac{1}{2} \rho A v^3 C_p \quad (2\text{-}6)$$

Analog to the approach described in Chapter 2.2.1, it can be shown that $Cp$ reaches a maximum value with a velocity ratio of $u/v = 1/3$. The maximum value of $C_p$ is then

$$C_{p,max} = \frac{4}{27} C_D \quad (2\text{-}7)$$

It is taken into account that the aerodynamic drag coefficient $C_D$ of a concave surface curved against the wind direction can hardly exceed a value of 1.3. Thus, the maximum power coefficient $C_p$, max of a general drag-type wind rotor becomes about 0.2, only one third of Betz's ideal $C_p$ value of 0.593.

#### 2.2.2.2 Lift Devices

Utilization of aerodynamic lift on wind rotor blade can achieve much higher power coefficients. The lift blade design employs the same principle that enables airplanes to fly. As shown in **Fig. 2.4**, when air flows over the blade, a pressure gradient creates between the upper and the lower blade surfaces. The pressure at the lower surface is greater than upper surface. Thus, the difference of pressure produces a lift force to uplift the blade. The lift force occurred on a body by wind can be calculated from the air density $\rho$, acting area $A$, wind velocity $v$ and aerodynamic lift coefficient $C_L$ as

$$L = C_L \frac{1}{2} \rho A v^2 \quad (2\text{-}8)$$

When blades are attached to the central axis of a wind rotor, the lift force is translated into rotational motion. All of the modern wind rotor types are designed for utilizing this effect, and the best type suited for this purpose is with a horizontal rotational axis. The aerodynamic force created is divided into a component in the direction of free-stream velocity, the drag force *D*, and a component perpendicular to the free-stream velocity, the lift force *L*. The lift force *L* can be further divided into a component $L_{torque}$ in the plane of rotation of the wind rotor, and a component $L_{thrust}$ perpendicular to the plane of rotation. $L_{torque}$ constitutes the driving torque of the wind rotor.

Modern airfoils, developed for aircraft wings and which are also applied in wind rotors, have an extremely favorable lift-to-drag ratio. It could show a qualitative utilization of how much an aerodynamic lift force uses as a driving force would have more efficiency. However, it is no longer possible to calculate the power coefficients of lift-type wind rotors quantitatively with the aid of elementary physical relationships alone.

## 2.3 Vertical and Horizontal Axis Wind Rotors

Wind rotors are approximately classified into two general types by their orientations: horizontal axis type and vertical axis type. A horizontal axis wind rotor has its blades rotating on an axis parallel to the ground and a vertical axis one has its blades rotating on an axis perpendicular to the ground. There are a number of designs for both, and each type has certain advantages and disadvantages. There are numerous designs for both type rotors with different concerns, which are related to diverse situations. Generally, the number of

vertical axis wind rotor for commercial uses is much less than that of horizontal axis wind rotor.

### 2.3.1 Wind Rotors with a Vertical Axis of Rotation

The oldest design of wind rotors is fabricated in vertical axis of rotation. At the beginning, vertical-axis wind rotors could only be built for using aerodynamic drag. It was only recently that engineers succeeded in developing vertical-axis designs which could also utilize aerodynamic lift effectively. Darrieus proposed such design, considered as a promising concept for modern wind turbines in 1925. The Darrieus wind rotor resembles a gigantic eggbeater and the geometric shape of the wind rotors blades is complicated that is difficult to manufacture. A wind rotor, called H-rotor, also utilizes aerodynamic lift force. Instead of curved wind rotor blades, the straight blades are connected to the wind rotor shaft by struts.

Furthermore, Savonius wind rotor, which is investigated in this research, is also one type of vertical-axis wind rotors. The wind rotor was invented by a Finnish engineer, Savonius in 1922. The structure of Savonius wind rotor is simple with a shape of character “S”, so it is also called S-rotor. Savonius wind rotor is one of the simplest wind rotors to manufacture. Because it is a drag-typed device, Savonius wind rotor extracts much less wind energy than the other similarly-sized lift-type wind rotor, but it has higher starting torque.

### 2.3.2 Horizontal Axis Wind Rotors

The earliest design of this type of wind turbine was the big Dutch-style windmill, primarily used for milling grain. Another early type of these turbines was the windmill that was built on almost all farms in the early twentieth century.

This type of wind turbines is the dominant design principle in wind energy technology today. The undisputed superiority of this design to date is primarily based on the reason that the wind rotor blade shape can be aerodynamically optimized and the highest efficiency can be achieved when aerodynamic lift is utilized appropriately.

These turbines usually need to adjust the angle of the entire wind rotor with the change of wind direction. They achieve the objective by using a yaw system which can move the entire wind rotor left or right in small increments. They can also control the wind rotor torque and power output by adjusting the blade angle using the pitching mechanism. However, designs differing from standard concept are also common and simplifications of construction, such as the absence of the pitching mechanism, can be found, particularly in small wind turbines.

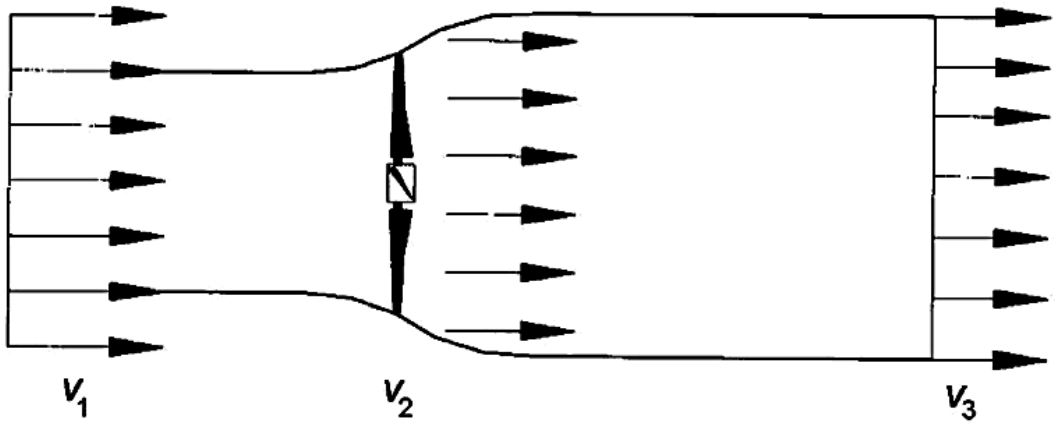


**Fig. 2.1 Idealized fluid model for a wind rotor [23]**

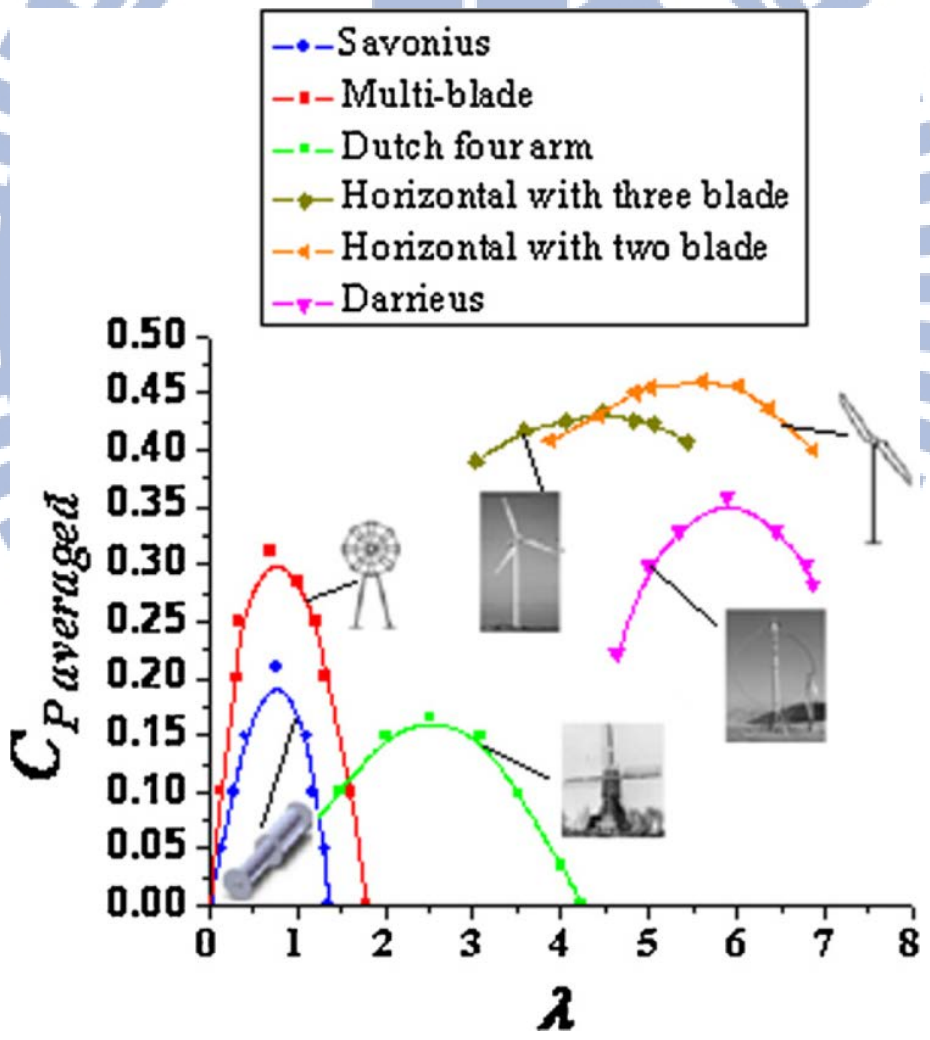


**Fig. 2.2 Characteristic curves of $C_{P\,averaged}$ as a function of $\lambda$ for various wind turbines. [17]**

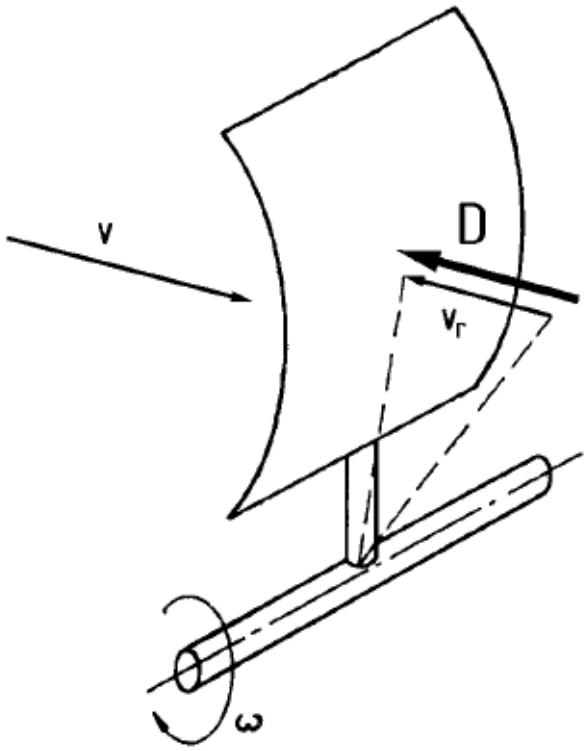


**Fig. 2.3 Flow conditions and aerodynamic forces with a drag device [24]**

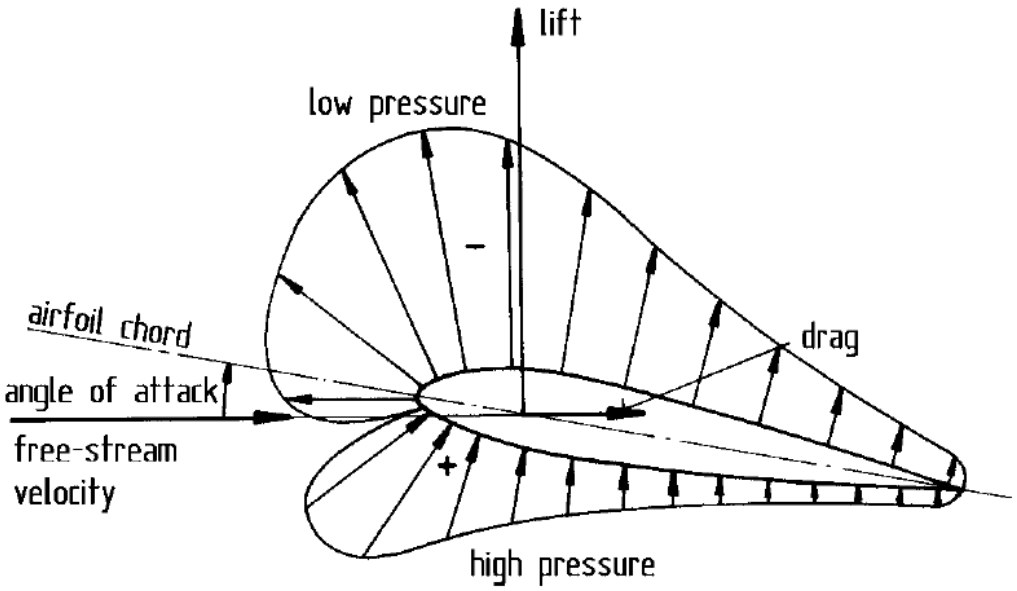


**Fig. 2.4 Aerodynamic forces acting on an airfoil exposed to an air stream [24]**

# CHAPTER 3

# MATHEMATICAL MODEL AND NUMERICAL ALGORITHM

## 3.1 Domain Description

In this work, the air flow fields around a single rotating Savonius wind rotor, the parallel matrix system with four Savonius wind rotors and the parallel matrix system with ten Savonius wind rotors are analyzed numerically under different tip-speed ratios by employing Fluent. The geometry of a two-bladed Savonius wind rotor was given in **Fig. 1.5** and the corresponding information is summarized in **Table 3.1**. And, the geometry of real wind rotor is shown in **Fig. 3.1**.

**Table 3.1 Geometrical Data**

| | |
|---|---|
| Number of Blades | 2 |
| Rotor Blade Diameter (m) | 0.9 |
| Overlap Ratio of Blades | 0.15 |

In order to compare the power efficiencies between one single Savonius wind rotor and the parallel matrix systems, three types of rectangular domains are set up and shown in **Figs. 3.2, 3.3** and **3.4**, respectively. The corresponding dimensions of these domains are listed in **Table 3.2**. For the case of parallel matrix system, the distance between each wind rotors is set as 1.5 m.

**Table 3.2 Dimensions of Computational Domains**

| | Length | Width |
|---|---|---|
| One single Savonius wind rotor (m) | 24.3 | 9.9 |
| The parallel matrix system with four wind rotors (m) | 24.3 | 9.9 |
| The parallel matrix system with ten wind rotors (m) | 24.3 | 29.7 |

Furthermore, the domains including ten Savonius wind rotors with different wind directions are set as shown in **Fig. 3.5**, and the angles of wind direction are 0°, 37°, 53° and 90°. For simplification, it does not include the consideration of the shaft of wind rotors.

## 3.2 Governing Equations

In order to make the model tractable, some assumptions are given as follow:

1. The flow is incompressible and turbulent.
2. The heat transfer and buoyancy effects are neglected.

Based on the assumptions mentioned above, the governing equations are given below.

### 3.2.1 The Continuity and Momentum Equation

Turbulent flows are characterized by fluctuating velocity field. In Reynolds averaging, the solution variables in the instantaneous (exact) Navier-Stokes

equations are decomposed into the mean (ensemble-averaged or time-averaged) and fluctuating components. For the velocity components:

$$u_i = \overline{u_i} + u_i' \tag{3-1}$$

where $\overline{u_i}$ and $u_i'$ are the mean and fluctuating velocity components ( $i$ = 1, 2, 3). Likewise, for pressure and other scalar quantities:

$$\phi = \overline{\phi} + \phi' \tag{3-2}$$

where $\phi$ denotes a scalar such as pressure, energy, or species concentration. Substituting expressions of this form for the flow variables into the instantaneous continuity and momentum equations and taking a time (or ensemble) average (and dropping the over-bar on the mean velocity, $\overline{u}$ ) yields the ensemble-averaged momentum equations. They can be written in Cartesian tensor form as:

$$\frac{\partial \rho}{\partial t} + \frac{\partial}{\partial x_j}(\rho u_i) = 0 \tag{3-3}$$

$$\frac{\partial}{\partial t}(\rho u_i) + \frac{\partial}{\partial x_j}\left(\rho u_i u_j\right) = -\frac{\partial P}{\partial x_i} + \frac{\partial}{\partial x_j}\left[\mu\left(\frac{\partial u_i}{\partial x_j} + \frac{\partial u_j}{\partial x_i} - \frac{2}{3}\delta_{ij}\frac{\partial u_l}{\partial x_l}\right)\right] + \frac{\partial}{\partial x_j}(-\rho\overline{u_i' u_j'}) \tag{3-4}$$

Eqs. (3-3) and (3-4) are called Reynolds-averaged Navier-Stokes (RANS) equations. They have the same general form as the instantaneous Navier-Stokes equations with the velocities and other solution variables now representing ensemble-averaged (or time-averaged) values. Additional terms now appear that represent the effects of turbulence. The Reynolds stress term, $-\rho\overline{u_i' u_j'}$, must be modeled in order to close Eq. (3-4).

### 3.2.2 RNG *k*-*ε* Model

The RNG-based *k*-*ε* turbulence model is derived from the instantaneous Navier-Stokes equations, using a mathematical technique called "renormalization group" (RNG) methods. The analytical derivation results in a model with constants different from those in the standard *k*-*ε* model. The additional terms and functions in the transport equations for *k* and *ε* are also different.

#### 3.2.2.1 Transport Equations for the RNG *k*-*ε* Model

The turbulence kinetic energy, *k*, and its rate of dissipation, *ε*, are obtained from the following transport equations:

$$\frac{\partial}{\partial t}(\rho k) + \frac{\partial}{\partial x_i}(\rho k u_i) = \frac{\partial}{\partial x_j}\left(\alpha_k \mu_{eff} \frac{\partial k}{\partial x_j}\right) + G_k - \rho\varepsilon + S_k \quad (3\text{-}5)$$

and

$$\frac{\partial}{\partial t}(\rho\varepsilon) + \frac{\partial}{\partial x_i}(\rho\varepsilon u_i) = \frac{\partial}{\partial x_j}\left(\alpha_\varepsilon \mu_{eff} \frac{\partial \varepsilon}{\partial x_j}\right) + C_{1\varepsilon}\frac{\varepsilon}{k}(G_k) - C_{2\varepsilon}\rho\frac{\varepsilon^2}{k} - R_\varepsilon + S_\varepsilon \quad (3\text{-}6)$$

The term of $G_k$ represents the production of turbulence kinetic energy. Using the exact equation for the transport of *k*, this term may be defined as $G_k = -\rho\overline{u_i' u_j'}\frac{\partial u_j}{\partial x_i}$. The quantities $\alpha_k$ and $\alpha_\varepsilon$ are the inverse effective Prandtl numbers for *k* and *ε*, respectively. $S_k$ and $S_\varepsilon$ are user-defined source terms.

#### 3.2.2.2 Modeling the Turbulent Viscosity

The scale elimination procedure in RNG theory produces a differential equation for turbulent viscosity:

$$d\left(\frac{\rho^2 k}{\sqrt{\varepsilon\mu}}\right) = 1.72\frac{\hat{\nu}}{\sqrt{\hat{\nu}^3 - 1 + C_\nu}}d\hat{\nu} \quad (3\text{-}7)$$

where

$$\hat{\nu} = \mu_{eff}/\mu,$$

$$C_\nu \approx 100$$

Eq. (3-7) is integrated to obtain an accurate description of how the effective turbulent transport varies with the effective Reynolds number (or eddy scale), allowing the model to be better handled in the low-Reynolds-number and near-wall flows.

In the high-Reynolds-number limit, Eq. (3-7) gives

$$\mu_t = \rho C_\mu \frac{k^2}{\varepsilon} \tag{3-8}$$

with $C_\mu$ = 0.0845, derived using RNG theory.

**3.2.2.3 RNG Swirl Modification**

Turbulence, in general, is affected by rotation or swirl in the mean flow. The RNG model in Fluent provides an option to account for the effects of swirl or rotation by modifying the turbulent viscosity appropriately. The modification takes the following functional form:

$$\mu_t = \mu_{t0}\, f(\alpha_s, \Omega, \frac{k}{\varepsilon}) \tag{3-9}$$

where $\mu_{t0}$ is the value of turbulent viscosity calculated without the swirl modification using either Eq. (3-7) or Eq. (3-8). $\Omega$ is a characteristic swirl number evaluated within Fluent, and $\alpha_s$ is a swirl constant that assumes different values depending on whether the flow is swirl-dominated or only mildly swirling. This swirl modification always takes effect for axisymmetric, swirling flows and three-dimensional flows when the RNG model is selected. For mild swirling flows (the default in Fluent), $\alpha_s$ is set to 0.07. For strong swirling flows, however, a higher value of $\alpha_s$ can be used.

### 3.2.2.4 Calculating the Inverse Effective Prandtl Numbers

The inverse effective Prandtl numbers, $k$ and $\varepsilon$, are computed using the following formula derived analytically by the RNG theory:

$$\left|\frac{\alpha-1.3929}{\alpha_0-1.3929}\right|^{0.6321}\left|\frac{\alpha+2.3929}{\alpha_0+2.3929}\right|^{0.3769}=\frac{\mu_{mol}}{\mu_{eff}} \tag{3-10}$$

where $\alpha_0 = 1.0$. In the high-Reynolds-number limit ($\frac{\mu_{mol}}{\mu_{eff}} \ll 1$), $\alpha_k = \alpha_\varepsilon \approx 1.393$.

### 3.2.2.5 The $R_\varepsilon$ in the $\varepsilon$ Equation

The main difference between the RNG and standard $k$-$\varepsilon$ models lies in the additional term in the $\varepsilon$ equation given by

$$R_{\varepsilon=}\frac{C_\mu\rho\eta^3(1-\eta/\eta_0)}{1+\beta\eta^3}\frac{\varepsilon^2}{k} \tag{3-11}$$

where $\eta \equiv S_k / \varepsilon$, $\eta_0 = 4.38$, $\beta = 0.012$.

The effects of this term in the RNG $\varepsilon$ equation can be seen more clearly by rearranging Eq. (3-6). Using Eq. (3-11), the third and fourth terms on the right-hand side of Eq. (3-6) can be merged, and the resultant $\varepsilon$ equation can be rewritten as

$$\frac{\partial}{\partial t}(\rho\varepsilon)+\frac{\partial}{\partial x_i}(\rho\varepsilon u_i) = \frac{\partial}{\partial x_j}\left(\alpha_\varepsilon\mu_{eff}\frac{\partial\varepsilon}{\partial x_j}\right)+C_{1\varepsilon}\frac{\varepsilon}{k}(G_k+C_{3\varepsilon}G_b)-C_{2\varepsilon}^*\rho\frac{\varepsilon^2}{k} \tag{3-12}$$

where $C_{2\varepsilon}^*$ is given by

$$C_{2\varepsilon}^* \equiv C_{2\varepsilon}+\frac{C_\mu\eta^3(1-\eta/\eta_0)}{1+\beta\eta^3} \tag{3-13}$$

In regions where $\eta < \eta_0$, the $R$ term makes a positive contribution, and $C_{2\varepsilon}^*$ becomes larger than $C_{2\varepsilon}$. In the logarithmic layer, for instance, it can be shown that

$\eta \approx 3.0$ gives $C_{2\varepsilon}^{*} \approx 2.0$, which is close in magnitude to the value of $C_{2\varepsilon}^{*}$ in the standard *k*-*ε* model (1.92). As a result, for weakly to moderately strained flows, the RNG model tends to give results largely comparable to the standard *k*-*ε* model.

In regions of large strain rate ($\eta > \eta_0$), however, the *R* term makes a negative contribution, making the value of $C_{2\varepsilon}^{*}$ less than $C_{2\varepsilon}$. In comparison with the standard *k*-*ε* model, the smaller destruction of *ε* augments *ε*, reducing *k* and, eventually, the effective viscosity. As a result, in rapidly strained flows, the RNG model yields a lower turbulent viscosity than the standard *k*-*ε* model.

Thus, the RNG model is more responsive to the effects of rapid strain and streamlining curvature than the standard *k*-*ε* model, which explains the superior performance of the RNG model for certain classes of flows.

#### 3.2.2.6 Model Constant

The model constants $C_{1\varepsilon}$ and $C_{2\varepsilon}$ in Eq. (3-6) have values derived analytically by the RNG theory. These values, used by default in Fluent, are

$$C_{1\varepsilon} = 1.42;\ C_{2\varepsilon} = 1.68$$

### 3.2.3 Standard Wall Functions

The standard wall functions in Fluent are based on the proposal of Launder and Spalding (1974), and have been most widely used for industrial flows.

#### Momentum

The law-of-the-wall for mean velocity yields

$$U^{*} = \frac{1}{k} ln(Ey^{*}) \qquad (3\text{-}14)$$

where

$$U^* \equiv \frac{U_P C_\mu^{1/4} k_P^{1/2}}{\tau_w/\rho} \tag{3-15}$$

$$y^* \equiv \frac{\rho C_\mu^{1/4} k_P^{1/2} y_P}{\mu} \tag{3-16}$$

In which

$k$ = von Karman constant (= 0.487)

$E$ = empirical constant (= 9.793)

$U_P$ = mean velocity of the fluid at point $P$

$K_P$ = turbulent kinetic energy at point $P$

$y_P$ = distance from point $P$ to the wall

$\mu$ = dynamic viscosity of the fluid

## 3.3 Boundary Conditions

In the model domain, there exist boundary conditions for the followings: rotation of the wind rotor, inlet surfaces, outlet surfaces, physical symmetric surfaces, and wall boundary conditions.

### 1. Rotation boundary condition

In the domain of interest mentioned above, boundary conditions are described at the rotating wind rotor, inlet surfaces, outlet surfaces, side surfaces (atmosphere), and walls (curtain).

$$\omega = \frac{2v_1\lambda}{D} \tag{3-17}$$

where $D$ is the outer wind rotor diameter, $\omega$ the angular wind rotor speed, $v_1$ the wind velocity, and $\lambda$ the tip-speed ratio (TSR).

### 2. The inlet boundary condition

The inlet boundary conditions are:

$$u = u_{in}$$

$$v = 0$$

$$w = 0$$

where *u*, *v* and *w* represent the velocity components in X, Y and Z directions, respectively.

**3. The outflow boundary condition**

Outflow boundary conditions are applied at downstream flow exit, where the details of the local velocity and pressure are not known in advance. It is set by Fluent (2010) internally that the mass conservation is definitely maintained.

**4. The symmetrical boundary condition**

In the atmospheric case, the free surface boundary conditions, where the local velocity gradient approximate zero, are applied for side surfaces, provided that the distances are far enough from the center line of the domain. Via a series of numerical tests, the distance between the free surface and center line is chosen five times of the rotor diameter as Akwa et al. [15] do.

**5. Wall boundary condition**

The wall boundary conditions satisfy the no-slip condition that are *u*, *v*, *w* = 0.

## 3.4 Introduction to FLUENT Software

Fluent is a state-of-the-art computer program for modeling fluid flow and

heat transfer in complex geometries. It provides complete mesh flexibility, including the ability to solve the flow problems using unstructured meshes that can be generated about complex geometries with relative ease. Supported mesh types include 2-D triangular/quadrilateral, 3-D tetrahedral/hexahedral/pyramid, and mixed (hybrid) meshes. Fluent also allows refining or coarsening grid based on the flow solution.

Fluent is written in the C computer language and makes full use of the flexibility and power offered by the language. Consequently, true dynamic memory allocation, efficient data structures, and flexible solver control are all possible. In addition, Fluent uses a client/server architecture, which allows it to run as separate simultaneous processes on client desktop workstations and powerful computational servers. This architecture allows for efficient execution, interactive control, and complete flexibility between different types of machines or operating systems.

All functions required to compute a solution and display the results are accessible in Fluent through an interactive, menu-driven interface.

## 3.5 Numerical Method

This study employs the computational fluid dynamics software Fluent to analyze the flow fields around rotating Savonius wind rotors. The finite volume iteration and SIMPLE algorithm are put in use to solve the governing equations of a transient flow field. And the corresponding grid movement is also solved by using sliding mesh method.

Fluent uses Segregated Solver method to solve the governing integral equations for the conservation of mass and momentum, and (when appropriate)

for energy and other scalars such as turbulence and chemical species. In case a control-volume-based technique is used that consists of:

1. Division of domain into discrete control volumes using a computational grid.
2. Integration of the governing equations on the individual control volumes to construct algebraic equations for the discrete dependent variables such as velocities, pressure, temperature, and conserved scalars.
3. Linearization of the discretized equations and solutions of the resultant linear equation system yield updated values of the dependent variables.

### 3.5.1 Segregated Solution Method

Using this approach, the governing equations are solved sequentially (i.e., segregated from one another). Because the governing equations are non-linear (and coupled), several iterations of the solution loop must be performed before a converged solution is obtained. Each time of iteration consists of the steps illustrated in **Fig. 3.6** and outlined below:

1. Fluid properties are updated, based on the current solution. (If the calculation has just begun, the fluid properties will be updated based on the initialized solution.)
2. The *u*, *v*, and *w* momentum equations are each solved in turn using current values for pressure and face mass fluxes, in order to update the velocity field.
3. Since the velocities obtained in Step 2 may not satisfy the continuity equation locally, a Poisson-type equation for the pressure correction is derived from the continuity equation and the linearized momentum equations. This pressure correction equation is then solved to obtain the necessary

corrections to the pressure and velocity fields and the face mass fluxes that continuity is satisfied.

4. Where appropriate equations for scalars such as turbulence, energy, species, and radiation are solved using the previously updated values of the other variables.
5. When inter-phase coupling is to be included, the source terms in the appropriate continuous phase equations may be updated with a discrete phase trajectory calculation.
6. A check for convergence of the equation set is made. These steps are continued until the convergence criteria are met.

### 3.5.2 Linearization: Implicit

In the segregated solution method the discrete, non-linear governing equations are linearized to produce a system of equations for the dependent variables in every computational cell. The resultant linear system is then solved to yield an updated flow-field solution.

The manner in which the governing equations are linearized may take an implicit form with respect to the dependent variable (or set of variables) of interest. The implicit form is described in the following:

**Implicit**

For a given variable, the unknown value in each cell is computed using a relation that includes both existing and unknown values from neighboring cells. Therefore each unknown will appear in more than one equation in the system, and these equations must be solved simultaneously to give the unknown quantities.

In the segregated solution method each discrete governing equation is

linearized implicitly with respect to that equation's dependent variable. This will result in a system of linear equations with one equation for each cell in the domain. Because there is only one equation per cell, this is sometimes called a scalar system of equations. A point implicit (Gauss-Seidel) linear equation solver is used in conjunction with an algebraic multi-grid (AMG) method to solve the resultant scalar system of equations for the dependent variable in each cell. For example, the *x*-momentum equation is linearized to produce a system of equations in which *u*-velocity is the unknown. Simultaneous solution of this equation system (using the scalar AMG solver) yields an updated *u*-velocity field.

In summary, the segregated approach solves for a single variable field (e.g., p) by considering all cells at the same time. It then solves for the next variable field by again considering all cells at the same time, and so on. There is no explicit option for the segregated solver.

### 3.5.3 Discretization

Fluent uses a control-volume-based technique to convert the governing equations to algebraic equations that can be solved numerically. This control volume technique consists of integrating the governing equations about each control volume, yielding discrete equations that conserve each quantity on a control volume basis.

Discretization of the governing equations can be illustrated most easily by considering the steady-state conservation equation for transport of a scalar quantity $\phi$. This is demonstrated by the following equation written in integral form for an arbitrary control volume *V* as follows:

$$\oint \rho\phi\vec{v} \cdot d\vec{A} = \oint \Gamma_\phi \nabla\phi \cdot d\vec{A} + \oint_V S_\phi dV \qquad (3\text{-}18)$$

where

$\rho$ = density

$\vec{v}$ = velocity vector

$\vec{A}$ = surface area vector

$\Gamma_\phi$ = diffusion coefficient for $\phi$

$\nabla\phi$ = gradient of $\phi$

$S_\phi$ = source of $\phi$ per unit volume

Eq. (3-18) is applied to each control volume, or cell, in the computational domain. The two-dimension, triangular cell shown in **Fig. 3.7** is an example of such a control volume. Discretization of Eq. (3-18) on a given cell yields

$$\sum_f^{N_{faces}} \rho_f \overrightarrow{v_f} \phi_f \cdot \overrightarrow{A_f} = \sum_f^{N_{faces}} \Gamma_\phi (\nabla\phi)_n \cdot \overrightarrow{A_f} + S_\phi V \qquad (3\text{-}19)$$

where

$N_{faces}$ = number of faces enclosing cell

$\phi_f$ = value of $\phi$ convected through face $f$

$\rho_f \overrightarrow{v_f} \cdot \overrightarrow{A_f}$ = mass flux through the face

$\overrightarrow{A_f}$ = area of face $f$

$(\nabla\phi)_n$ = magnitude of $\nabla\phi$ normal to face $f$

$V$ = cell volume

The equations solved by Fluent take the same general form as the one given above and apply readily to multi-dimension, unstructured meshes composed of arbitrary polyhedral.

By default, Fluent stores discrete values of the scalar $\phi$ at the cell center (c0 and c1 in **Fig. 3.7**). However, face values $\phi_f$ are required for the convection

terms in Eq. (3-19) and must be interpolated from the cell center values. This is accomplished using an upwind scheme.

**First-Order Upwind Scheme**

When first-order accuracy is desired, quantities at cell faces are determined by assuming that the cell-center values of any field variable represent a cell-average value and hold throughout the entire cell; the face quantities are identical to the cell quantities. Thus when first-order upwind is selected, the face value $\phi_f$ is set equal to the cell-center value of $\phi$ in the upstream cell.

### 3.5.4 Simple Algorithm

The SIMPLE algorithm uses a relationship between velocity and pressure corrections to enforce mass conservation and to obtain the pressure field.

If the momentum equation is solved with a guessed pressure field $p^*$, the resulting face flux $J_f^*$, computed from $J_f = \hat{J}_f + d_f(p_{c0} - p_{c1})$ (where $p_{c0}$ and $p_{c1}$ are the pressures within the two cells on either side of the face, and $\hat{J}_f$ contains the influence of velocities in these cell. The term $d_f$ is a function of $\overline{a}_p$, the average of the momentum equation $\overline{a}_p$ coefficients for the cells on either side of face *f*.)

$$J_f^* = \hat{J}^*{}_f + d_f(p_{c0}^* - p_{c1}^*) \tag{3-20}$$

does not satisfy the continuity equation. Consequently, a correction $J_f'$ is added to the face flux $J_f^*$ so that the corrected face flux, $J_f$

$$J_f = J_f^* + J_f' \tag{3-21}$$

satisfies the continuity equation. The SIMPLE algorithm postulates that $J_f'$ be written as

$$J_f' = d_f(p_{c0}' + p_{c1}') \tag{3-22}$$

where $p'$ is the cell pressure correction.

The SIMPLE algorithm substitutes the flux correction equations, Eq. (3-21) and (3-22), into the discrete continuity equation ($\sum_f^{N_{faces}} J_f A_f = 0$) to obtain a discrete equation for the pressure correction $p'$ in the cell:

$$a_p p' = \sum_{nb} a_{nb} p_{nb}' + b \tag{3-23}$$

where the source term *b* is the net flow rate into the cell:

$$b = \sum_f^{N_{faces}} J_f^* A_f \tag{3-24}$$

The pressure-correction equation, Eq. (3-23), may be solved using the algebraic multigrid (AMG) method. Once a solution is obtained, the cell pressure and the face flux are used correctly.

$$p = p^* + \alpha_p p' \tag{3-25}$$

$$J_f = J_f^* + d_f(p_{c0}' - p_{c1}') \tag{3-26}$$

Here $\alpha_p$ is the under-relaxation factor for pressure. The corrected face flux $J_f$ satisfies the discrete continuity equation identically during each time of iteration.

### 3.5.5 Sliding Mesh

The sliding mesh model allows adjacent grids to slide relative to one another. In doing so, the grid faces do not need to be aligned on the grid interface. This setup requires a means of computing the flux across the two non-conformal

interface zones of each grid interface.

To compute the interface flux, the intersection between the interface zones is determined at each new time step. The resulting intersection produces one interior zone (a zone with fluid cells on both sides) and one or more periodic zones. If the problem is not periodic, the intersection produces one interior zone and a pair of wall zones (which will be empty if the two interface zones completely intersect), as shown in **Fig. 3.8**. The resultant interior zone corresponds to where the two interface zones overlap; the resultant periodic zone corresponds to where they do not. The number of faces in these intersection zones will vary as the interface zones move relative to one another. Principally, fluxes across the grid interface are computed using the faces resulting from the intersection of the two interface zones (rather than from the interface zone faces themselves).

In the example shown in **Fig. 3.9**, the interface zones are composed of faces A-B and B-C, and faces D-E and E-F. The intersection of these zones produces the faces a-d, d-b, b-e, etc. Faces produced in the region where the two cell zones overlap (d-b, b-e, and e-c) are grouped to form an interior zone, while the remaining faces (a-d and c-f) are paired up to form a periodic zone. To compute the flux across the interface into cell IV, for example, face D-E is ignored and faces d-b and b-e are used instead, bringing information into cell IV from cells I and III, respectively.

## 3.6 Computational Procedure of Simulation

The complete operating procedure by using Fluent package software is carried out through the following processes sequentially.

### 3.6.1 Model Geometry

Before Fluent calculations, it is necessary to build a model. This study used the pre-processor software Gambit to build the geometry of the model. Divide the geometry into finite volumes in order to generate grids conveniently. The details of geometry information can be referred to Section 3.1.

### 3.6.2 Grid Generation

After building the geometry, the model has to use the pre-processor Gambit to generate grids as shown in **Fig. 3.10**. This step defines the different grid sizes in different volumes. The smaller grid size for the small volume will increase the accuracy of the simulation, but it also produce larger grid number which cause calculation difficulty. To consider the appropriate grid size for grid generation is important. The grid generation usually reduced the calculation cost under acceptable accuracy.

### 3.6.3 FLUENT Calculation

To determine and solve the important features of the problem follow the basic procedural steps and get the results. Before starting Fluent, create the model geometry and grid as mentioned in **3.6.1** and **3.6.2**. Then starts Fluent with choose an appropriate solver for 2-D or 3-D modeling. In the beginning, import the mesh grid file and check the grid. After that, various settings and parameters need to be confirmed. Select the solver formulation and choose the basic equations (e.g., laminar, turbulent, inviscid, chemical species, or heat transfer models, etc.) to solve the problem. Identify additional models needed such as fans, heat exchangers, porous media, etc. Specify material properties and the boundary conditions. Adjust the solution control parameters. Give an

initialized value for iterate the flow field model. Finish those foregoing steps, start to calculate a solution and examine the results. If necessary, refine the grid or consider revisions to the numerical or physical model.

### 3.6.4 Grid-Independence Test

The grid-independence test should be taken in advance to have a trade-off between the acceptable accuracy and an affordable calculation resource. As described in Section 3.1, there are three types of rectangular domains: one single Savonius wind rotor, the parallel matrix system with four Savonius wind rotors and the parallel matrix system with ten Savonius wind rotors. The grid-independence tests in 2-D simulations of these three types are carried out first.

In the case of one single Savonius wind rotor, the boundary conditions of wind velocity and tip-speed ratio are 7 m/s and 0.4. Grid numbers of 11244, 11296, 12339, 12794, 13749, 15192 and 16993 in x-y plane are tested and the simulation results are shown in **Fig. 3.11(a)** and **Table 3.3**. Because the changing rate of $C_p$ from grid number 13749 to 15192 is small enough and remains almost the same value while the grid number increases, the grid number of 13749 is chosen.

The grid numbers of 12476, 13500, 14363, 16682, 19110, 22406 and 27442 in x-y plane are tested in the case of the parallel matrix system with four Savonius wind rotors. The results are shown in **Fig. 3.11 (b)** and **Table 3.4**. The boundary conditions for this case adopt wind velocity as 7 m/s and tip-speed ratio as 0.4. The same reason as the case of one single Savonius wind rotor, grid numbers 22406 is selected accordingly.

After that, in the case of the parallel matrix system with ten Savonius wind

rotors, the boundary conditions of wind velocity and tip-speed ratio are 7 m/s and 0.4. Grid numbers of 15703, 17689, 17858, 20595, 25027, 32683 and 36541 in x-y plane are tested and the simulation results are shown in **Fig. 3.11 (c)** and **Table 3.5**. The same reason as the case of one single Savonius wind rotor, grid numbers 32683 is selected accordingly.

Following the procedure for the grid-independence tests of one single Savonius wind rotor in x-y plane, the grid number of the parallel matrix system with four Savonius wind rotors domain and the grid number of the parallel matrix system with ten Savonius wind rotors domain are set accordingly. The set grid numbers of these three domains are listed in **Table 3.6.**

**Table 3.3 Grid-independence Tests in the case of one single Savonius wind rotor**

| Grid Number (x-y Plane) | $C_p$ | Changing Rate |
|---|---|---|
| 11,244 | 0.1528 | - |
| 11,296 | 0.1558 | 0.019685 |
| 12,339 | 0.1582 | 0.015383 |
| 12,794 | 0.1613 | 0.019219 |
| 13,749 | 0.1632 | 0.011865 |
| 15,192 | 0.1621 | -0.00632 |
| 16,993 | 0.1637 | 0.009291 |

**Table 3.4 Grid-independence Tests in the case of the parallel matrix system with four Savonius wind rotors**

| Grid Number (x-y Plane) | $C_p$ | Changing Rate |
|---|---|---|
| 12,476 | 0.2504 | - |
| 13,500 | 0.2603 | 0.039397 |
| 14,363 | 0.2669 | 0.025515 |
| 16,682 | 0.2678 | 0.003245 |
| 19,110 | 0.2750 | 0.026895 |
| 22,406 | 0.2823 | 0.026812 |
| 27,442 | 0.2820 | -0.001153 |

**Table 3.5 Grid-independence Tests in the case of the parallel matrix system with ten Savonius wind rotors**

| Grid Number (x-y Plane) | $C_p$ | Changing Rate |
|---|---|---|
| 15,703 | 0.2835 | - |
| 17,689 | 0.2896 | 0.021258 |
| 17,858 | 0.2897 | 0.000617 |
| 20,595 | 0.2892 | -0.00183 |
| 25,027 | 0.2970 | 0.026746 |
| 32,683 | 0.3160 | 0.063987 |
| 36,541 | 0.3069 | -0.02872 |

**Table 3.6 Grid Numbers of all the Domains**

| | Grid Number (2-D) |
|---|---|
| One single Savonius wind rotor | 13,749 |
| The parallel matrix system with four Savonius wind rotors | 22,406 |
| The parallel matrix system with ten Savonius wind rotors | 32,683 |

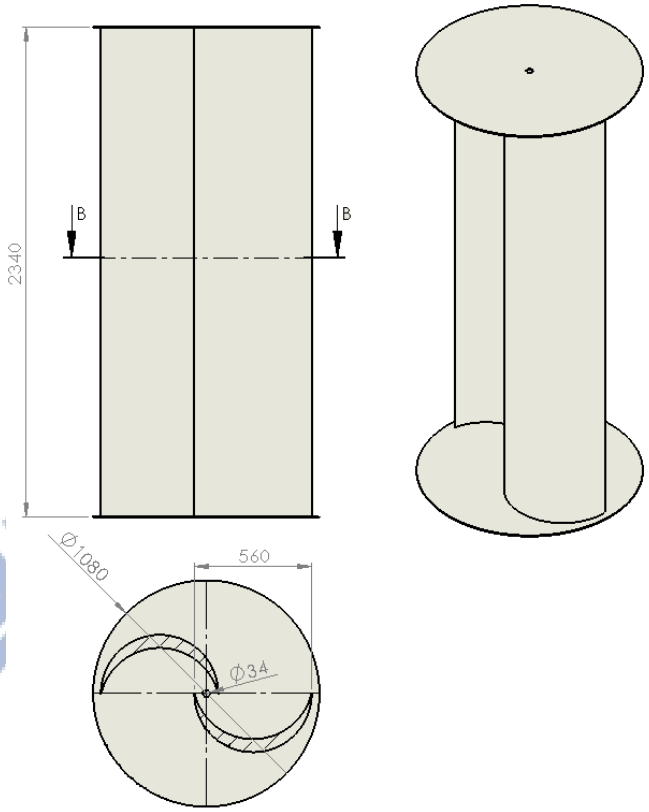


**Fig. 3.1 Schematics of Savonius wind rotor geometry in experimental study**

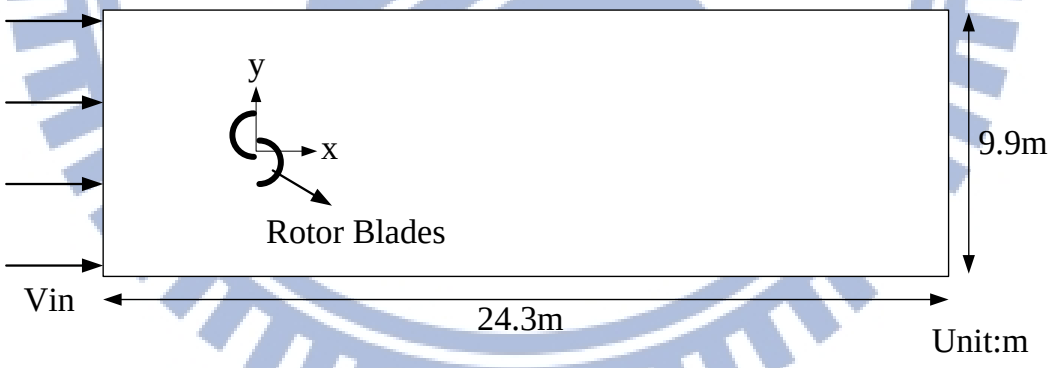


**Fig. 3.2 The domain of one single Savonius wind rotor**

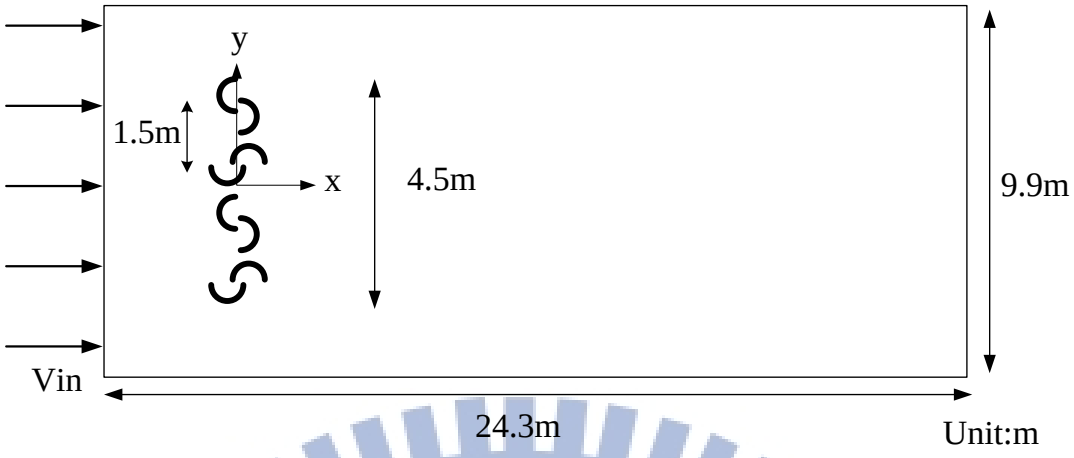


**Fig. 3.3 The domain of four two-bladed Savonius wind rotors in parallel matrix system**

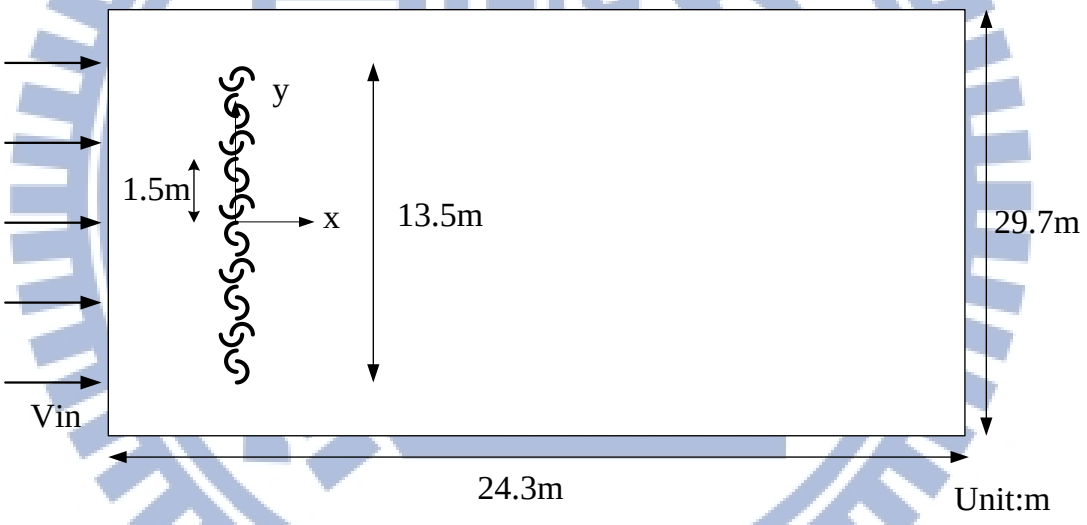


**Fig. 3.4 The domain of ten two-bladed Savonius wind rotors in parallel matrix system**

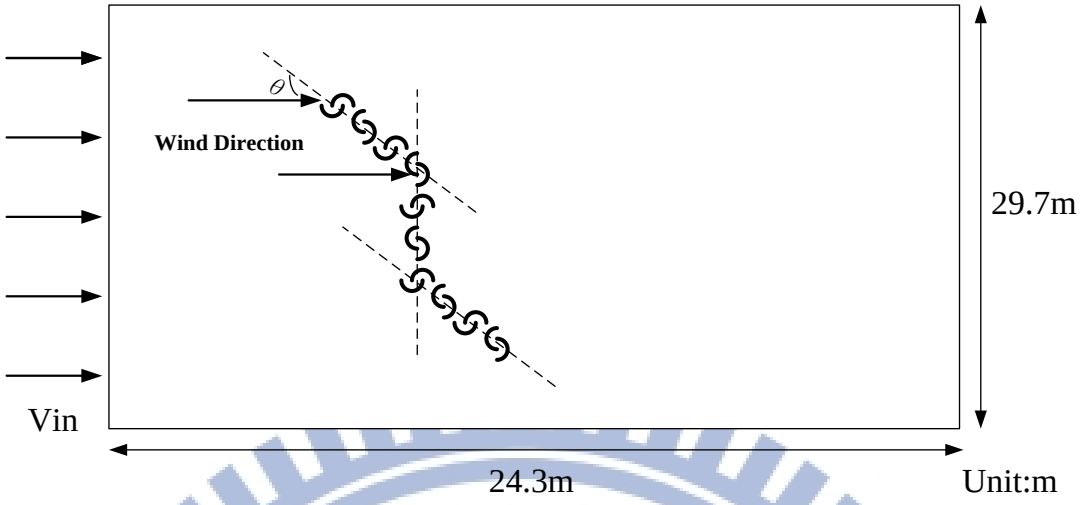


**Fig. 3.5 The domain for ten two-bladed Savonius wind rotors with different wind direction (θ=0°, 37°, 53°, 90°)**

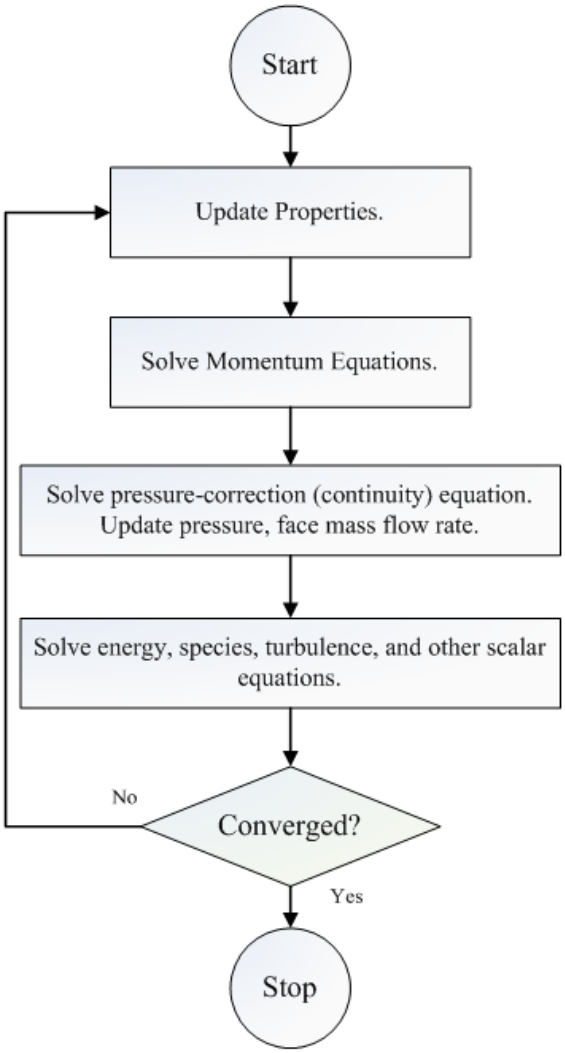


**Fig. 3.6 Overview of the segregated solution method**

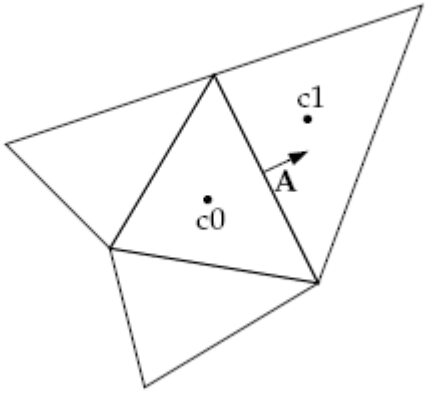


**Fig. 3.7 Control volume used to illustrate discretization of a scalar transport equation**

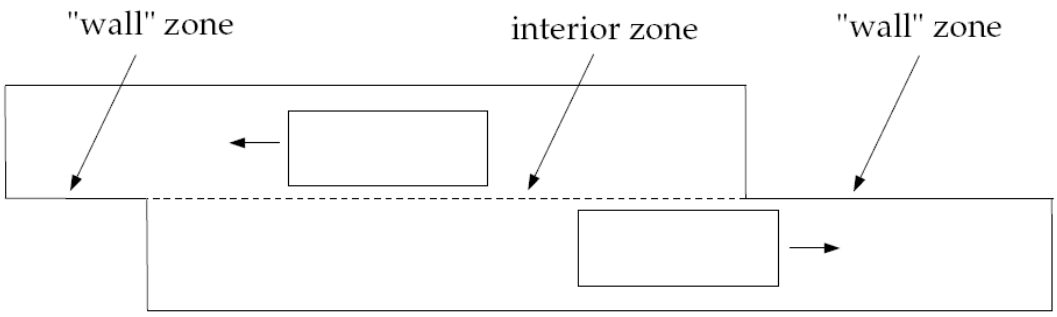


**Fig. 3.8 Zones created by non-periodic interface intersection**

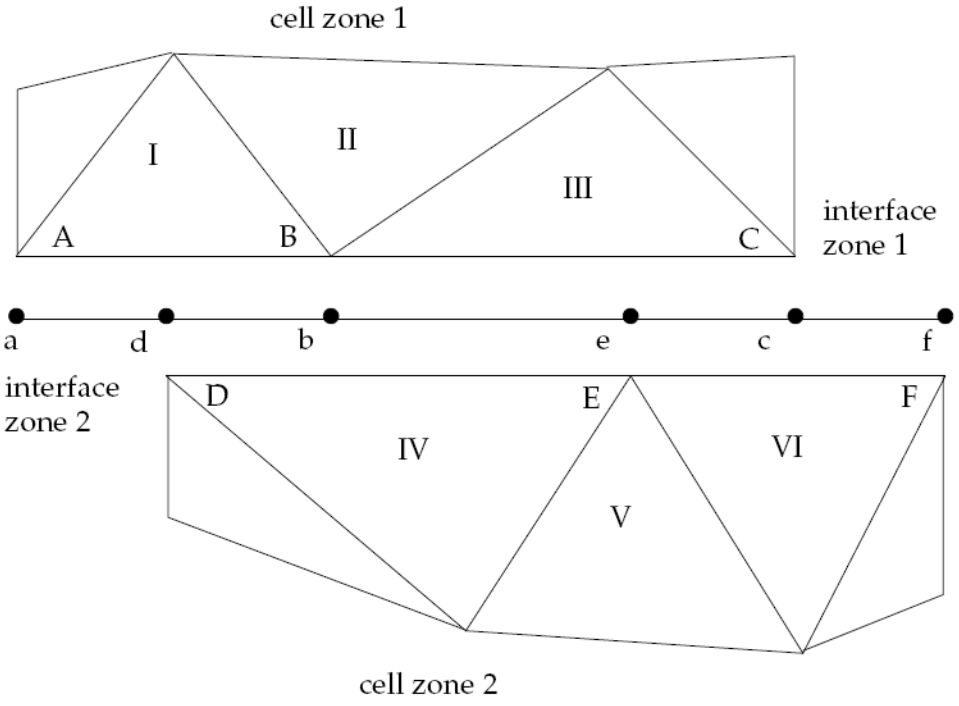


**Fig. 3.9 Two-dimensional grid interface**

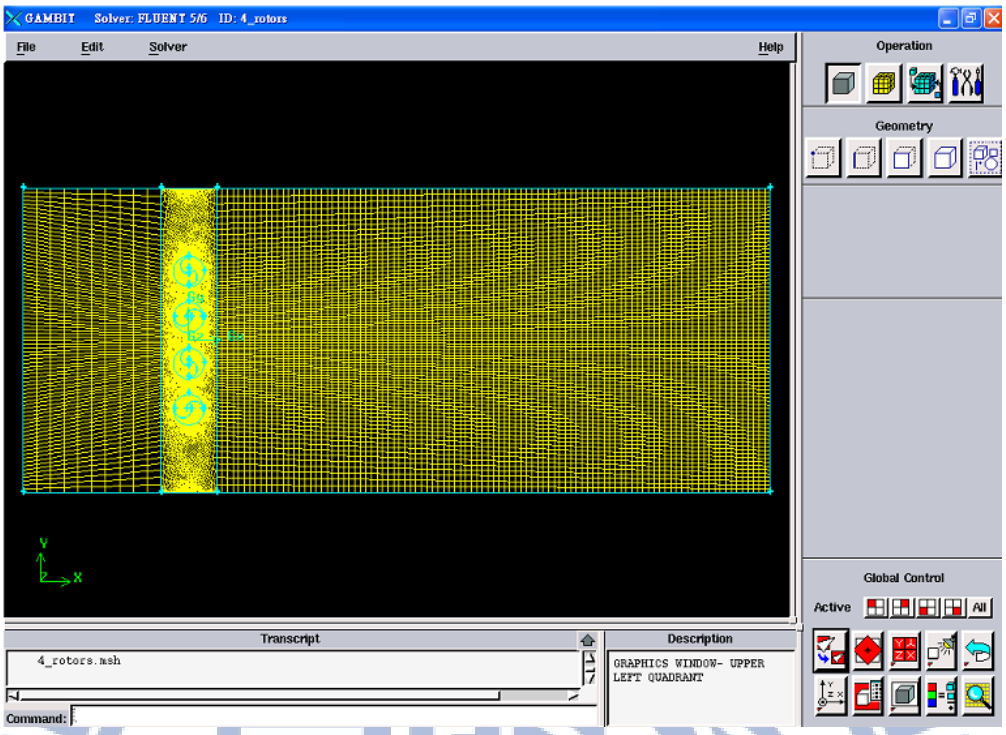


**Fig. 3.10 User interface of Gambit**

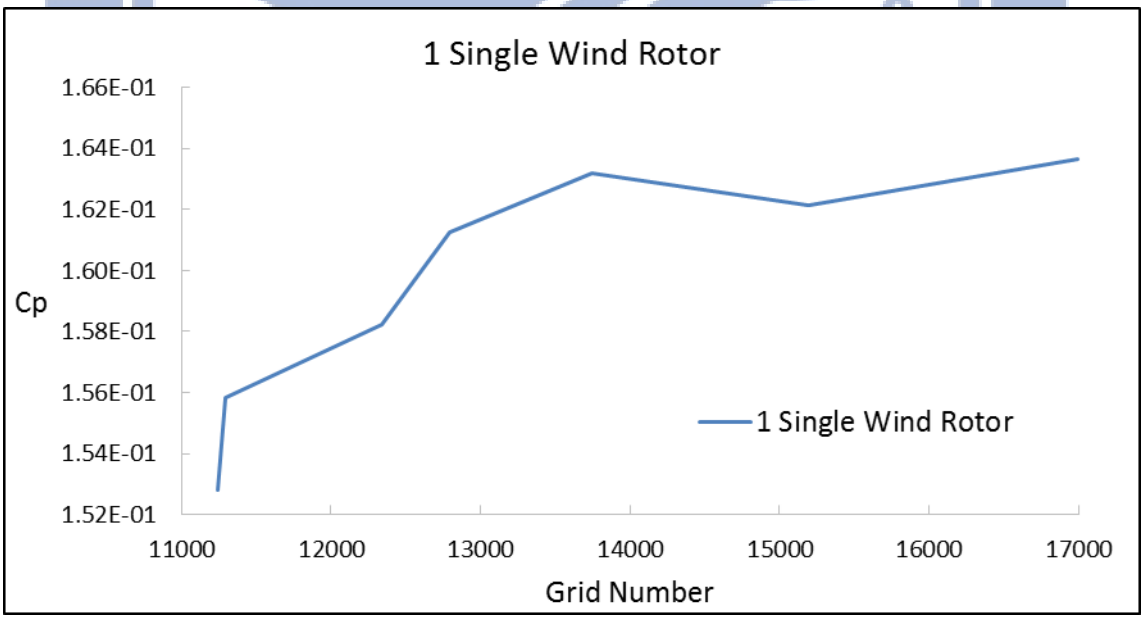


**(a)**

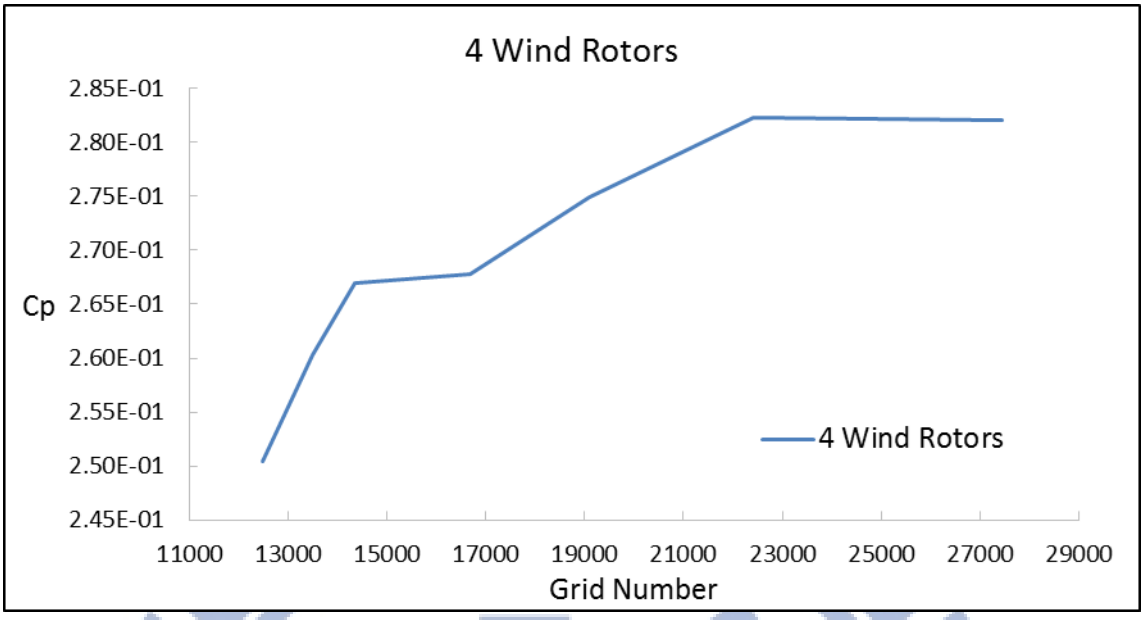


**(b)**

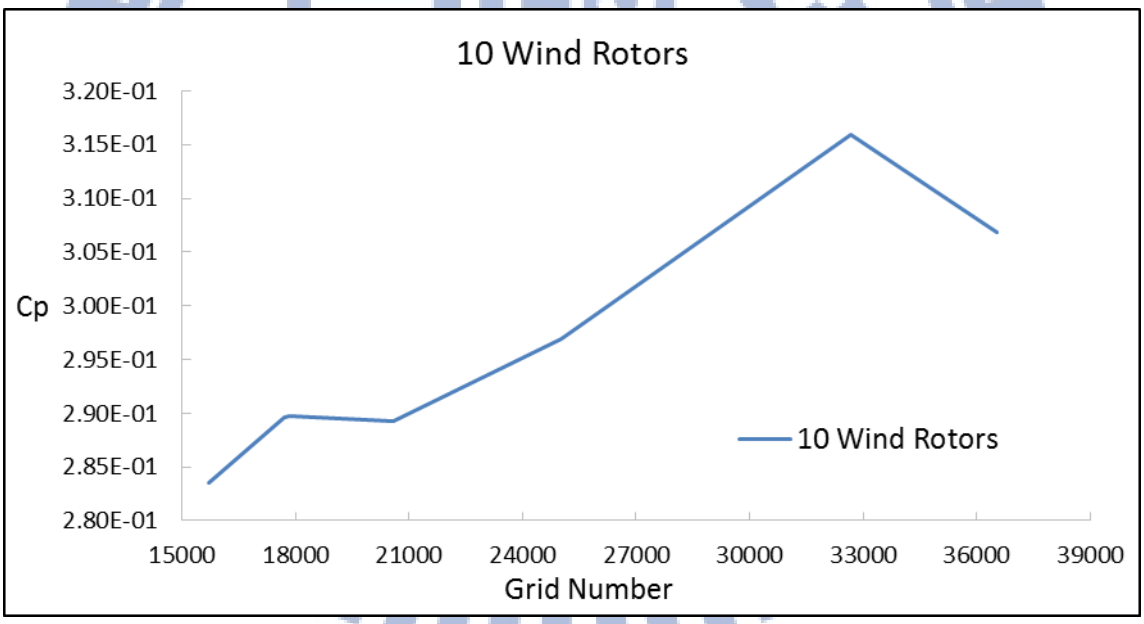


**(c)**

**Fig. 3.11 Grid-independence tests: (a) one single Savonius wind rotor; (b) the parallel matrix system with four Savonius wind rotors; (c) the parallel matrix system with ten Savonius wind rotors**

# CHAPTER 4

# RESULTS AND DISCUSSION

This study employs the computational fluid dynamics (CFD) software, Fluent, to analyze the flow fields around two-bladed Savonius wind rotors and their corresponding performances. The working fluid in this research is air with density 1.225 kg/ $m^3$ and molecular viscosity $1.79\times10^{-5}$ kg/ m-s.

The research flow chart was already shown in **Fig. 1.7**. It includes three cases: the first one is a study of one single Savonius wind rotor, demonstrated in Section 4.1; the second is the parallel matrix system, consisting of four two-bladed Savonius wind rotors, shown in Section 4.2; the last one, Section 4.3, is the parallel matrix system of ten two-bladed Savonius wind rotors. All of the cases are carried out by their corresponding parametric studies, whose parameters include the wind velocity and tip speed ratio. As to the influence of wind direction change on the parallel system, it is only given in Section 4.3. Finally, comparisons between the systems mentioned above are discussed in Section 4.4.

## 4.1 One Single Savonius Wind Rotor in 2-D Simulation

### 4.1.1 One Single Savonius Wind Rotor and Reference Case

Such simulation procedure in the present thesis is the same as the references of Feng [1] and Huang [2] with different rotor configuration (see **Fig. 4.1** and **Table 4.1**). From **Table 4.1**, the diameter is 0.9 m in present study, 0.9 m in Feng's simulation [1], 1.08 m in Huang's simulation [2], respectively. The overlap ratio of blades is 0.15 in present study, 0.15 in Feng's simulation [1], 0.196 in Huang's simulation [2], respectively. From **Figs. 4.1 (a)**, **(b) and (c)**,

the shape of blade is semicircle and the thickness of blade is the same in present study, the blade, whose shape can be referred to **Fig. 4.1 (c)** in Huang's predictions [2]**.** On the other hand, the blade used by Feng's predictions [1] does not consider the thickness effect.

**Table 4.1 Geometry of Savonius wind rotor: present thesis; Feng [1]; Huang [2]**

| | Present Thesis | Feng [1] | Huang [2] |
|---|---|---|---|
| Number of Blades | 2 | 2 | 2 |
| Diameter (m) | 0.9 | 0.9 | 1.08 |
| Overlap Ratio of Blades | 0.15 | 0.15 | 0.196 |

The Savonius wind rotor rotates under a predetermined load given by motor in the steady wind speeds of 7 or 14 m/s, respectively. The free spinning wind rotor cannot be fully simulated, because the turbine load is not considered in simulations. The method in simulations is to specify constant rotational speeds and change the parameters.

To compare with Feng's predictions [1], Huang's predictions [2] and experimental measurements by Howell et al. [12], the 2-D simulations are carried out with a specified wind speed of 7m/s and 14 m/s. The parametric study is based on the variation of tip speed ratio (TSR) ranged from 0.4 to 1.2. The simulated $C_p$ results as a function of TSR for one single Savonius wind

rotor are shown in **Figs. 4.2 (a)** and **4.2 (b)**, which Feng's predictions [1], Huang's predictions [2] and Howell et al.'s measurements [12] are also included. In one single Savonius wind rotor simulations with wind speed of 7m/s, the maximum values of $C_p$ are 0.191 at TSR 0.8 in present study, 0.234 at TSR 0.9 in Feng's simulation [1], 0.255 at TSR 1.1 in Huang's simulation [2] and 0.241 at TSR 0.86 in experiment by Howell et al. [12], respectively. And in one single Savonius wind rotor simulations with wind speed of 14m/s, the maximum values of $C_p$ are 0.193 at TSR 0.8 in present study, 0.236 at TSR 0.9 in Feng's simulation [1] and 0.24 at TSR 0.87 in experiment by Howell et al. [12], respectively. The reasons that lead to the discrepancy with Feng's predictions [1], Huang's predictions [2] and Howell et al. [12] are the different geometry of wind rotor blade.

The two dimensional simulations are carried out with the wind speeds of 7 and 14m/s and the tip speed ratios ranged from 0.4 to 1.2. The 2-D model uses a grid number of 13,749. The parameters used are summarized in **Table 4.2**.

**Table 4.2 Parameters for one single Savonius wind rotor**

| | |
|---|---|
| Wind Speed | 7 m/s and 14 m/s |
| Tip-Speed Ratio | 0.4 ~ 1.2 |
| Simulation Domain | 2-D (24.3m × 9.9m) |

The 2-D predictions of one single Savonius wind rotor in wind speeds of 7m/s and 14 m/s are shown in **Table 4.3** and **Fig. 4.3**. In 2-D simulations, the maximum of $C_p$ is 0.191 at wind speed 7 m/s and 0.193 at 14 m/s. It also can be

seen that the $C_p$ in wind speed 14 m/s are slightly higher than that in 7 m/s at the same tip-speed ratio 0.8. It is because the Reynolds number around the blades increases with wind speed, causing a delayed separation is shown in **Figs. 4.4 (a)** and **(b)**. Therefore, the drags on the advancing blades decrease and then cause a higher $C_p$.

**Table 4.3 Comparisons of the maximum $C_p$s between one single Savonius wind rotor in 2-D simulation**

| | Wind Speed (m/s) | Maximum $C_p$ |
|---|---|---|
| One Single Savonius Wind Rotor | 7 | 0.191 |
| | 14 | 0.193 |

In order to observe the flow field, α is firstly defined as the angle of rotating wind blade relative to the initial angle and illustrated in **Fig. 4.5**. In 2-D simulation, the description of flow field is given for demonstrating the fundamental phenomenon. The resultant torque curve of one single Savonius wind rotor with wind speed 7 m/s and tip-speed ratio 0.8 in a rotation (360°) is shown in **Fig. 4.6**. As shown in this figure, the minimal torque happens at α = 20° and the maximal one happens at α = 100°. At these two positions, the corresponding static pressure fields and velocity vector distributions around the single Savonius wind rotor are demonstrated in **Figs. 4.7** and **4.8**, respectively.

As shown in these two figures, the pressure difference between the front and back sides of the returning blade at α = 20° is apparently higher than that at α =

100°. It also can be seen that a large vortex is generated around the tip at the low-pressure region behind the blade in **Figure 4.7 (a)**. This effect would produce a negative torque and thus causes a lower net torque. On the other hand, at $\alpha = 100°$ in **Figure 4.7 (b)**, the pressure difference is smaller, and the resulted vortices are also smaller. Therefore, the negative torque is reduced, resulting in a higher net torque. Such phenomenon is typical characteristics of drag device, which has high starting torque but low $C_p$ (see Section 2.2.2.1).

The maximums of average power output of one single Savonius wind rotor are calculated and the results are listed in **Table 4.4**.

**Table 4.4 The maximum of average power output of one single Savonius wind rotor**

| Condition | Wind Speed (m/s) | Average Power Output (W/per rotor) |
|---|---|---|
| One Single Savonius Wind Rotor | 7 | 36.12 |
| | 14 | 291.29 |

## 4.2 The Parallel Matrix System with Four Savonius Wind Rotors in 2-D Simulation

Feng [1] numerically studied a parallel matrix system, which includes three Savonius wind rotors with the same angular speed, the specified phase angle and the fixed distance. He found that such disposition can cause constructive interference that improves performance of wind rotor and the best performance occurs at the phase angle difference equal to 90°. These conclusions can be

supported by the numerical simulation of Shigetomi et al. [14], illustrated in **Fig. 4.9**. Therefore, the phase angle difference of 90° is adopted by the present simulation.

In this section, the parallel matrix system, which is consisting of four two-bladed Savonius wind rotors rotating with the same angular speed and the fixed distance, is studied. The domain geometry is shown in **Fig. 3.3** and the corresponding information is also summarized in **Tables 3.1** and **3.2**. The two dimensional simulations are carried out with the wind speeds of 7 and 14m/s and the tip speed ratios ranged from 0.4 to 1.2. The 2-D model uses a grid number of 22,406. The parameters used for this case are summarized in **Table 4.5**.

**Table 4.5 Parameters for the parallel matrix system with four Savonius wind rotors**

| | |
|---|---|
| The Distance between the Two Centers of Savonius Wind Rotors | 1.5m |
| Wind Speed | 7 m/s and 14 m/s |
| Tip-Speed Ratio | 0.4 ~ 1.2 |
| Simulation Domain | 2-D (24.3m × 9.9m) |

### 4.2.1 Four Savonius Wind Rotors in Different Wind Velocity

The 2-D predictions of the parallel matrix system with four Savonius wind rotors in wind speeds of 7m/s and 14 m/s are shown in **Table 4.6**. In 2-D simulations, the maximum of $C_p$ is 0.402 at wind speed 7 m/s and 0.403 at 14 m/s. It also can be seen that the $C_p$ in wind speed 14 m/s are slightly higher than

that in 7 m/s at the same tip-speed ratio 0.9. It is because the Reynolds number around the blades increases with wind speed, causing a delayed separation is shown in **Fig. 4.10**. Therefore, the drags on the advancing blades decrease and then cause a higher $C_p$.

**Table 4.6 Comparisons of the maximum $C_p$s between the parallel matrix system with four Savonius wind rotors in 2-D simulation**

| | Wind Speed (m/s) | Maximum $C_p$ |
|---|---|---|
| The Parallel Matrix System with Four Savonius Wind Rotors | 7 | 0.402 |
| | 14 | 0.403 |

### 4.2.2 Four Savonius Wind Rotors in Different Tip-Speed Ratio

The torque curves of the parallel matrix system with four Savonius wind rotors and one single Savonius wind rotor are shown in **Figure 4.11.** In **Figure 4.11**, it can be seen that for rotors No.1 to 4, each has higher performance than one single rotor. The four wind rotors rotate in the same direction (counterclockwise). The wind departed from rotor No.1 enhances the rotation of No. 2, and so on. When the wind passes through the wind rotor, it causes a low pressure that contributes extra rotation power to adjacent wind rotor. However, there is no wind rotor to enhance the rotation of No.1. But the performance of rotor No.1 is still higher than one single rotor. The static pressure field and velocity vector distribution around parallel matrix system are demonstrated in **Figs. 4.12** and **4.13**, respectively.

For the purpose to analyze flow field more clearly, **Fig. 4.14** shows the streamline distribution derived from 2-D simulation, which has same parameters with present case. The difference between each adjacent stream functions represents the volume flow rate. Therefore, the thinner streamlines has higher velocity and wider streamlines has lower velocity. The higher velocity indicates that wind passes through the wind rotor easily. On the other hand, the lower velocity indicates the wind rotor to be able to absorb more wind work that lets the velocity goes down. Thus, wind rotors produce an asymmetrical flow field that the dense streamlines take place around wind rotor with lower torque; wider streamlines around wind rotor with higher torque.

For this case, the maximum value of $C_p$ is 0.402 at TSR 0.9, given in **Fig. 4.15**. It also reveals that parallel matrix system apparently has higher performance than one single rotor.

The maximums of average power output of the parallel matrix system with four Savonius wind rotors are calculated and the results are listed in **Table 4.7**.

**Table 4.7 The maximum of average power output of the parallel matrix system with four Savonius wind rotors**

| Condition | Wind Speed (m/s) | Average Power Output (W/per rotor) |
|---|---|---|
| The Parallel Matrix System with Four Savonius Wind Rotors | 7 | 76.08 |
| | 14 | 609.44 |

## 4.3 The Parallel Matrix System with Ten Savonius Wind Rotors in

## 2-D Simulation

In this section, the parallel matrix system, which is consisting of ten two-bladed Savonius wind rotors rotating with the same angular speed and the fixed distance, is studied. The domain geometry is shown in **Fig. 3.4** and the corresponding information is also summarized in **Tables 3.1** and **3.2**. The two dimensional simulations are carried out with the wind speeds of 7 and 14m/s and the tip speed ratios ranged from 0.4 to 1.2. The 2-D model uses a grid number of 32,683. The parameters used for this case are summarized in **Table 4.8**.

**Table 4.8 Parameters for the parallel matrix system with ten Savonius wind rotors**

| | |
|---|---|
| The Distance between the Two Centers of Savonius Wind Rotors | 1.5m |
| Wind Speed | 7 m/s and 14 m/s |
| Tip-Speed Ratio | 0.4 ~ 1.2 |
| Simulation Domain | 2-D (24.3m × 29.7m) |

### 4.3.1 Ten Savonius Wind Rotors in Different Wind Velocity

The 2-D predictions of the parallel matrix system with ten Savonius wind rotors in wind speeds of 7m/s and 14 m/s are shown in **Table 4.9**. In 2-D simulations, the maximum of $C_p$ is 0.438 at wind speed 7 m/s and 0.463 at 14 m/s. It also can be seen that the $C_p$ in wind speed 14 m/s are slightly higher than that in 7 m/s at the same tip-speed ratio 0.7. It is because the Reynolds number around the blades increases with wind speed, causing a delayed separation is

shown in **Fig. 4.16**. Therefore, the drags on the advancing blades decrease and then cause a higher $C_p$.

**Table 4.9 Comparisons of the maximum $C_p$s between the parallel matrix system with ten Savonius wind rotors in 2-D simulation**

| | Wind Speed (m/s) | Maximum $C_p$ |
|---|---|---|
| The Parallel Matrix System with Ten Savonius Wind Rotors | 7 | 0.438 |
| | 14 | 0.463 |

### 4.3.2 Ten Savonius Wind Rotors in Different Tip-Speed Ratio

The torque curves of the parallel matrix system with ten Savonius wind rotors and one single Savonius wind rotor are shown in **Figure 4.17**. As shown in **Figure 4.17,** it can be seen that for rotors No.1 to 10, each has higher performance than one single rotor. The ten wind rotors rotate in the same direction (counterclockwise). The wind departed from rotor No.1 enhances the rotation of No. 2, and so on. When the wind passes through the wind rotor, it causes a low pressure that contributes extra rotation power to adjacent wind rotor. However, there is no wind rotor to enhance the rotation of No.1. But the performance of rotor No.1 is still higher than one single rotor. The static pressure field and velocity vector distribution around parallel matrix system are demonstrated in **Figs. 4.18** and **4.19**, respectively.

For the purpose to analyze flow field more clearly, **Fig. 4.20** shows the streamline distribution derived from 2-D simulation, which has same parameters with present case. The difference between each adjacent stream functions

represents the volume flow rate. Therefore, the thinner streamlines has higher velocity and wider streamlines has lower velocity. The higher velocity indicates that wind passes through the wind rotor easily. On the other hand, the lower velocity indicates the wind rotor to be able to absorb more wind work that lets the velocity goes down. Thus, wind rotors produce an asymmetrical flow field that the dense streamlines take place around wind rotor with lower torque; wider streamlines around wind rotor with higher torque.

For this case, the maximum value of $C_p$ is 0.438 at TSR 0.7, given in **Fig. 4.21**. It also reveals that parallel matrix system apparently has higher performance than one single rotor.

### 4.3.3 Ten Savonius Wind Rotors in Different Wind Direction

Feng [1] numerically studied a parallel matrix system, which includes three Savonius wind rotors with the same angular speed, the specified wind direction and the fixed distance on the parallel system. He found that such disposition can cause constructive interference that improves performance of wind rotor and the performance curve of three Savonius wind rotors with different wind directions as shown in **Fig. 4.22**. These conclusions can be supported by the numerical simulation of Shigetomi et al. [14], illustrated in **Fig. 4.9**. Therefore, present study will discuss the effect in different wind directions on the parallel matrix system, which is consisting of ten two-bladed Savonius wind rotors. The different wind directions are due to different arrangement of Savonius wind rotor.

According to the research of Feng [1], the best phase angle difference in such system is 90° and the poorest one is 135°. The suitability of phase angle difference for more energy gained from wind is based on the shape of the two

semicircular blades of these Savonius wind rotors. The higher performance is resulted from the positive interaction between these Savonius wind rotors, and the flow fluctuation plays the major role in contributing to this effect. According to the research of Howell et al. [12], the fluctuation is caused by reasons, such as the potential disturbances around the rotating blades and the large vortex shedding due to the flow separation from the wind rotor's blade. The influence of the fluctuation velocity on the power output is explained by separating the inflow velocity into time average and fluctuation components as following:

$$W = Cu^3$$
$$= C(\overline{u} + u')^3$$
$$= C\left(\overline{u}^3 + 3\overline{u}^2 \cdot u' + 3\overline{u} \cdot u'^2 + u'^3\right)$$
$$\Rightarrow \overline{W} = C\overline{u}^3 \cdot \left[1 + 3\left(\frac{u'}{\overline{u}}\right)^2\right]$$

where C represents the constant to $u^3$ with all the other factors fixed, and the over bar indicates time averaging. Therefore, it can be concluded that the time average power output will increase with the fluctuation of velocity.

This positive interaction by connecting ten Savonius wind rotors in parallel may gain apparently the higher performance, but it might be sensitive to the direction of wind. Therefore, the influence of wind direction on the parallel system is studied now. The system with phase angle difference 90° are chosen with the wind velocity 7 m/s and tip-speed ratio 0.7. The angles of wind direction are 0°, 37°, 53° and 90°. The results are shown in **Fig. 3.5** and **Fig. 4.23**, and a comparison with a single Savonius wind rotor is given as well. In the figure, the change of wind direction will clearly affect and higher the $C_p$ of the parallel matrix system at 0°. When θ = 0°, the $C_p$ is even lower than that of a

single one.

**Figs. 4.24 (a)、(b)、(c)** and **(d)** show the velocity vector distribution around the ten Savonius wind rotors with a wind direction 0°, 37°, 53° and 90°, respectively. And **Figs. 4.25 (a)、(b)、(c)** and **(d)** show the static pressure field around the ten Savonius wind rotors with a wind direction 0°, 37°, 53° and 90°, respectively. As shown in these figures, the above mentioned effect that the pressure difference on the retuning blade is decreased by the effect of the lower wind rotor is reduced due to the changed arrangement relative to the wind direction. The lower wind rotor could not affect the fluid flowing to the region behind the retuning blade of the upper one to reduce the vortex. Therefore, a negative torque is increased and then causes a lower performance. It indicates that the parallel matrix system is strongly influenced by the change of wind direction, representing that one of the advantages in VAWTs is lost.

The maximums of average power output of the parallel matrix system with ten Savonius wind rotors are calculated and the results are listed in **Table 4.10**.

**Table 4.10 The maximum of average power output of the parallel matrix system with ten Savonius wind rotors**

| Condition | Wind Direction | Wind Speed (m/s) | Average Power Output (W/per rotor) |
|---|---|---|---|
| The Parallel Matrix System with Ten Savonius Wind | θ=0° | 7 | 24.87 |
| | | 14 | 252.18 |
| | θ=37° | 7 | 46.35 |
| | | 14 | 427.52 |

| | | | |
|---|---|---|---|
| Rotors | θ=53° | 7 | 57.3 |
| | | 14 | 520.24 |
| | θ=90° | 7 | 82.87 |
| | | 14 | 700.46 |

## 4.4 Comparison between One Single Savonius Wind Rotor and Parallel Matrix Systems

The simulation models are built up to analyze the $C_p$ of the parallel matrix systems and compare with that of one single Savonius wind rotor. The dimensions of the simulation model are shown in **Tables 3.1** and **3.2**. Regarding the boundary conditions, the wind velocity is set to be 7 m/s and 14 m/s, in addition the variation of tip-speed ratio is constrained in the range of 0.4 through 1.2. The predicted $C_p$s of one single Savonius wind rotor and the parallel matrix systems are shown in **Table 4.11** and **Fig. 4.26**. The highest $C_p$ of one single Savonius wind rotor occurs at 0.8 tip-speed ratio and the one of the parallel matrix system with four Savonius wind rotors occurs while the tip-speed ratio is 0.9. In present study, the average $C_p$ of the parallel matrix system with four Savonius wind rotors is 2.07 times higher than that in one single Savonius wind rotor. However, in Huang's predictions [2], which investigates the parallel matrix system with four Savonius wind rotors, the corresponding $C_p$ was 1.46 times higher than that in one single Savonius wind rotor; in Feng's predictions [1], which investigates the parallel matrix system with three Savonius wind rotors, the corresponding $C_p$ is predicted to be 1.9 times higher than that in one single Savonius wind rotor.

**Table 4.11** and **Fig. 4.26** also show that the $C_p$s of one single Savonius

wind rotor in this study are lower than that in Huang [2] at all different tip-speed ratios, but the $C_p$s for the parallel matrix system with four Savonius wind rotors are higher than that in Huang [2]. The reasons that lead to the discrepancy are the different wind blade structures. In addition, the $C_p$s for both single rotor and matrix system at each tip-speed ratio in the present study are lower compared to the results from Feng [1]. The reasons that bring about the discrepancy are the different distances between each rotor.

**Table 4.11 Predicted $C_p$s at different Tip-speed Ratios in 2-D simulations: (a) one single rotor (b) parallel matrix systems**

**(a)**

| Tip-speed Ratio | Present Study | Huang's predictions [2] | Feng's predictions [1] |
|---|---|---|---|
| 0.4 | 0.163 | 0.184 | 0.168 |
| 0.5 | 0.176 | 0.189 | 0.187 |
| 0.6 | 0.184 | 0.208 | 0.2 |
| 0.7 | 0.19 | 0.222 | 0.218 |
| 0.8 | 0.191 | 0.235 | 0.231 |
| 0.9 | 0.184 | 0.246 | 0.234 |
| 1.0 | 0.178 | 0.253 | 0.231 |
| 1.1 | 0.166 | 0.255 | 0.226 |
| 1.2 | 0.148 | 0.253 | 0.219 |

**(b)**

| Tip-speed Ratio | Present Study | Huang's predictions [2] | Feng's predictions [1] |
|---|---|---|---|
| 0.4 | 0.275 | 0.247 | 0.273 |
| 0.5 | 0.335 | 0.285 | 0.332 |
| 0.6 | 0.372 | 0.315 | 0.377 |
| 0.7 | 0.387 | 0.341 | 0.413 |
| 0.8 | 0.398 | 0.36 | 0.454 |
| 0.9 | 0.402 | 0.366 | 0.479 |
| 1.0 | 0.394 | 0.363 | 0.468 |
| 1.1 | 0.372 | 0.356 | 0.437 |
| 1.2 | 0.337 | 0.344 | 0.395 |

This research also includes one single Savonius wind rotor, the parallel matrix system with four Savonius wind rotors and the parallel matrix system with ten Savonius wind rotors. **Fig. 4.27** shows that the $C_p$s of one single Savonius wind rotor, the parallel matrix system with four Savonius wind rotors and the parallel matrix system with ten Savonius wind rotors. These systems are in the wind speeds of 7m/s and the tip speed ratios ranged from 0.4 to 1.2. The average $C_p$ of the parallel matrix system with ten Savonius wind rotors is 2.25 times higher than that in one single Savonius wind rotor and the average $C_p$ of the parallel matrix system with four Savonius wind rotors is 2.07 times higher than that in one single Savonius wind rotor. However, the average $C_p$ of the parallel matrix system with ten Savonius wind rotors is 1.08 times higher than that in the parallel matrix system with four Savonius wind rotors. It also reveals that parallel matrix systems apparently have higher performance than one single

rotor.

Furthermore, the power output can be derived from $C_p$ as follows:

$$C_p = \frac{W}{\frac{1}{2}\rho A v^3}$$

$$\Rightarrow W = C_p \cdot (\frac{1}{2}\rho A v^3)$$

By using the above equation, the maximums of average power output of Savonius wind rotor in the three conditions, the parallel matrix systems with phase angle difference 90° and one single Savonius wind rotor, are calculated and the results are listed in **Table 4.12**.

**Table 4.12 The maximum of average power output of the parallel matrix systems and one Single Savonius wind rotor**

| Condition | Wind Direction | Wind Speed (m/s) | Average Power Output (W/per rotor) |
|---|---|---|---|
| One Single Savonius wind rotor | - | 7 | 36.12 |
| | | 14 | 291.29 |
| The Parallel Matrix System with Four Savonius Wind Rotors | - | 7 | 76.08 |
| | | 14 | 609.44 |
| The Parallel | $\theta$ =0° | 7 | 24.87 |

| | | | |
|---|---|---|---|
| Matrix System with Ten Savonius Wind Rotors | | 14 | 252.18 |
| | $\theta$ =37° | 7 | 46.35 |
| | | 14 | 427.52 |
| | $\theta$ =53° | 7 | 57.3 |
| | | 14 | 520.24 |
| | $\theta$ =90° | 7 | 82.87 |
| | | 14 | 700.46 |

From the above table, it can be seen that the average power output of the parallel matrix systems are higher than the average power output of one single Savonius wind rotor. The reason is that the performance enhancement in the parallel matrix system depends on the positive interactions between wind rotors.

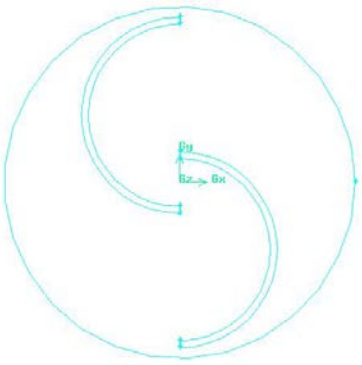

**(a)**

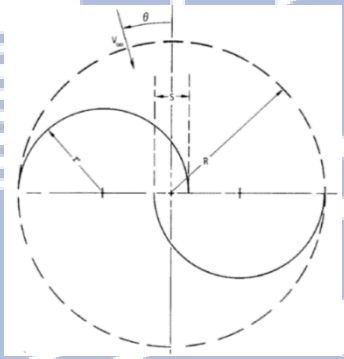

**(b)**

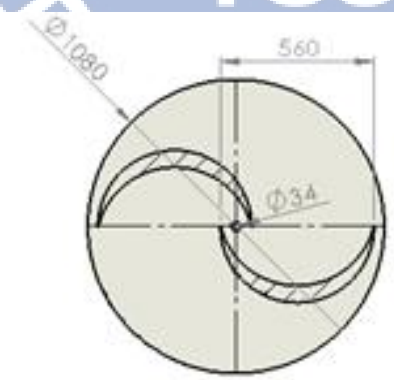


**(c)**

**Fig. 4.1 Schematics of Savonius wind rotor geometry: (a) present thesis; (b) Feng [1]; (c) Huang [2]**

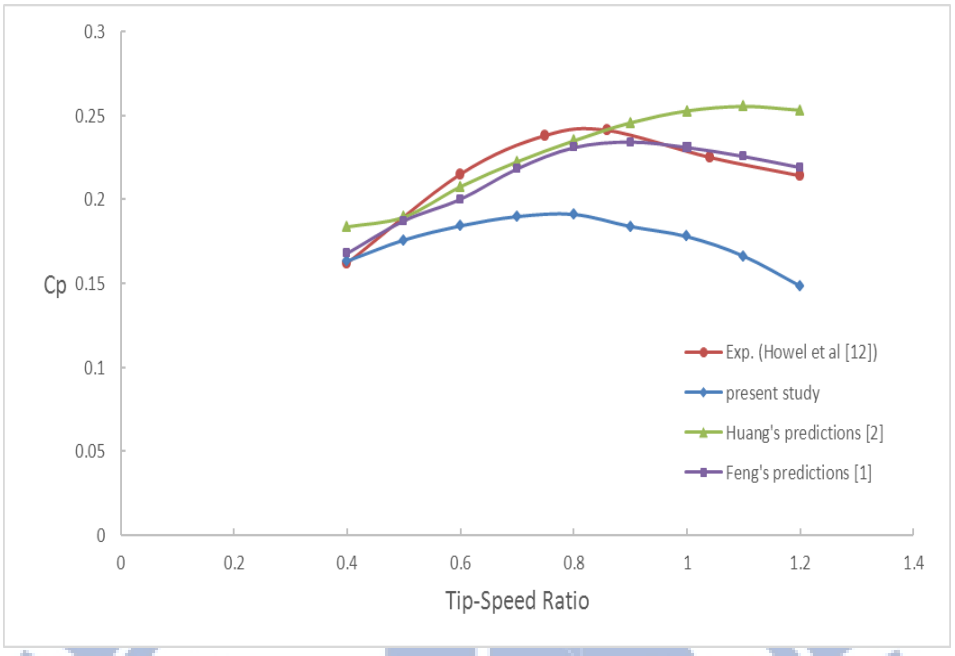


**(a)**

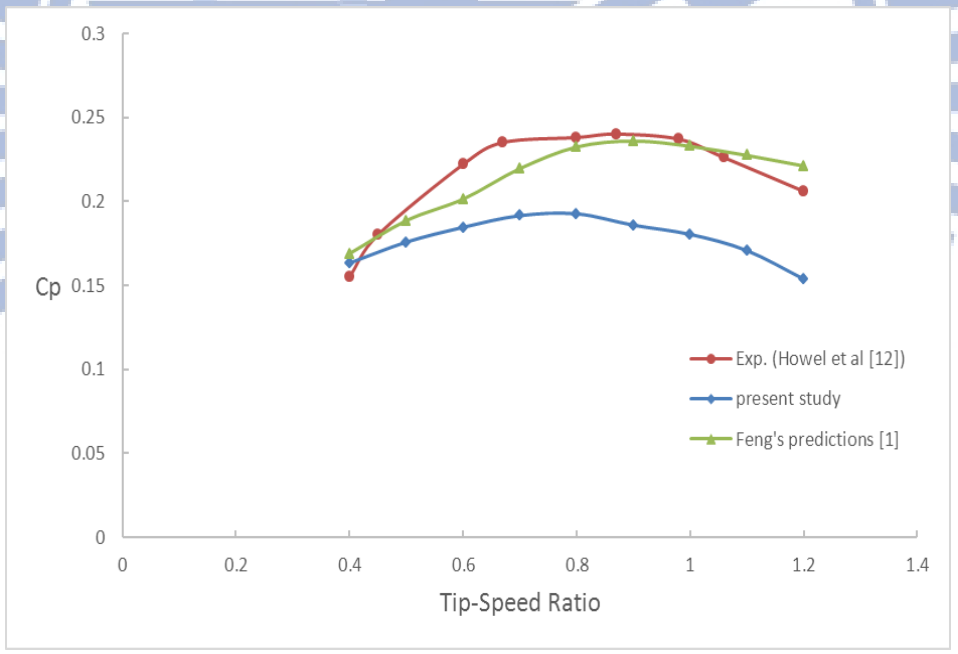


**(b)**

**Fig. 4.2 The 2D simulation of one single Savonius wind rotor comparing with Feng's predictions [1], Huang's predictions [2] and experimental measurements by Howell et al. [12] in: (a) wind speed 7 m/s; (b) wind speed 14 m/s**

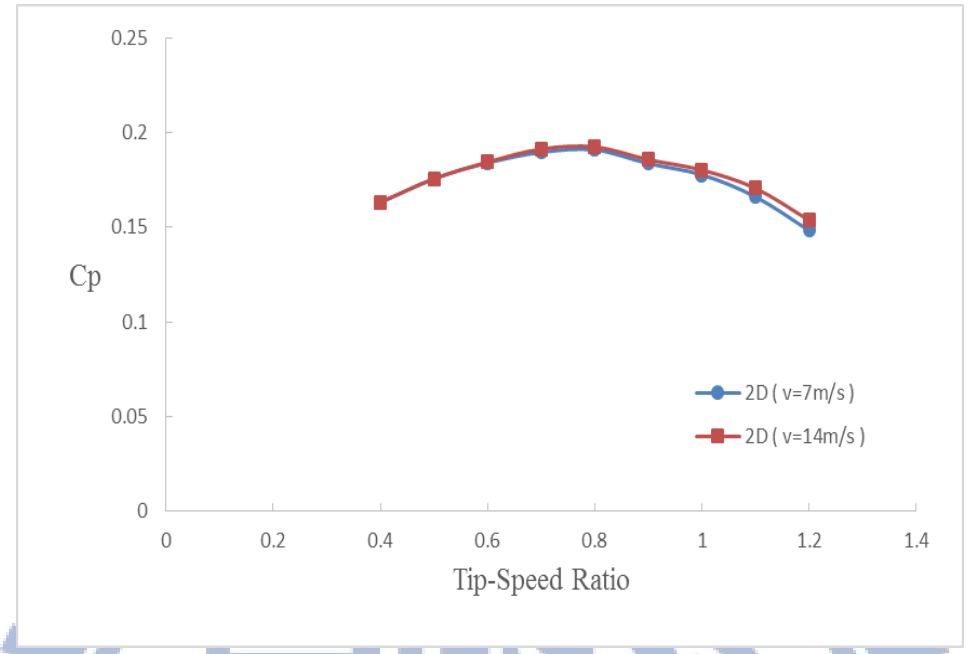


**Fig. 4.3 The performance of one single Savonius wind rotor**

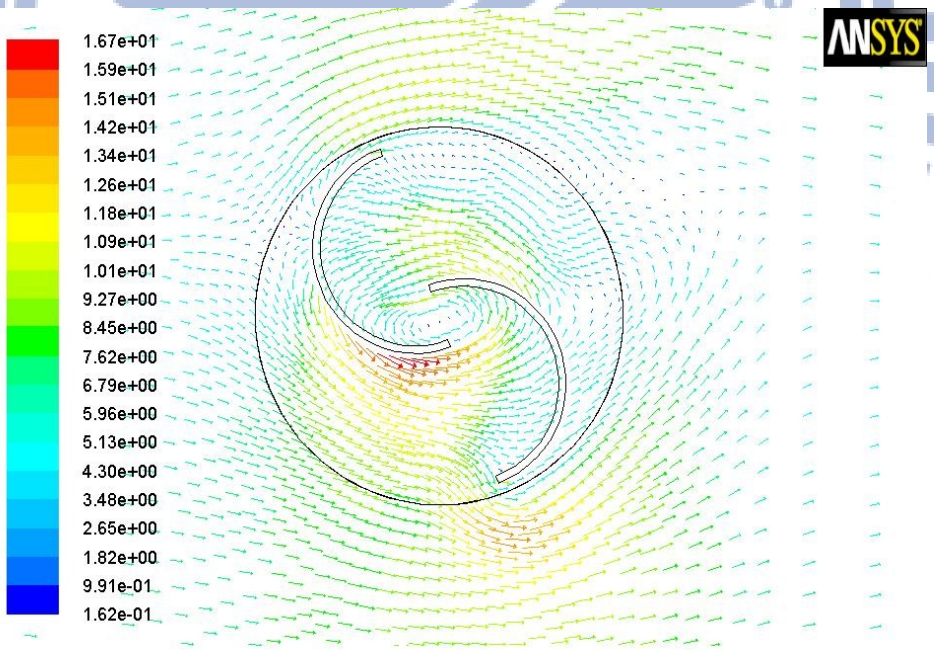


**(a)**

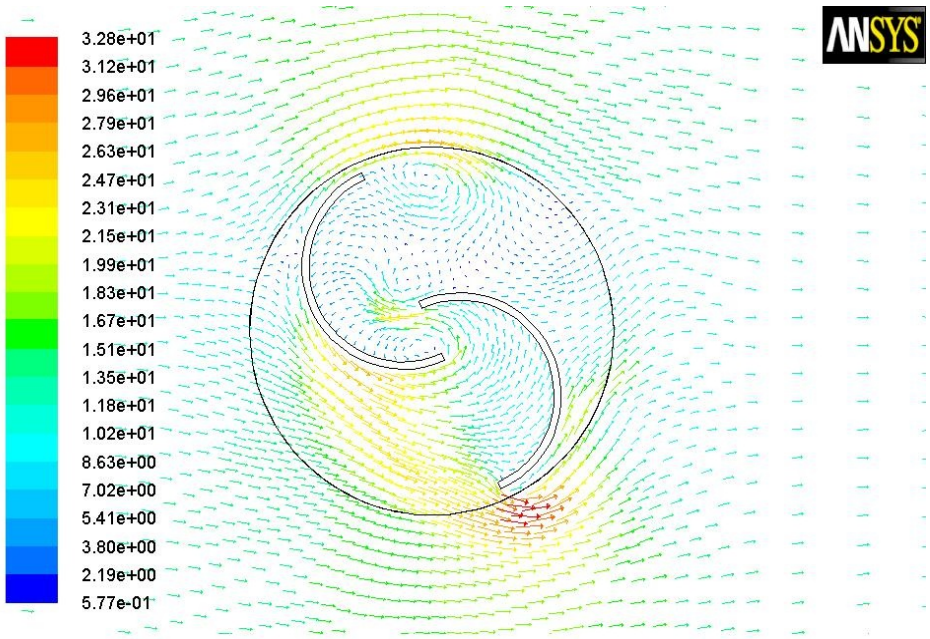


**(b)**

**Fig. 4.4 Velocity vector distribution around one single Savonius wind rotor at α=100° in wind speed: (a) 7m/s; (b) 14m/s**

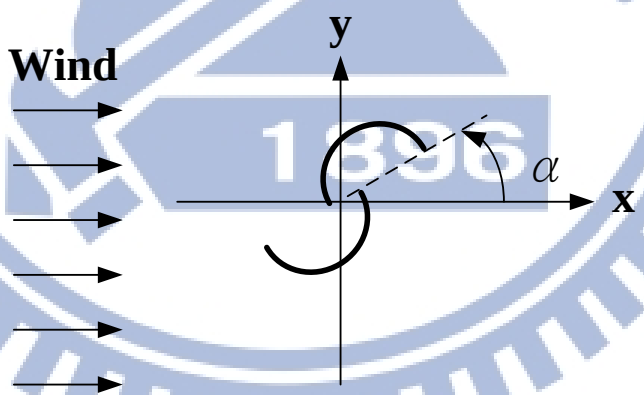


**Fig. 4.5 The defined angle α of rotating wind blade relative to the initial angle**

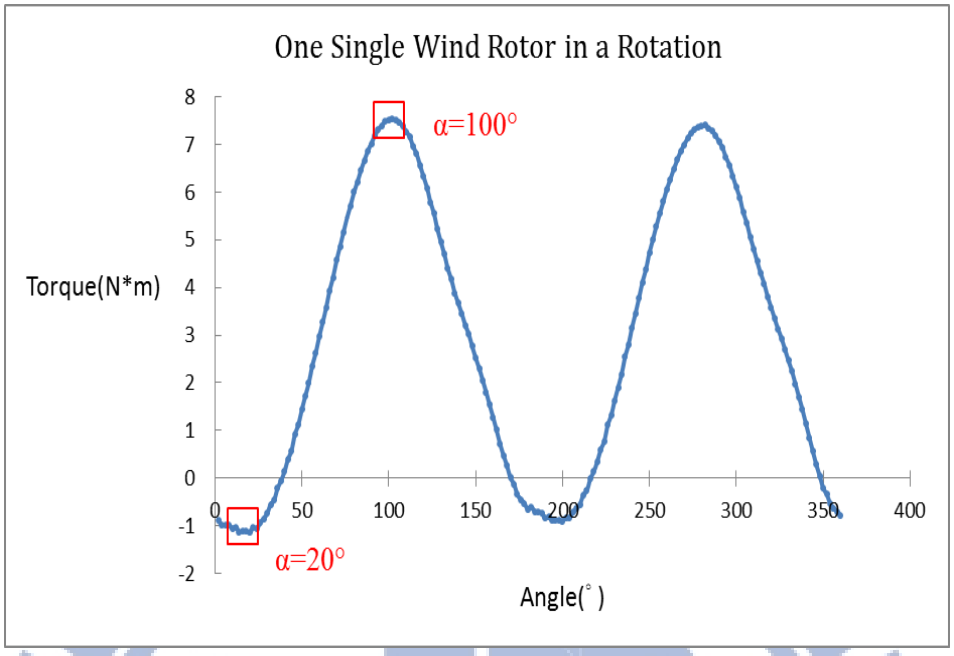


**Fig 4.6 Torque curve of one single Savonius wind rotor with wind speed 7 m/s and tip-speed ratio 0.8 in a rotation**

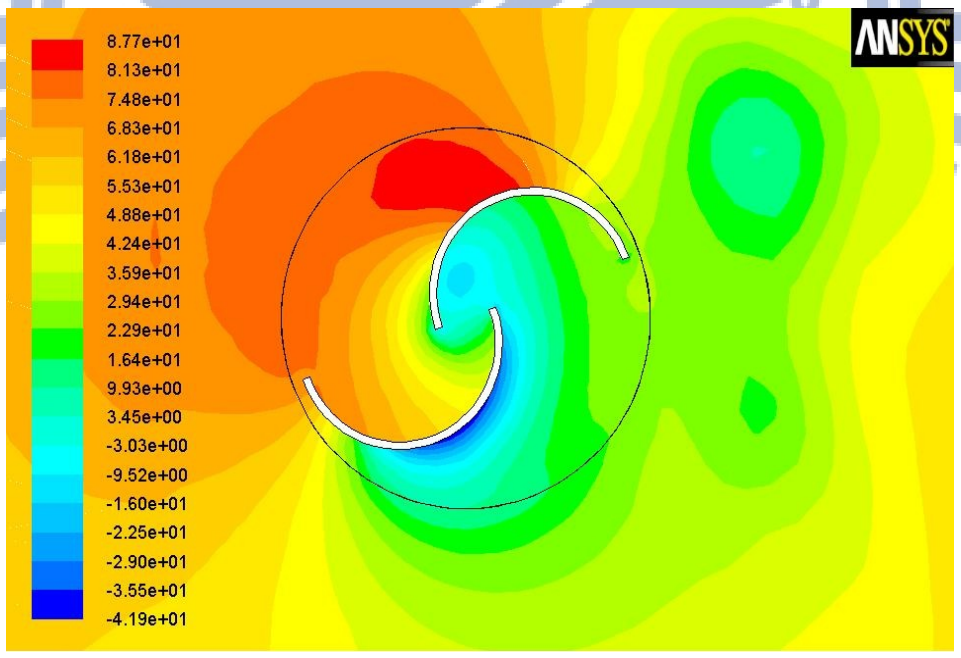


**(a)**

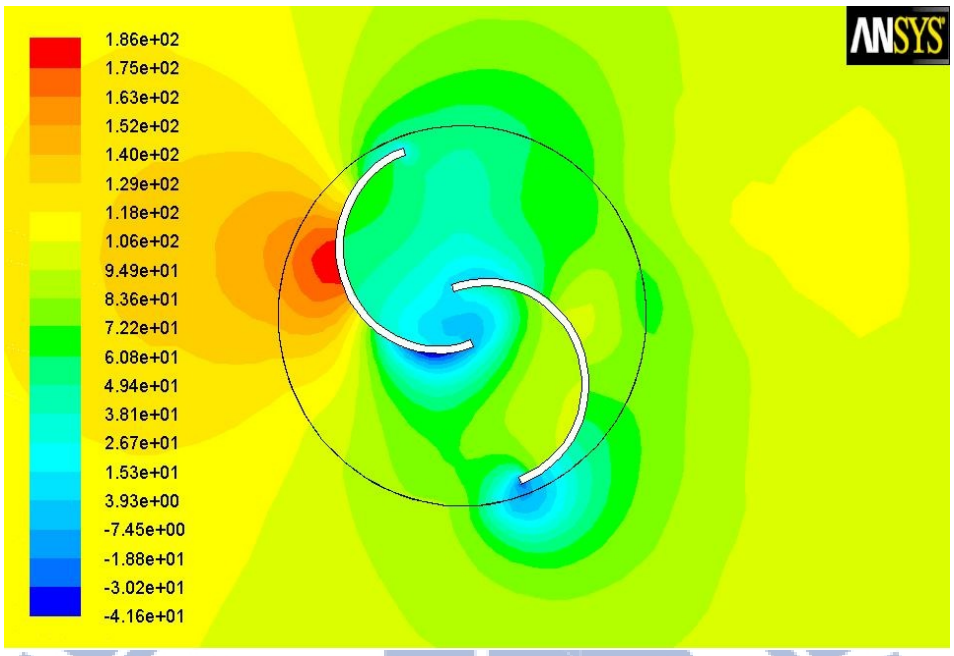


**(b)**

**Fig. 4.7 Static pressure field around one single Savonius wind rotor in 2-D simulation at: (a) α=20°; (b) α=100°**

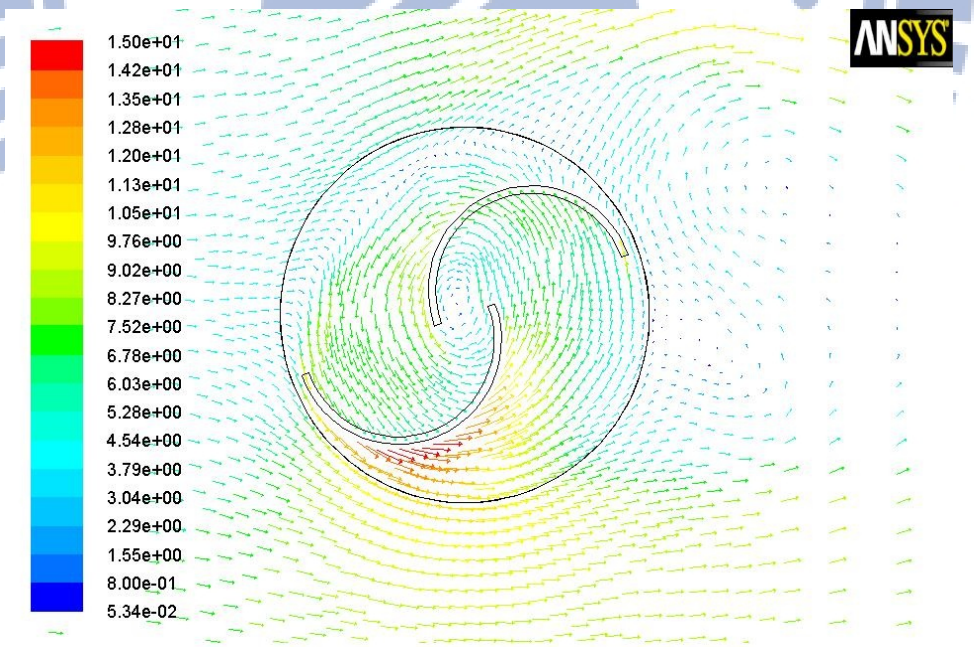


**(a)**

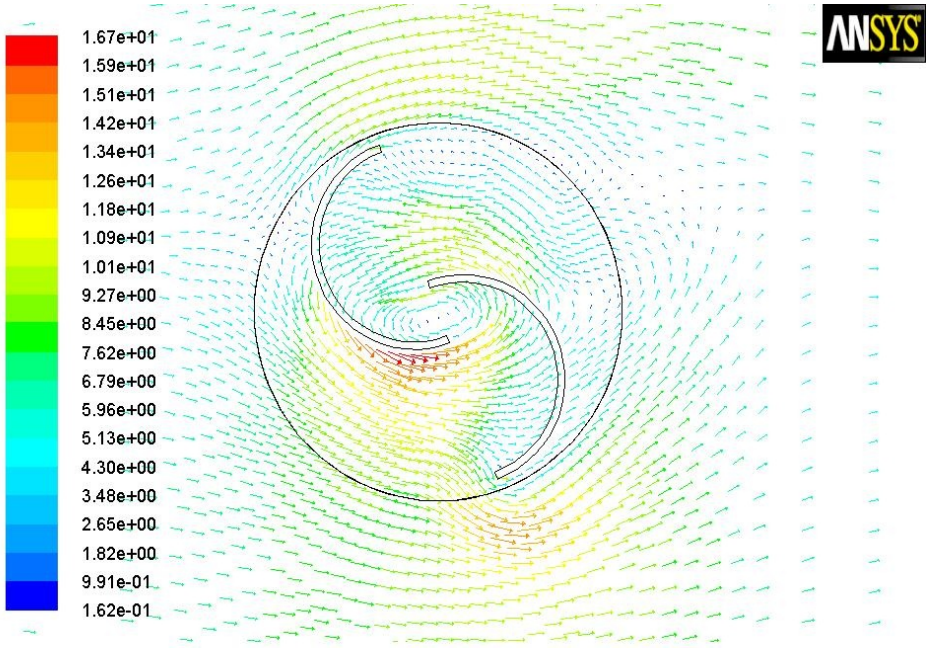


**(b)**

**Fig. 4.8 Velocity vector distribution around one single Savonius wind rotor in 2-D simulation at: (a) α=20°; (b) α=100°**

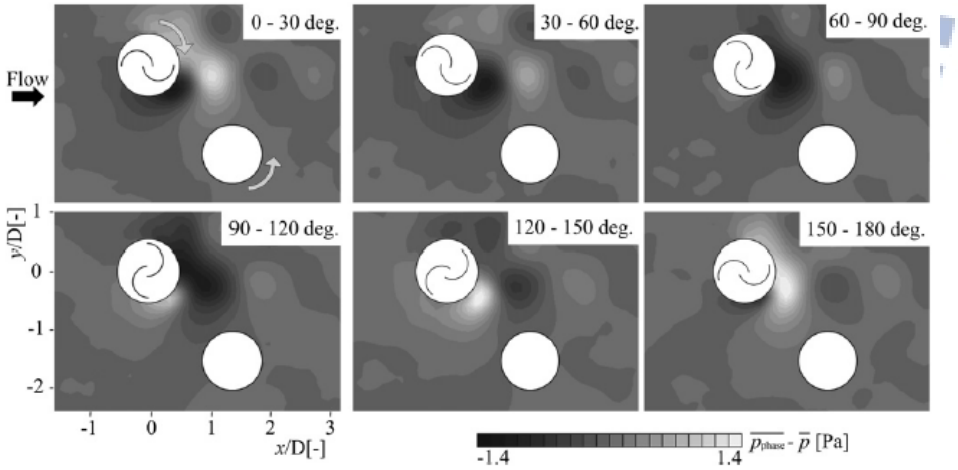


**Fig. 4.9 Phase-averaged pressure difference from the average pressure field [14]**

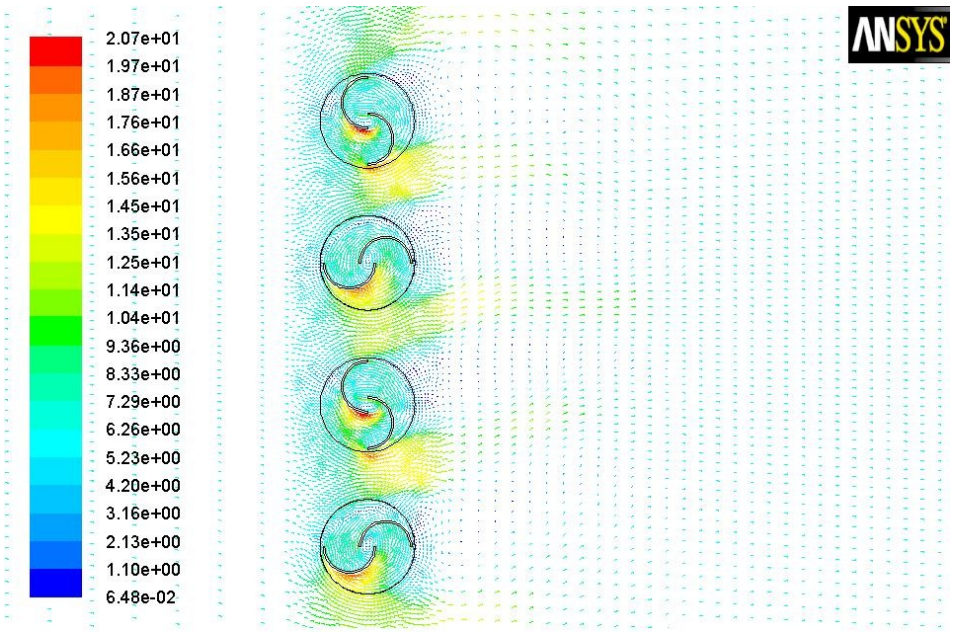


**(a)**

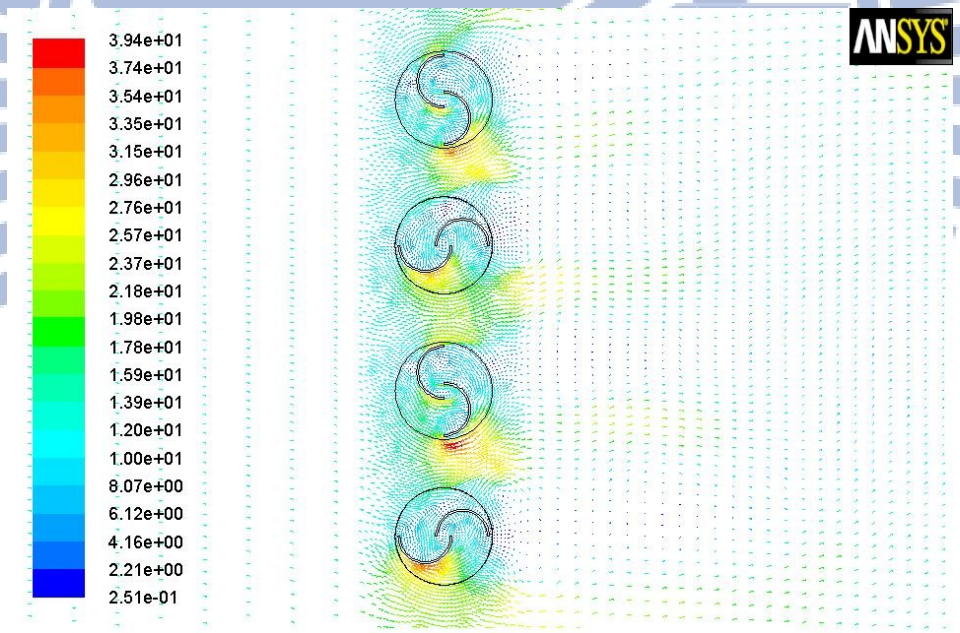


**(b)**

**Fig. 4.10 Velocity vector distribution around the parallel matrix system with four Savonius wind rotors in wind speed: (a) 7m/s; (b) 14m/s**

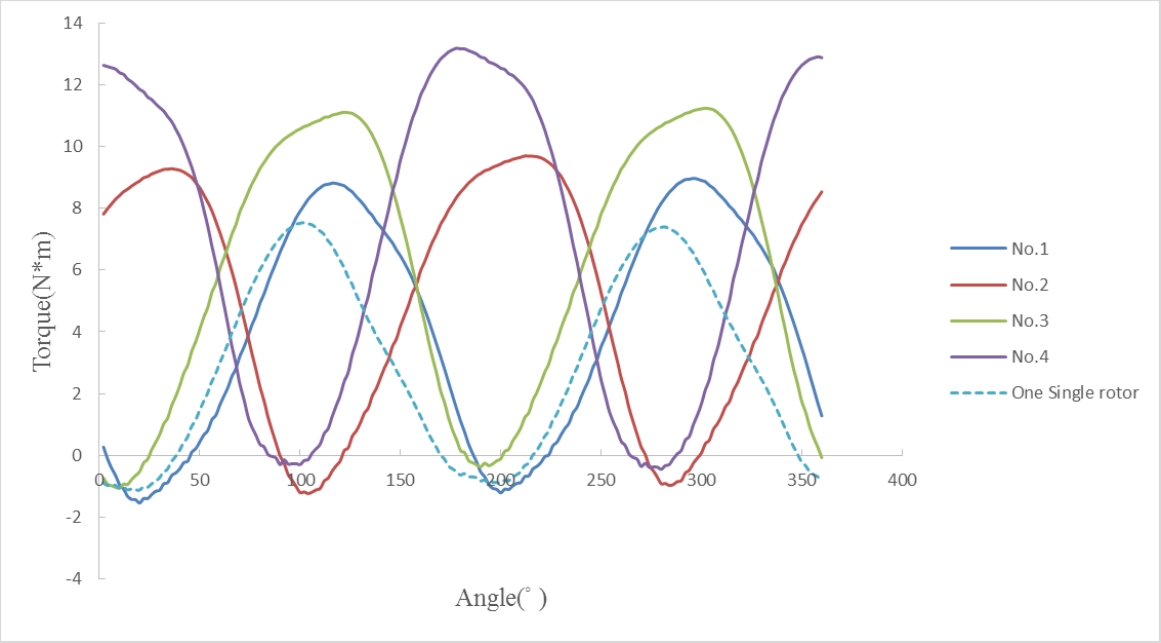


**Fig. 4.11 Torque curves of the parallel matrix system with four Savonius wind rotors and one single Savonius wind rotor**

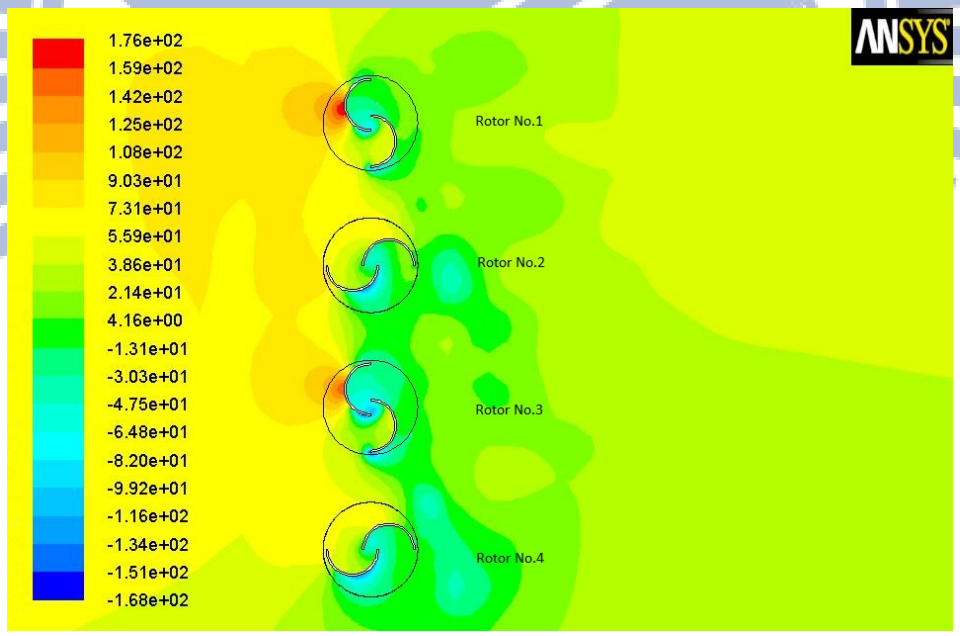


**Fig. 4.12 Static pressure field around the parallel matrix system with four Savonius wind rotors**

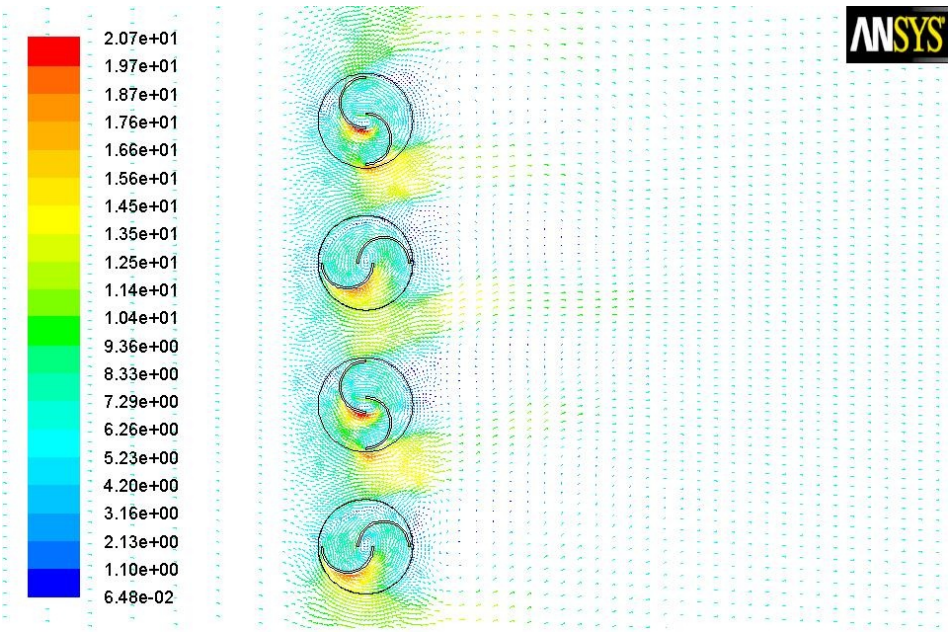


**Fig. 4.13 Velocity vector distribution around the parallel matrix system with four Savonius wind rotors**

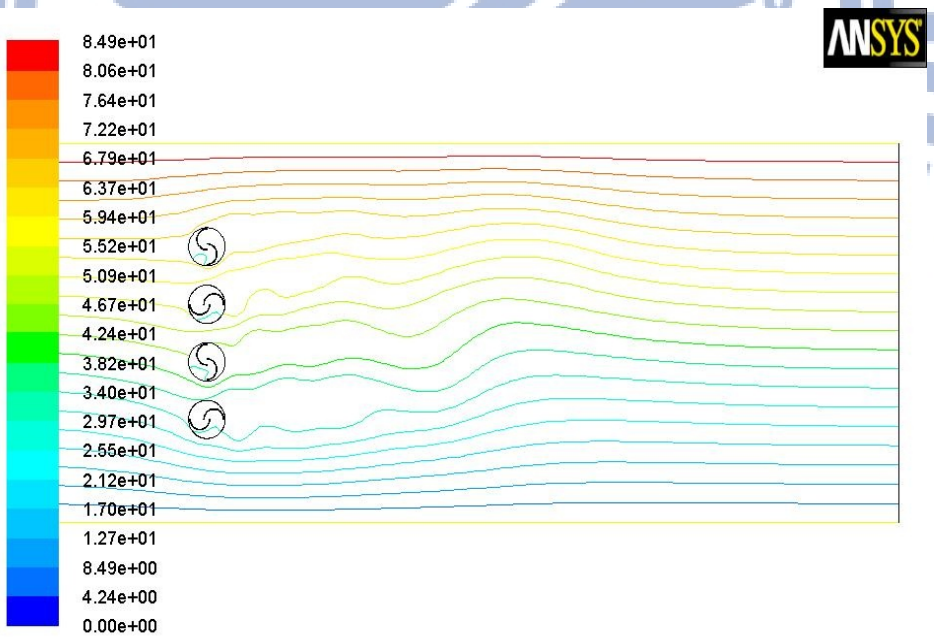


**Fig. 4.14 Streamlines around the parallel matrix system with four Savonius wind rotors at wind speed 7 m/s and TSR 0.9**

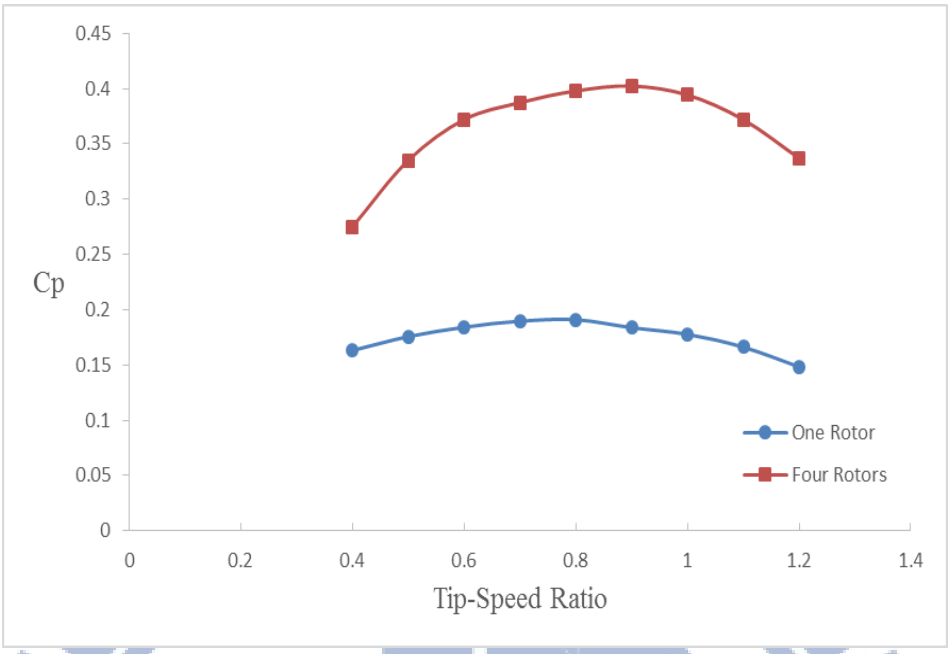


**Fig. 4.15 Comparison of the parallel matrix system with four Savonius wind rotors and one single Savonius wind rotor**

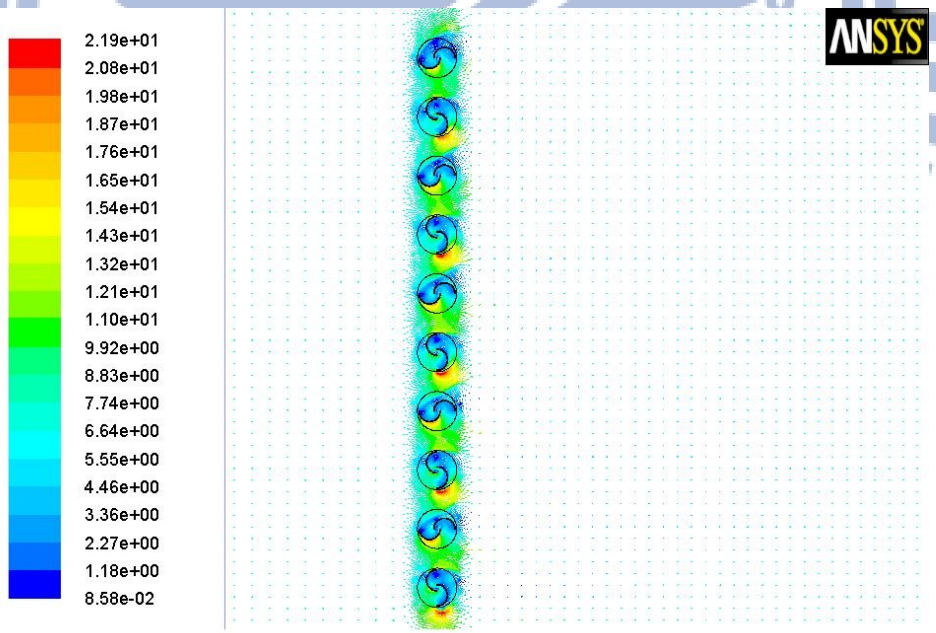


**(a)**

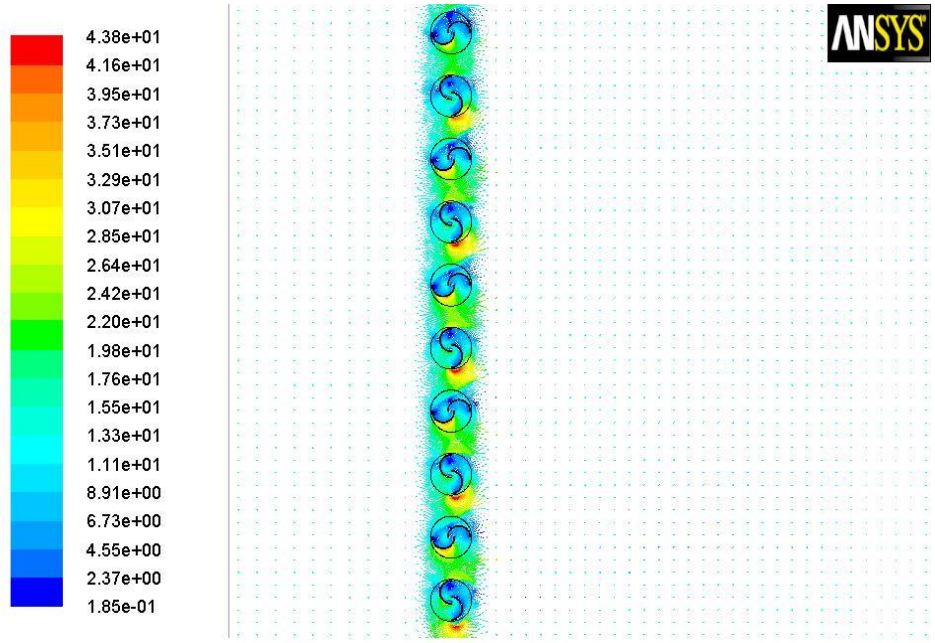


**(b)**

**Fig. 4.16 Velocity vector distribution around the parallel matrix system with ten Savonius wind rotors in wind speed: (a) 7m/s; (b) 14m/s**

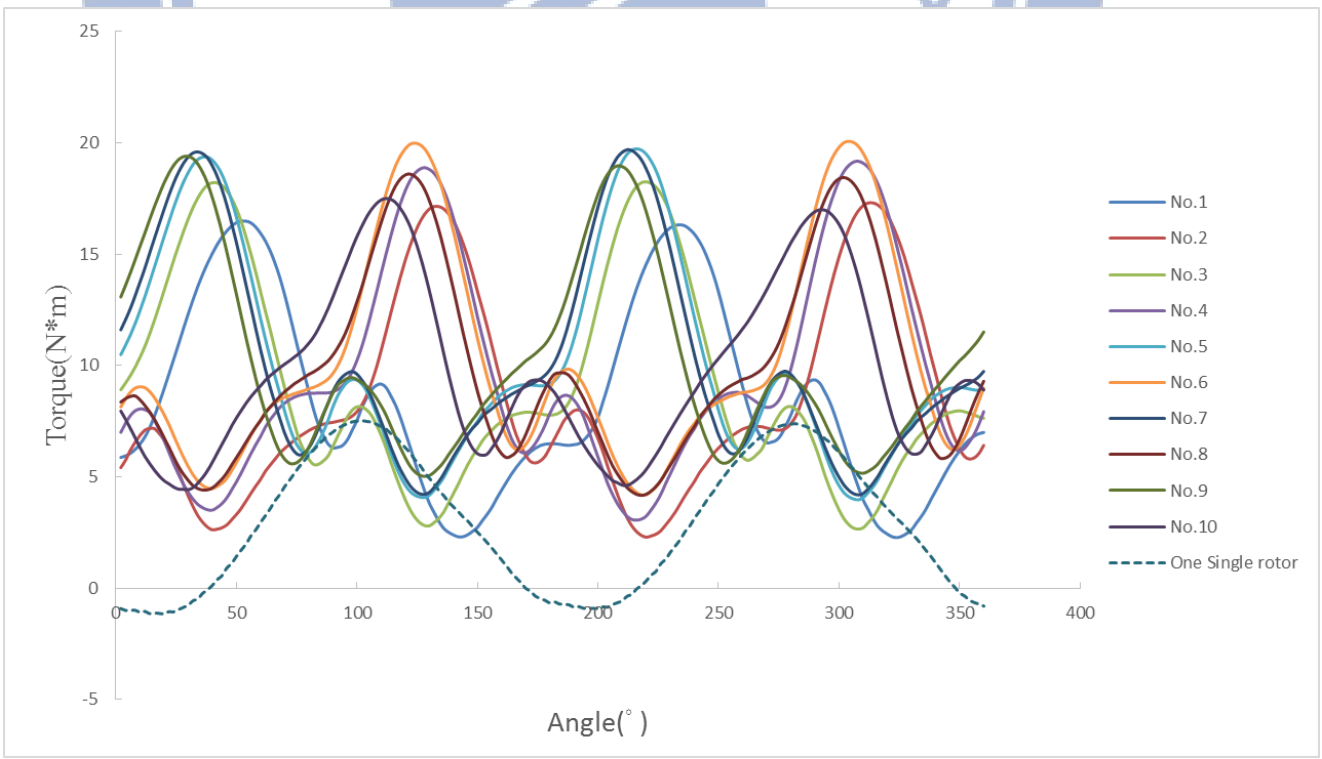


**Fig. 4.17 Torque curves of the parallel matrix system with ten Savonius wind rotors and one single Savonius wind rotor**

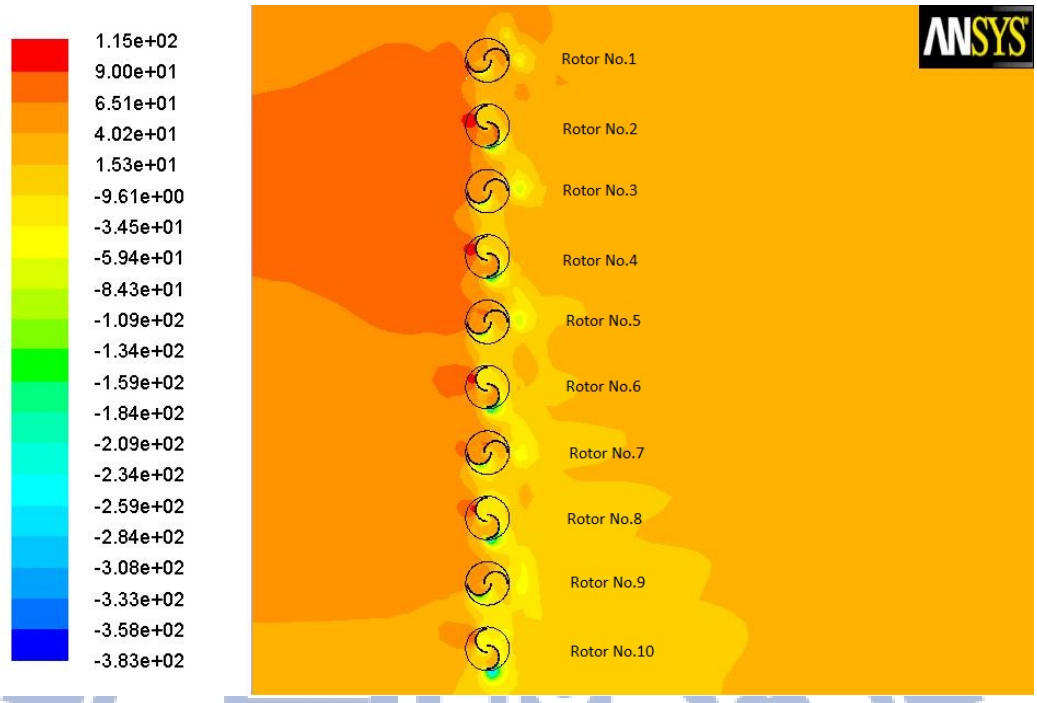


**Fig. 4.18 Static pressure field around the parallel matrix system with ten Savonius wind rotors**

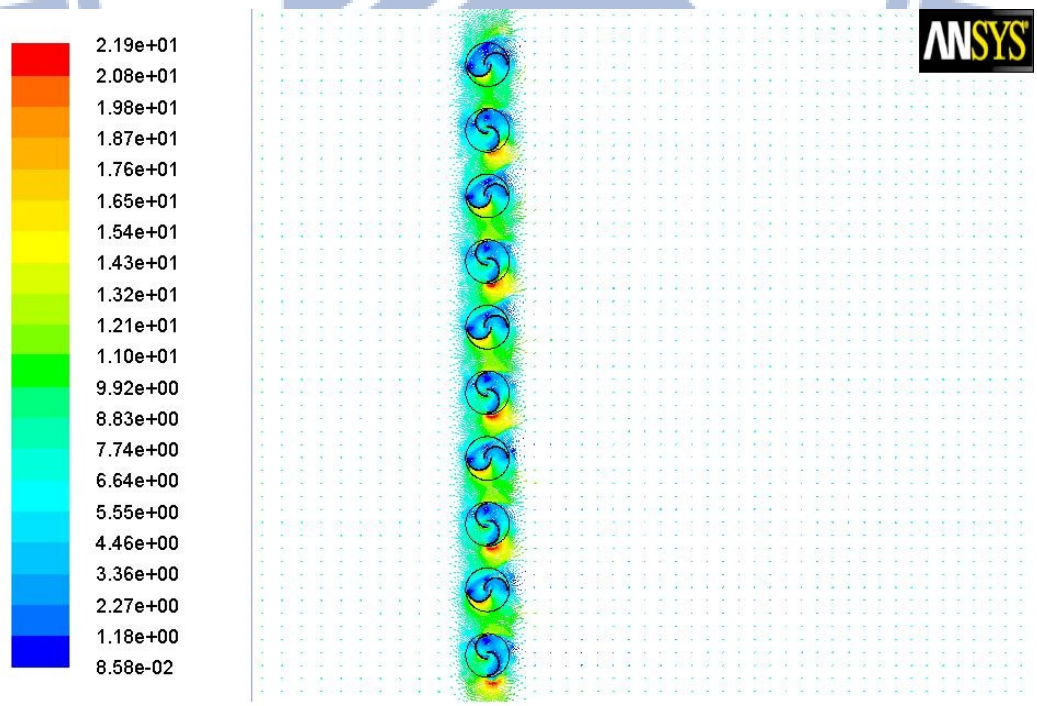


**Fig. 4.19 Velocity vector distribution around the parallel matrix system with ten Savonius wind rotors**

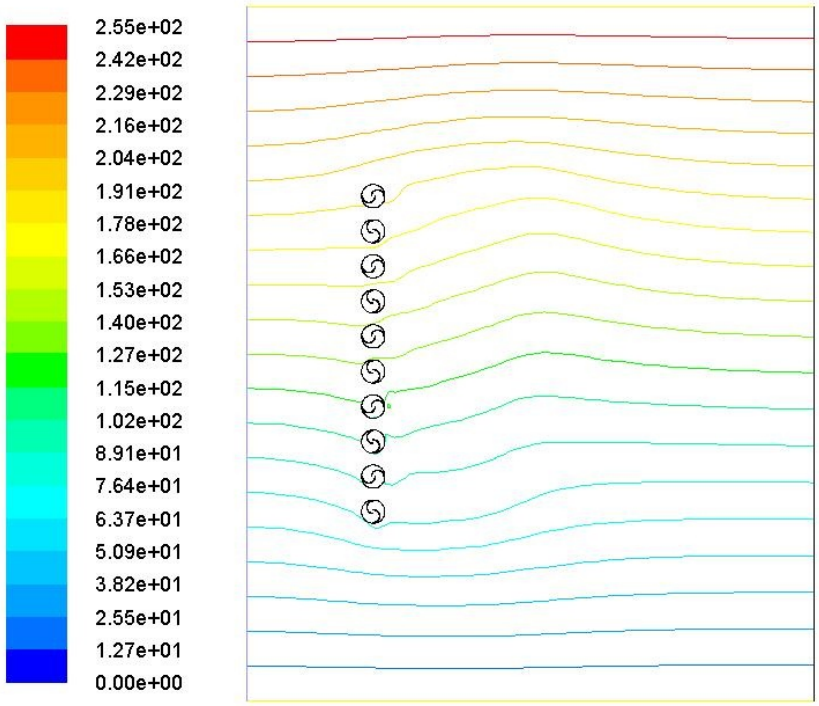


**Fig. 4.20 Streamlines around the parallel matrix system with ten Savonius wind rotors at wind speed 7 m/s and TSR 0.7**

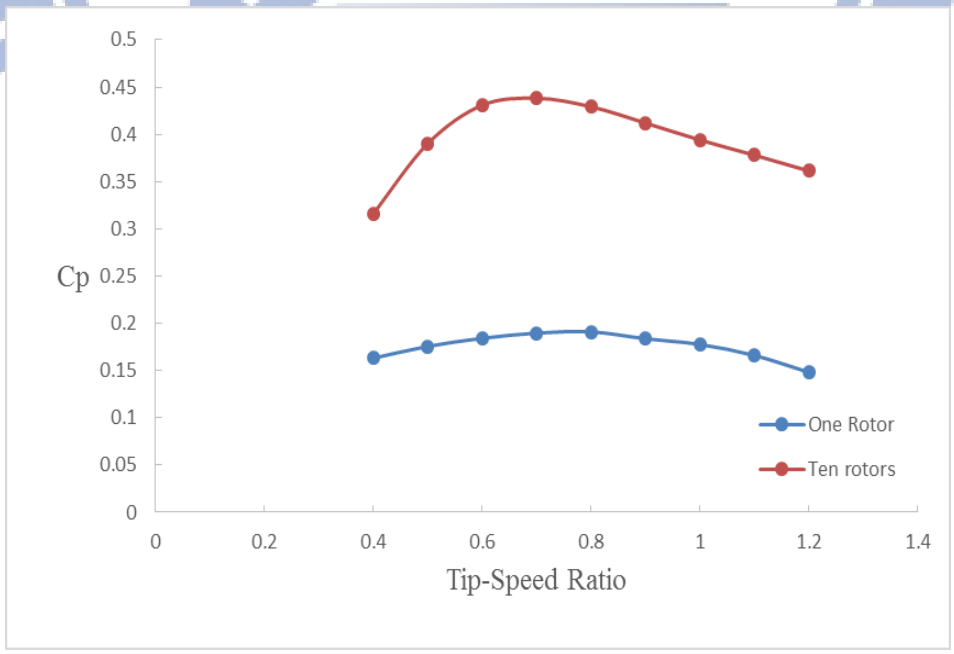


**Fig. 4.21 Comparison of the parallel matrix system with ten Savonius wind rotors and one single Savonius wind rotor**

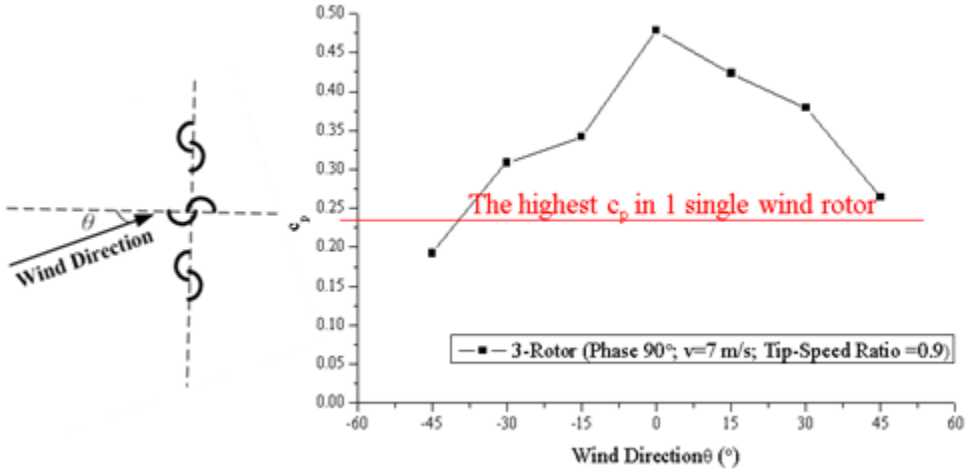


**Fig. 4.22 Three-rotor with phase angle difference 90° in different wind directions [1]**

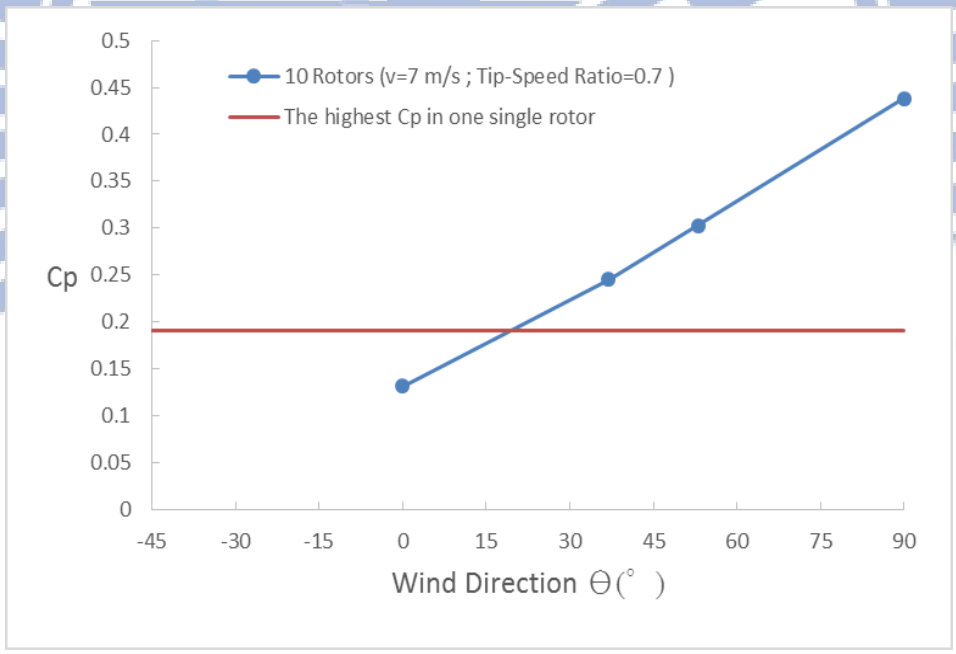


**Fig. 4.23 the parallel matrix system with ten Savonius wind rotors in different wind directions**

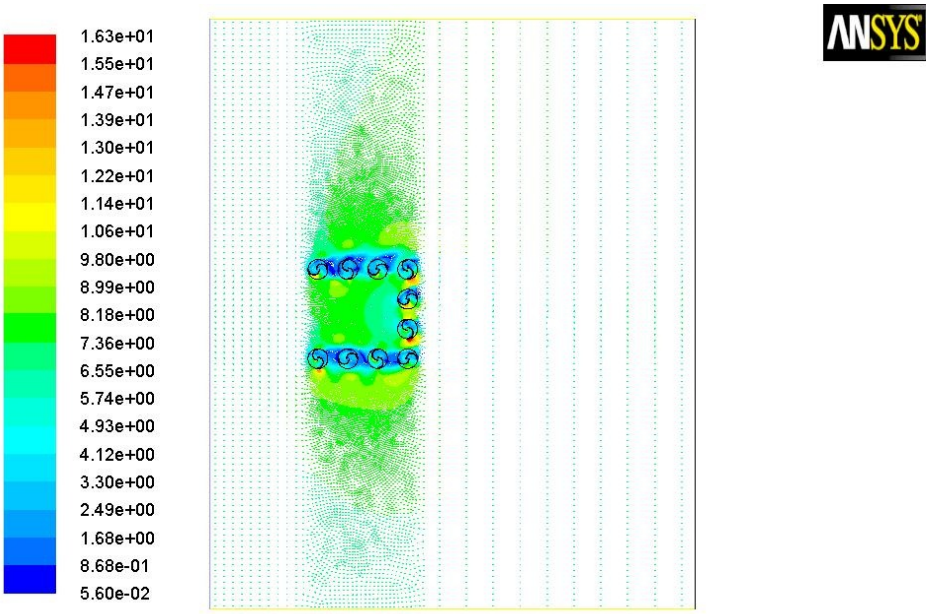
1.63e+01
1.55e+01
1.47e+01
1.39e+01
1.30e+01
1.22e+01
1.14e+01
1.06e+01
9.80e+00
8.99e+00
8.18e+00
7.36e+00
6.55e+00
5.74e+00
4.93e+00
4.12e+00
3.30e+00
2.49e+00
1.68e+00
8.68e-01
5.60e-02
ANSYS

**(a)**

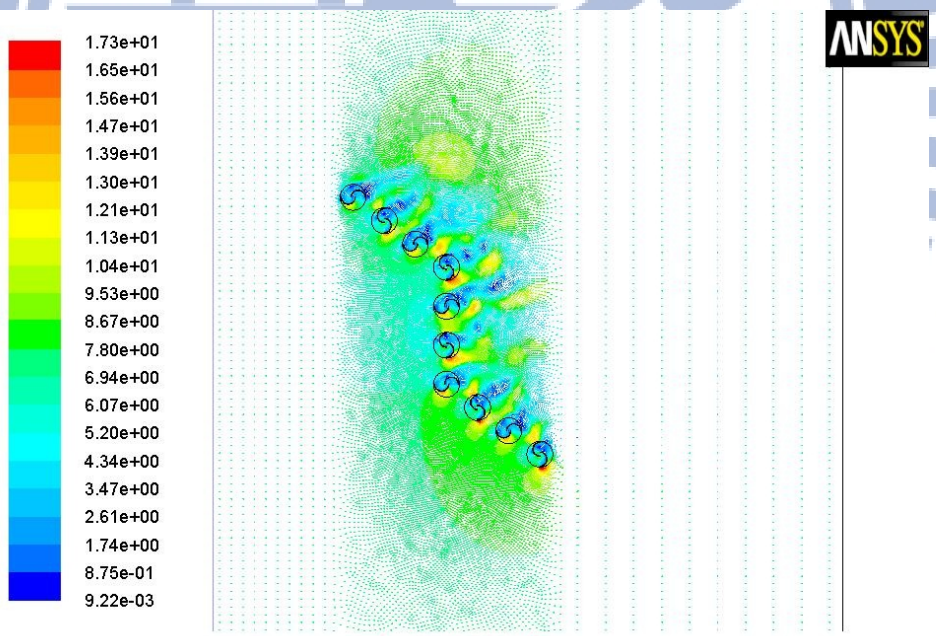
1.73e+01
1.65e+01
1.56e+01
1.47e+01
1.39e+01
1.30e+01
1.21e+01
1.13e+01
1.04e+01
9.53e+00
8.67e+00
7.80e+00
6.94e+00
6.07e+00
5.20e+00
4.34e+00
3.47e+00
2.61e+00
1.74e+00
8.75e-01
9.22e-03
ANSYS

**(b)**

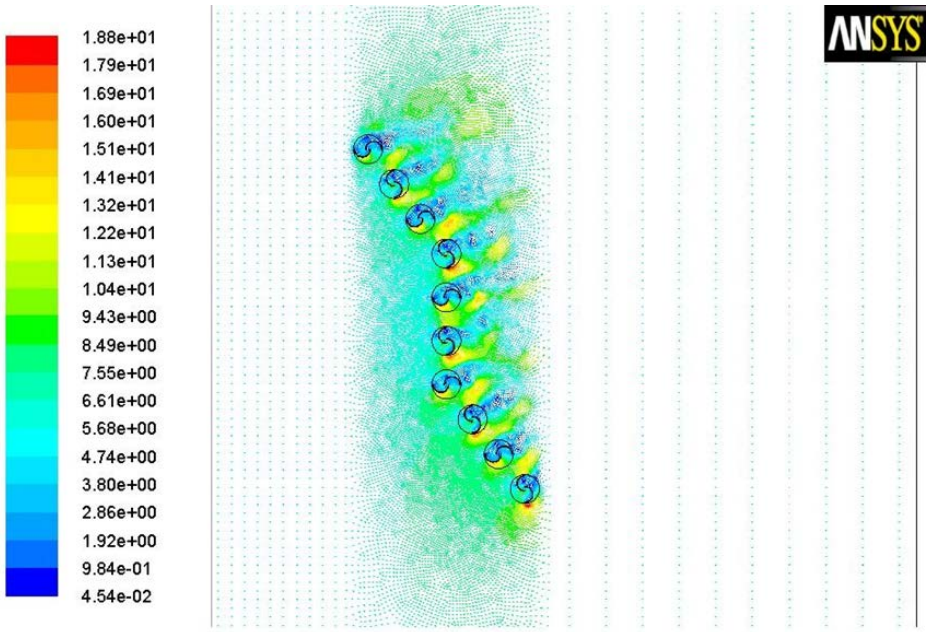


**(c)**

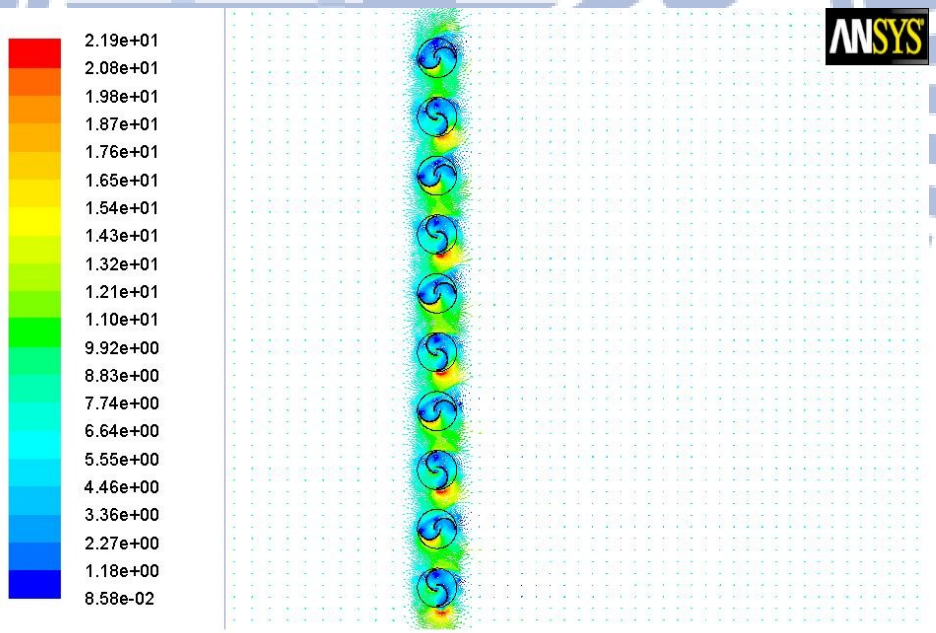


**(d)**

**Fig. 4.24 Velocity vector distribution around the ten Savonius wind rotors with a change of wind direction θ (a) θ = 0°; (b) θ = 37°; (c) θ = 53°; (d) θ = 90°**

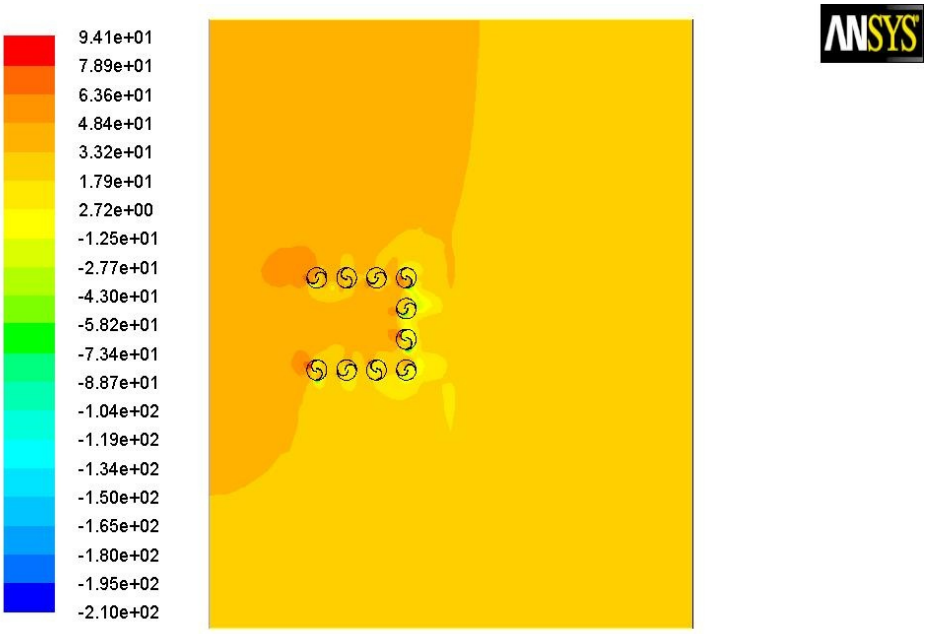
9.41e+01
7.89e+01
6.36e+01
4.84e+01
3.32e+01
1.79e+01
2.72e+00
-1.25e+01
-2.77e+01
-4.30e+01
-5.82e+01
-7.34e+01
-8.87e+01
-1.04e+02
-1.19e+02
-1.34e+02
-1.50e+02
-1.65e+02
-1.80e+02
-1.95e+02
-2.10e+02
ANSYS

**(a)**

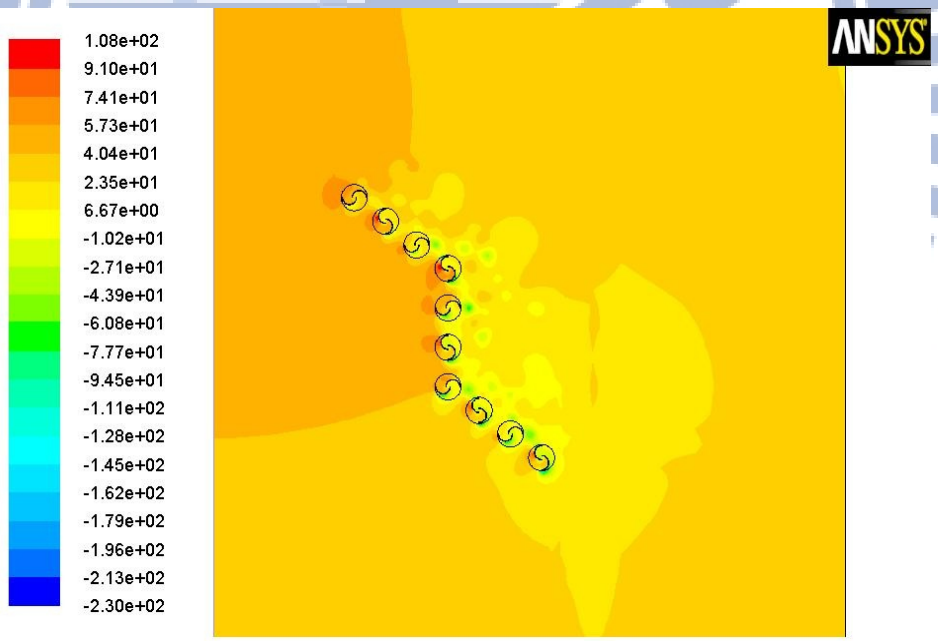
1.08e+02
9.10e+01
7.41e+01
5.73e+01
4.04e+01
2.35e+01
6.67e+00
-1.02e+01
-2.71e+01
-4.39e+01
-6.08e+01
-7.77e+01
-9.45e+01
-1.11e+02
-1.28e+02
-1.45e+02
-1.62e+02
-1.79e+02
-1.96e+02
-2.13e+02
-2.30e+02
ANSYS

**(b)**

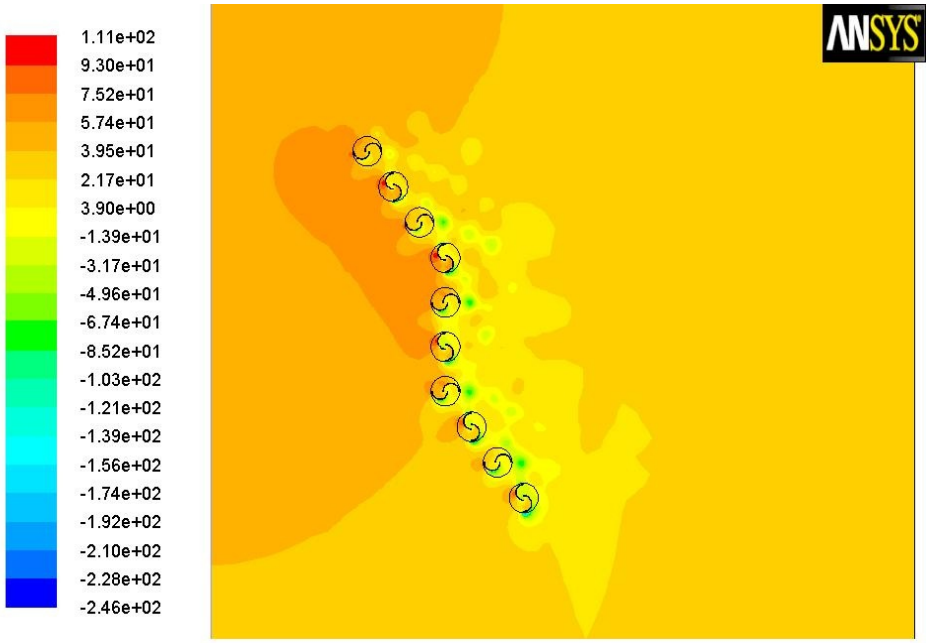


**(c)**

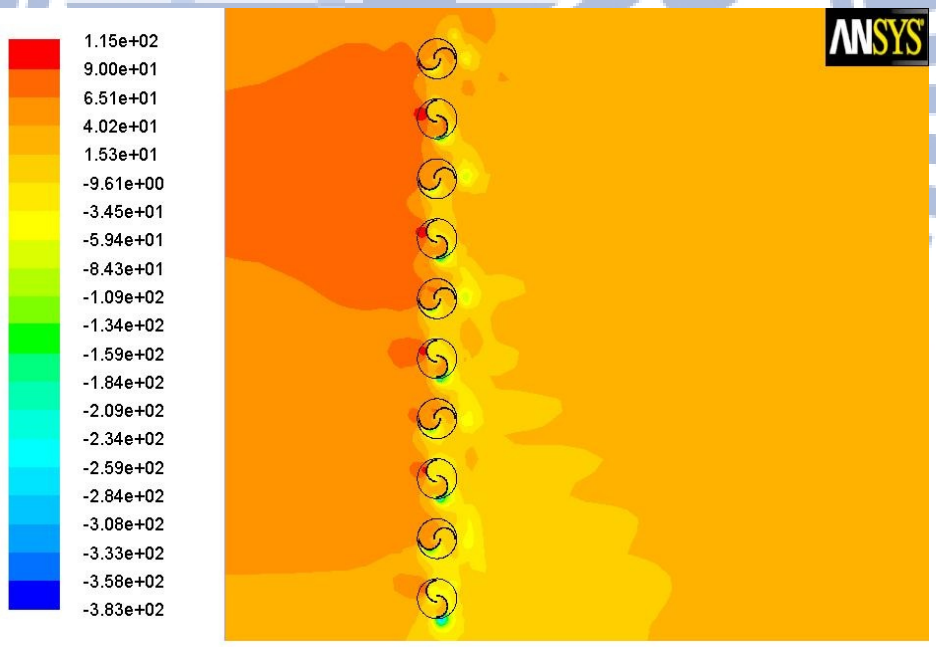


**(d)**

**Fig. 4.25 Static pressure field around the ten Savonius wind rotors with a change of wind direction θ (a) θ = 0°; (b) θ = 37°; (c) θ = 53°; (d) θ = 90°**

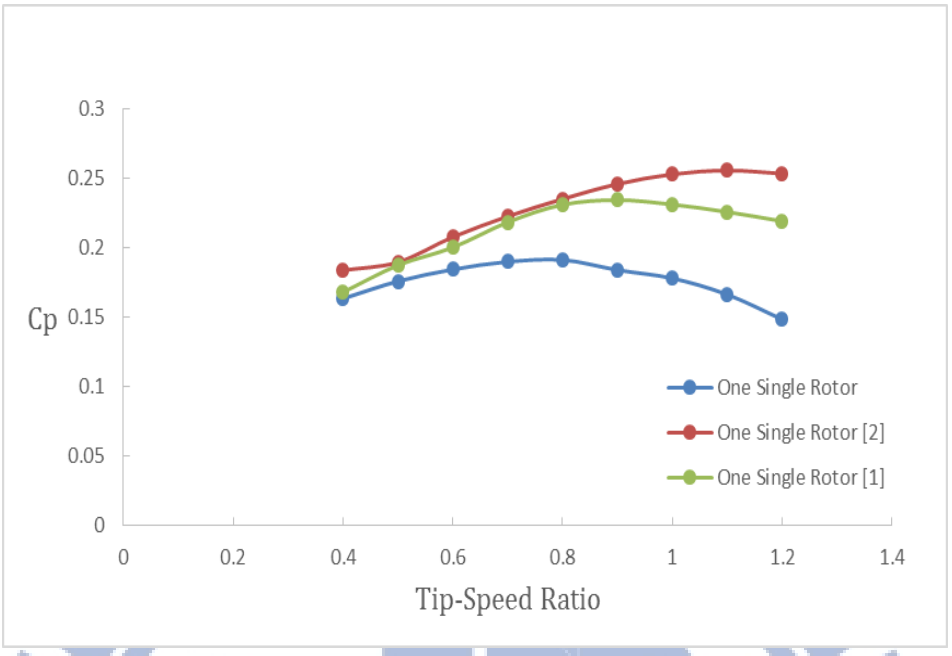


**(a)**

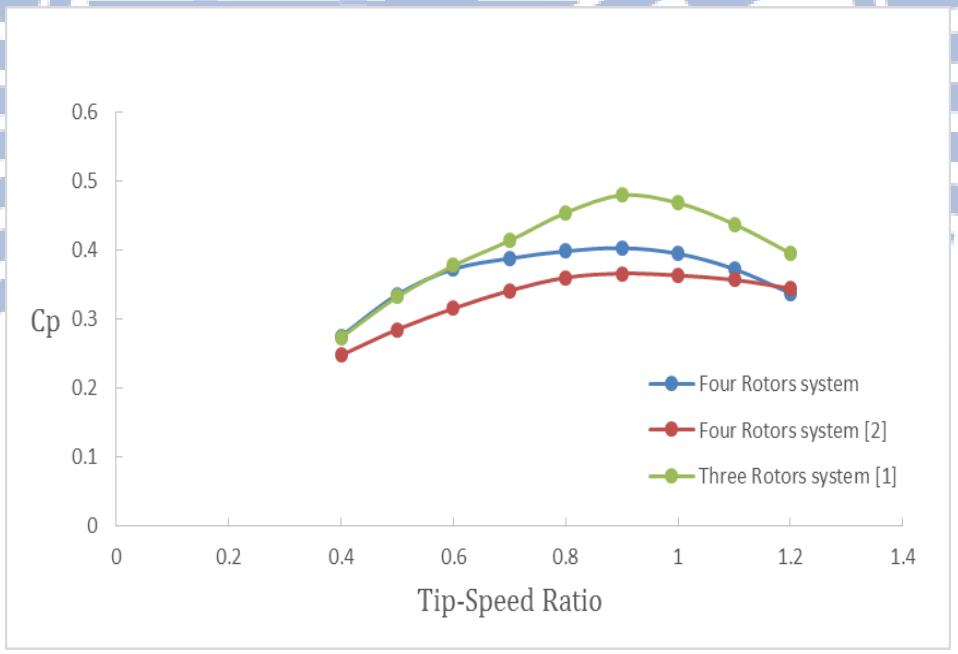


**(b)**

**Fig. 4.26 Predicted $C_p$s at different Tip-speed Ratios in 2-D simulations: (a) one single rotor; (b) parallel matrix system**

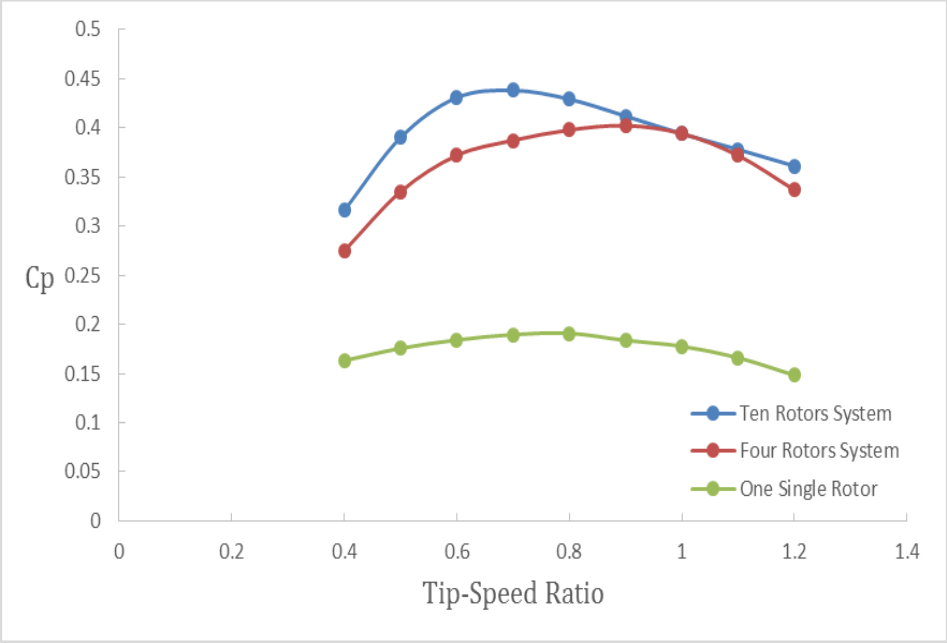


**Fig. 4.27 Comparison of the parallel matrix system with ten Savonius wind rotors, the parallel matrix system with four Savonius wind rotors and one single Savonius wind rotor**

# CHAPTER 5

# CONCLUSIONS AND RECOMMENDATIONS

## 5.1 Conclusions

This study employs a computational fluid dynamics (CFD) software, Fluent, to analyze the flow fields around two-bladed Savonius wind rotors and their corresponding performances. This research includes three cases: the first one is a single Savonius wind rotor, the second is a parallel matrix system, consisting of four two-bladed Savonius wind rotors, and the last one is a parallel matrix system of ten two-bladed Savonius wind rotors. All of the cases begin with the analyses of the effect of wind velocity and tip speed ratio on $C_p$, and the influence of wind direction change on the $C_p$ is studied subsequently. Eventually, comparisons between different cases mentioned above are discussed for further investigation.

According to the simulation results, the conclusions are organized as follows:

Firstly, in the case of one single Savonius wind rotor, the minimal torque happens at $\alpha = 20°$ and the maximal one happens at $\alpha = 100°$. The pressure difference between the front and back side of the returning blade at $\alpha = 20°$ is apparently higher than that at $\alpha = 100°$. In addition, at $\alpha = 20°$, it can be seen that a large vortex is generated around the tip at the low-pressure region behind the blade. This phenomenon would result in a negative torque and further causes a low net torque. On the other hand, at $\alpha = 100°$, smaller vortices are obtained, and the pressure difference across the returning blade is smaller compared to the one at $\alpha = 20°$. Therefore, the negative torque is reduced, resulting in a higher net torque. Such phenomena are typical characteristics of drag devices, which

have high starting torque but low $C_p$.

Secondly, in the case of the parallel matrix system with four Savonius wind rotors and the parallel matrix system with ten Savonius wind rotors. The difference between each adjacent stream functions represents the volume flow rate. Therefore, the two adjacent streamlines with narrow gap indicates higher velocity and streamlines with wide gap shows low velocity. The high velocity indicates that wind passes through the wind rotor easily. On the other hand, the low velocity indicates that the wind rotor is able to absorb more wind energy and lead to velocity decrease. Thus, wind rotors produce an asymmetrical flow field that the dense streamlines take place around wind rotor with lower torque; wider streamlines around wind rotor with higher torque.

Thirdly, among the three cases in this study, the $C_p$s in wind speed 14 m/s conditions are slightly higher than those in 7 m/s at the same tip-speed ratio. It is because the Reynolds number around the blades increases with wind speed, causing a delayed separation. Therefore, the drags on the advancing blades decrease and then cause a higher $C_p$.

Fourthly, the 2-D predictions of these three systems are in the wind speeds of 7m/s and the tip speed ratios ranged from 0.4 to 1.2. The average $C_p$ of the parallel matrix system with ten Savonius wind rotors is 2.25 times higher than that in one single Savonius wind rotor and the average $C_p$ of the parallel matrix system with four Savonius wind rotors is 2.07 times higher than that in one single Savonius wind rotor. However, the average $C_p$ of the parallel matrix system with ten Savonius wind rotors is 1.08 times higher than that in the parallel matrix system with four Savonius wind rotors.

Finally, with ten Savonius wind rotors at the conditions of 90° phase angle difference, 7 m/s wind velocity, and 0.7 tip-speed ratio, the change of wind

direction will clearly affect the $C_p$, and the lowest $C_p$ is found in parallel matrix system with $\theta = 0°$. Moreover, while $\theta = 0°$, the $C_p$ with ten rotors is even lower than that of a single one. It indicates that the parallel matrix system is strongly influenced by the change of wind direction, representing that one of the advantages in VAWTs is lost.

## 5.2 Recommendations

In the end of this study, some recommendations for future extension of this research are listed as follows:

1. Investigate the influence of the blade thickness on power coefficient of parallel matrix system of Savonius wind rotors.
2. Investigate the influence of distance between wind rotors on power coefficient of parallel matrix system of Savonius wind rotors.
3. Conduct experiment with parallel matrix system of Savonius wind rotors and compare the experimental data with this simulation results.

# REFERENCE


[1] Jia-Shiuan Feng, “A Numerical Analysis of Power Efficiency of Wind Rotor System in Parallel Matrix”, National Chiao Tung University, Degree of Master of Science in Mechanical Engineering, June 2011.

[2] Tien-Yang Huang, “The Experimental Study of Power Efficiency of Two-bladed Wind Rotors in Parallel Matrix System”, National Chiao Tung University, Degree of Master of Science in Mechanical Engineering, June 2012.

[3] S. J. Savonius, “The S-Roto and its Applications”, Mechanical Engineering, 8. No.5, pp.333-338, 1931.

[4] Ben F. Blackwell, Robert E. Sheldahl, and Louis V. Feltz, “Wind Tunnel Performance Data for Two- and Three-bucket Savonius Rotors”, Journal of Energy, 2, pp.160-164, 1978.

[5] Nobuyuki Fujisawa, “On the Torque Mechanism of Savonius Rotors”, Journal of Wind Engineering and Industrial Aerodynamics, 40, pp. 277-292, 1992.

[6] R. Gupta, R. Das, and K. Sharma, “Experimental Study of a Savonius-Darrieus Wind Machine”, Proceedings of the International Conference on Renewable Energy for Developing Countries, Washington D. C., April 2006.

[7] Kunio Irabu and Jitendro Nath Roy, “Characteristics of Wind Power on Savonius Rotor Using a Guide-box Tunnel”, Experimental Thermal and Fluid Science, 32, pp. 580-586, 2007.

[8] U.K. Saha, S. Thotla, D. Maity, “Optimum Design Configuration of Savonius Rotor through Wind Tunnel Experiments”, Journal of Wind

Engineering and Industrial Aerodynamics, 96, pp. 1359-1375, 2008.

[9] Burçin Deda Altan, Mehmet Atılgan, and Aydoğan Özdamar, “An Experimental Study on Improvement of a Savonius Rotor Performance with Curtaining”, Experimental Thermal and Fluid Science, 32, pp. 1673-1678, 2008.

[10] Sylvain Antheaume, Thierry Maître, and Jean-Luc Achard, “Hydraulic Darrieus Turbines Efficiency for Free Fluid Flow Conditions Versus Power Farms Conditions”, Renewable Energy, 33, pp. 2186-2198, 2008.

[11] Zhenzhou Zhao, Yuan Zheng, Xiaoyun Xu, Wenming Liu, and Guoxiang Hu, “Research on the Improvement of the Performance of Savonius Rotor Based on Numerical Study”, Sustainable Power Generation and Supply, pp.1-6, 2009.

[12] Robert Howell, Ning Qin, and Jonathan Edwards, Naveed Durrani, “Wind Tunnel and Numerical Study of a Small Vertical Axis Wind Turbine”, Renewable Energy, 35, pp. 412-422, 2010.

[13] K. Pope, V. Rodrigues, R. Doyle, A. Tsopelas, R. Gravelsins, G.F. Naterer, and E. Tsang, “Effects of Stator Vanes on Power Coefficients of a Zephyr Vertical Axis Wind Turbine”, Renewable Energy, 35, pp. 1043-1051, 2010.

[14] Akinari Shigetomi, Yuichi Murai, Yuji Tasaka, Yasushi Takeda, "Interactive Flow Field Around Two Savonius Turbines", Renewable Energy, 36, pp.536-545, 2011.

[15] João Vicente Akwa, Gilmar Alves da Silva Júnior, Adriane Prisco Petry “Discussion on the Verification of the Overlap Ratio Influence on Performance Coefficients of a Savonius Wind Rotor Using Computational Fluid Dynamics”, Renewable Energy, 38, pp.141-149, 2012.

[16] S. McTavish, D. Feszty, T. Sankar, “Steady and Rotating Computational

Fluid Dynamics Simulations of a Novel Vertical Axis Wind Turbine for Small-Scale Power Generation", Renewable Energy, 41, pp.171-179, 2012.

[17] Joao Vicente Akwa, Horacio Antonio Vielmo, Adriane Prisco Petry, "A review on the performance of Savonius wind turbines", Renewable and Sustainable Energy Reviews, 16, pp.3054-3064, 2012.

[18] Tong Zhou, Dietmar Rempfer, "Numerical study of detailed flow field and performance of Savonius wind turbines", Renewable Energy, 51, pp.373-381, 2013.

[19] Boden, T., and G. Marland, Oak Ridge National Laboratory, Carbon Dioxide Information Analysis Center, 2010.

[20] Hiroki Hondo, "Life Cycle GHG Emission Analysis of Power Generation Systems: Japanese Case", Energy, 30, pp. 2042-2056, 2005.

[21] How do the wind turbines work. 2009. BiofuelsWatch.com. 2 Oct. 2011 http://www.biofuelswatch.com/how-do-wind-turbines-work/.

[22] Wake. Danish Wind Industry Association. 2 Oct. 2011 http://wiki.windpower.org/index.php?title=Wake&redirect=no.

[23] Manfred Stiebler, "Wind Energy Systems for Electric Power Generation", Springer-Verlag Berlin Heidelberg, 2008.

[24] Erich Hau, "Wind Turbines: Fundamentals, Technologies, Application, Economics", Springer-Verlag Berlin Heidelberg, 2006.